DOCTOR OF SCIENCES

Direct growth of graphitic carbon/graphene on Si(111) by using electron beam evaporation

Pham Thanh, Trung

Award date:
2015

Awarding institution:
University of Namur

UNIVERSITY OF NAMUR

Research Center for the Physics of Matter and Radiation

Laboratoire de Physique des Matériaux Electroniques

DIRECT GROWTH OF GRAPHITIC CARBON/GRAPHENE ON Si(111) BY USING ELECTRON BEAM EVAPORATION

Presented by Trung T. PHAM

Dissertation

For the Degree of DOCTOR IN SCIENCES

Jury Members:

President: Professor Laurent HOUSSIAU (University of Namur)

Examiners: Doctor Jacques DUMONT (R & D Centre, AGC Glass Europe)
Professor Jean-Marc THEMLIN (University of Aix Marseille)
Professor Olivier DEPARIS (University of Namur)

Supervisor: Professor Robert SPORKEN (University of Namur)

October 15, 2015

Acknowledgments

First, I would like to sincerely thank my supervisor, Robert SPORKEN, for welcoming and giving me the opportunity to do research in his laboratory (LPME). He encouraged me and always created the best conditions for me during my PhD study, but at the same time let me autonomous. In particular, I am very grateful to him for all his help about our family reunion (my wife and my daughter). We are very happy to live together in Belgium. This will be the most memorable time in our living abroad. Thanks to that, I have had a good motivation to complete my PhD thesis.

Next, I also would like to thank

- Vietnam International Education Development (VIED) for financial support during my four-year PhD study in Belgium. In particular, I am very appreciated Director of VIED, Mr. Vang X. NGUYEN, for his valuable advices and enthusiastic encouragements.
- The university of Technology and Education of HCMC for their agreement with me to obtain the fellowship from Vietnam government for four-year study in Belgium.

For all the members of the laboratory (LPME), I would like to say the most thankful words to

- Etienne GENNART for technical support in time and other help for our living. A funny member who often makes a lot of rememberable jokes. Thanks so much!
- Fernande FRISING and Jean-Pierre VAN ROY for the valuable encouragements.
- Frédéric JOUCKEN, a friendly colleague, his numerous scientific advices and fruitful discussions helped me a lot during these 4 years of research.
- Dodji AMOUZOU and Paul THIRY for helpful discussions.

Among the members of Namur University, many thanks go to

- Mac MUGUMAODERHA Cubaka for guiding me in technical and experimental steps at the beginning of my study. His support helped me a lot to be familiar with the initial experiments.
- Nicolas RECKINGER for helping in Raman measurement, guiding me for doing graphene transfer and nice discussions.
- Francesca CECCHET for helping in AFM analyses and useful discussions.
- Benjamin BERA for helping in Magnetron sputtering of SiO_2 on my samples and discussions.
- Jacques GHIJSEN for helping UPS analyses in Hamburg, Alexandre FELTEN, Laurent NITTLER, Pierre LOUETTE for XPS and Jean-François COLOMER for SEM measurements.
- Jean-Paul LEONIS for assisting the paperworks whenever I met problems.
- Mrs. Cathy JENTGEN, Mrs. Florence COLLOT and Mr. Charles DEBOIS for their arrangement of our accommodation at an apartment of the university during my study.

My acknowledgements are also dedicated to Benoit HACKENS, Cristiane N. SANTOS, Jessica CAMPOS-DELGADO, Sébastien FANIEL for Raman and HR-SEM annalyses with useful discussions and Jean-Pierre RASKIN, Pierre-Antoine HADDAD for training on fabrication of graphene field-effect transistors at WINFAB in Université Catholique de Louvain (UCL) with interesting discussions/suggestions.

In addition, I would also like to thank all members of the jury for having kindly accepted to evaluate my work and the University of Namur for funding conferences, workshops and scientific stays.

Last but not least in my heart, all my thankfulness to my little family (my wife - Nuong and my daughter - Nguyen), my father, my parents in law, brothers, sister and to all my friends encouraged and always stayed beside me during my study abroad.

Thank you all!

Trung T. PHAM
Namur - Belgium
August 15, 2015

Abstract

Graphene has recently emerged as a promising material due to its outstanding electrical, optical, thermal, and mechanical properties. It opens new possibilities not only for fundamental physics research but also for industrial applications. Nowadays, since silicon is still the most important single-crystal substrate used for semiconductor devices and integrated circuits, integration of graphene into the current Si technology is highly desirable. A combination between graphene and silicon may overcome the traditional limitations in scaling down of devices that silicon-based technology is facing. Graphene on Si might be one of the most promising candidates as a material for graphene-based technology beyond CMOS. Therefore, it is crucial to find a process to grow graphene directly on Si.

In this thesis, we chose Si(111) as a substrate for graphene formation by electron beam evaporation because its surface has an interesting multi-layer reconstruction driven by the minimization of dangling bonds at the surface compared with other oriented Si. It exhibits a six-fold symmetry and is the most stable surface among various orientations of Si. Therefore, it is expected to be an appropriate substrate for graphitic carbon growth. However, due to the huge lattice mismatch between graphene ($a_G = 2.46$ Å) and Si(111) ($a_{Si_{1\times1}} = 3.84$ Å), it is not easy to grow directly graphene on Si(111) and a buffer is considered as a solution to reduce the lattice mismatch. In this context, we have proposed a structural model using amorphous carbon (a-C) and/or SiC as a buffer on Si(111) with different configurations such as C/a-C/Si(111), C/a-C/3C-SiC/Si(111), C/3C-SiC/Si(111) or C/Si/3C-SiC/Si(111) (C stands for the graphitic layer). The quality of the graphitic layer depends not only on the substrate temperature but also on the growth time and on the thickness of the buffer layer. In addition, we also found that silicon diffuses through the SiC buffer layer during the graphene growth and reduces the quality of epitaxial graphene. Therefore, a calculation of the silicon diffusion profile through the SiC buffer layer during carbon deposition is presented to explain how the crystalline quality of graphene depends on the details (annealing temperature, growth time, etc.) of the growth process.

Résumé

Le graphène a récemment émergé comme un matériau prometteur en raison de ses propriétés exceptionnelles tant électriques, optiques, thermiques que mécaniques. Il ouvre de nouvelles possibilités, non seulement pour la recherche en physique fondamentale, mais aussi pour les applications industrielles. Actuellement, puisque le silicium est encore le substrat monocristallin le plus important utilisé pour la fabrication des dispositifs semi-conducteurs et des circuits intégrés, l'intégration du graphène dans la technologie silicium est hautement souhaitable. Une combinaison entre graphène et silicium peut aider à dépasser les limites de miniaturization rencontrées par l'industrie. Le graphène sur silicium est un candidat prometteur pour dépasser la technologie CMOS. Par conséquent, trouver un processus pour faire croître le graphène directement sur silicium est un sujet important.

Dans cette thèse, nous avons choisi le Si(111) comme substrat pour la formation du graphène en utilisant l'évaporation par faisceau d'électrons parce que sa surface présente une reconstruction intéressante entraînée par la minimisation des liaisons pendantes comparée aux autres surfaces du silicium. Elle présente une symétrie hexagonale et est la surface la plus stable parmi les orientations du silicium. Par conséquent, il est considéré comme un substrat approprié pour la croissance du carbone graphitique. Cependant, à cause de la grande différence des paramètres de maille entre le graphène ($a_G = 2.46$ Å) et le Si(111) ($a_{Si_{1\times1}} = 3.84$ Å), il n'est pas aisé de faire croître directement le graphène sur le Si(111) et une couche tampon peut être considérée comme une solution à ce problème. Dans ce contexte, nous avons proposé un modèle utilisant le carbone amorphe (a-C) ainsi que le SiC comme couche tampon, en différentes combinaisons, telles que C/a-C/Si(111), C/a-C/3C-SiC/Si(111), C/3C-SiC/Si(111) ou C/Si/3C-SiC/Si(111) (C représente la couche graphitique). La qualité de la couche graphitique dépend de la température du substrat mais aussi du temps de croissance et de l'épaisseur de la couche tampon. Nous avons aussi trouvé que le silicium du substrat diffuse au travers de la couche tampon de SiC pendant la croissance du graphène ce qui réduit la qualité du graphène obtenu. Nous présentons en outre un calcul du profil de diffusion du silicium qui explique comment la qualité du graphène dépend des détails du processus de croissance.

Keywords: Graphitic carbon, graphene on Si, buffer layer, electron beam evaporation, Si diffusion.

List of abbreviations

Abbreviation	Full name
0D	Zero dimension
1D	One dimension
2D	Two dimensions
3D	Three dimensions
a-C	amorphous carbon
AES	Auger electron spectroscopy
AFM	Atomic force microscope
BCC	Body-centered cubic
CMP	Chemomechanical polishing
CMOS	Complementary metal-oxide-semiconductor
CVD	Chemical vapor deposition
DAS	Dimer-adatom-stacking
FCC	Face-centered cubic
FWHM	Full width at half maximum
g-C	graphitic carbon
G-FETs	Graphene field-effect transistors
GO	Graphene oxide
HAC	Hydrogenated amorphous carbon
HOPG	Highly oriented pyrolytic graphite
HR-SEM	High resolution scanning electron microscope
HV	High voltage
IMFP	Inelastic mean free path
FFT	Fast Fourier transform
FT-IR	Fourier transform infra-red
LEED	Low energy electron diffraction
LED	Light emitting diode
LO	Longitudinal optical
LPME	Laboratoire de Physique des Matériaux Electroniques
MBE	Molecular beam epitaxy
MFP	Mean free path
ML	Monolayer
MWCNTs	Multi-wall carbon nanotubes
NEXAFS	Near edge X-ray absorption fine structure
PMMA	Polymethyl methacrylate

RF	Radio frequency
RHEED	Reflection high energy electron diffraction
RS	Raman spectroscopy
RMS	Root mean square
SEM	Scanning electron microscope
SL	Single layer
STM	Scanning tunneling microscope
SWCNTs	Single wall carbon nanotubes
TEM	Tunneling electron microscope
T-P	Temperature - Pressure
TO	Transverse optical
UHV	Ultra-high vacuum
XPS	X-ray photoemission spectroscopy

List of publications and conference presentations

Number	**Publications**
1	Trung T. Pham, Frédéric Joucken, Jessica Campos-Delgado, Benoit Hackens, Jean-Pierre Raskin, Robert Sporken, *Direct growth of graphitic carbon on Si(111)*, Applied Physics Letters, 102, 013118 (2013).
2	Trung T. Pham, Jessica Campos-Delgado, Frédéric Joucken, Jean-François Colomer, Benoit Hackens, Jean-Pierre Raskin, Cristiane N. Santos, Robert Sporken, *Direct growth of graphene on Si(111)*, Journal of Applied Physics, 115, 163106 (2014).
Number	**Conference presentations**
1	Trung T. Pham, Frédéric Joucken, Jessica Campos-Delgado, Benoit Hackens, Jean-Pierre Raskin, Robert Sporken, *Direct growth of graphitic carbon on Si(111) by e-beam evaporation*, poster presentation, Materials sciences and technology, Halong-Vietnam (October 2012).
2	Trung T. Pham, Frédéric Joucken, Jessica Campos-Delgado, Benoit Hackens, Jean-Pierre Raskin, Robert Sporken, *Direct growth of nanocrystalline graphene films on Si(111)*, poster presentation, Graphene2013, Bilbao-Spain (April 2013).
3	Trung T. Pham, Frédéric Joucken, Benoit Hackens, Jean-Pierre Raskin, Robert Sporken, *Direct growth of graphene on Si(111)*, oral presentation (invited talk), MBE-grown graphene 2013, Berlin-Germany (October 2013).
4	Trung T. Pham, Frédéric Joucken, Jessica Campos-Delgado, Benoit Hackens, Jean-Pierre Raskin, Robert Sporken, *Direct growth of graphene on Si(111)*, poster presentation, Graphene2014, Toulouse-France (May 2014).
5	Trung T. Pham, Frédéric Joucken, Cristiane N. Santos, Benoit Hackens, Jean-Pierre Raskin, Robert Sporken, *Influence of substrate temperature and thickness of SiC buffer layer on the quality of graphene on Si(111)*, poster presentation, Graphene2015, Bilbao-Spain (March 2015).
6	Trung T. Pham, Frédéric Joucken, Cristiane N. Santos, Benoit Hackens, Jean-Pierre Raskin, Robert Sporken, *Influence of substrate temperature and thickness of SiC buffer layer on the quality of graphene on Si(111)*, oral presentation, Graphene2015, Bilbao-Spain (March 2015).

Epigraph

Learn from yesterday, live for today, hope for tomorrow. The important thing is not to stop questioning.

Albert Einstein (1879 - 1955)

There are two possible outcomes:

- *If the result confirms the hypothesis, then you've made a measurement.*
- *If the result is contrary to the hypothesis, then you've made a discovery.*

Enrico Fermi (1901 - 1954)

Table of Contents

List of Figures

List of Tables

Chapter 1

INTRODUCTION

1.1. General introduction

Carbon is a chemical element at the origin of living things. It exists in many different allotropes with different kinds of hybridization such as sp^3 (as in diamond), sp^2 (as in graphite), sp (as in carbynes) [1, 2]. During the last few decades, it has always surprised the scientific community with the discovery of new materials which are derived from carbon such as fullerene (0D) in 1985 [3], carbon nanotube (1D) in 1991 [4] and graphene (2D).

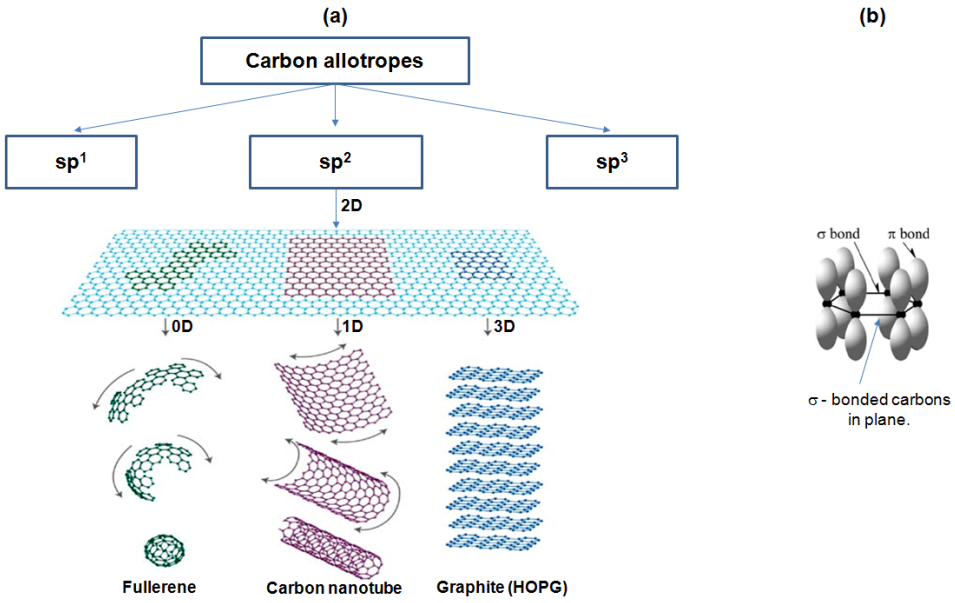

Fig. 1.1: (a) Carbon family tree shows known carbon allotropes where graphene is illustrated as the origin of all graphitic forms: roll into fullerenes (buckyballs)/ nanotubes or stack into multilayer graphite; (b) A sp^2 hybridization bonds in the honeycomb structure. Images adapted from Refs. [5, 6].

Among them, graphene is the newest member of the carbon family. It was isolated and its electronic transport properties were first measured in 2004 [7]. It consists of a single layer of sp^2 bonded carbon atoms in a two-dimensional honeycomb crystal lattice. As described in Fig. 1.1, graphene is considered as the basic building block of all graphitic forms [5].

As illustrated by Geim et al. [5], graphene can roll into buckyballs (0D) or nanotubes (1D) as well as stack into multilayer graphite (3D). These materials have unusual properties compared to silicon (Table 1.1).

Properties	Silicon	Fullerenes	Carbon nanotubes	HOPG	**Graphene**
Electrical conductivity ($\Omega^{-1}\cdot$ m^{-1})	$\sim 4.3 \times 10^{-4}$ [8]	$\sim 2\times10^{-5}$ [9]	$\sim 10^8$ (SWCNTs) [10]; 3×10^6 (MWCNTs) [11]	$\sim 2.6 \times 10^3$ [12]	$\sim 1.3 \times 10^8$ [13]
Thermal conductivity (W/m K)	156 [14]	0.4 [15]	6.6×10^4 (SWCNTs) [16]; $> 3 \times 10^3$ (MWCNTs) [17]	$\sim 3 \times 10^3$ [18, 19]	$\sim 5 \times 10^3$ [20]
Optical transparency (%)	-	-	-	-	~ 97.7 [21]
Electron mobility μ (cm^2/V·s)	$\leq 1.4 \times 10^3$ [22]	0.56 [23]	$\sim 10^5$ [24]	$5\times10^4 \leq \mu \leq 4 \times 10^7$ (*) [25]	$\sim 1.5 \times 10^4$ (**) [26], $\geq 1.1 \times 10^4$ (***) [27]; $\sim 2.0 \times 10^5$ (****) [28]

Table 1.1: Properties of carbon materials in comparison with silicon. (*) measured from 270 K to 3 K, respectively; (**) graphene on SiO_2 (the value was independent of temperature T between 10 and 100 K); (***) graphene on 4H-SiC measured at $\sim$ 0.3 K; (****) suspended graphene measured at $\sim$ 5 K.

In a graphene lattice, carbon atoms form a very strong σ bond with the three other atoms through sp^2 hybridization in the same plane (Fig. 1.1 (b)). This is responsible for the mechanical properties of graphene [29] while the remaining p orbital is available to form a π bond with adjacent atoms in the surface normal, which gives rise to graphene's unique electronic properties [7, 26, 30]. This has brought graphene to the center of attention during the past ten years. Indeed, graphene exhibits ballistic electron transport (electrons can travel submicron distances without scattering) [5], very high electron mobilities have been observed ($\sim$ 15000 cm^2/V.s for graphene on SiO_2 substrate [26], $\geq$ 11000 cm^2/V.s for epitaxial graphene on 4H-SiC substrate at $\sim$ 0.3 K [27] and $\sim$ 200000 cm^2/V.s for suspended graphene at $\sim$ 5 K [28]). Moreover, some studies also reported other outstanding properties such as high transparency [21] and superior thermal conductivity [20] which make graphene emerge as an exciting novel material. Therefore, graphene was considered as an excellent candidate for nanoelectronic devices. For example, graphene field-effect transistors (G-FETs) [31], transparent electrodes in solar cells [32], light emitting diodes [33], optoelectronics [34], sensors [35] and so on.

Since the discovery of isolated graphene by Geim and his co-workers at Manchester University using mechanical exfoliation of highly oriented pyrolytic graphite (HOPG) [7], followed by the award of the Nobel prize in Physics 2010 [36], enormous efforts have been devoted to grow, transfer and characterize graphene on various substrates using many different methods in order to obtain high quality and large area graphene as reflected by number of publications and published patents per year from the worldwide patent landscape in 2015 (Fig. 1.2).

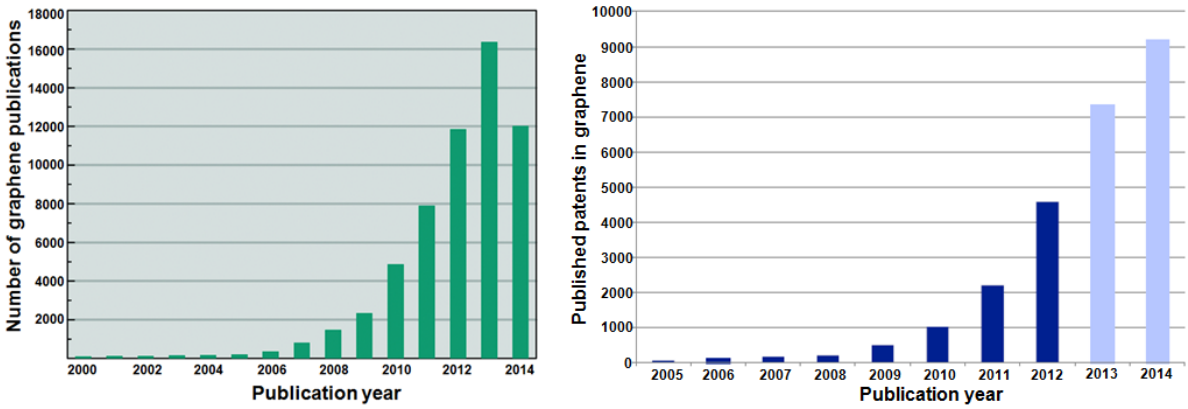

Fig. 1.2: (a) Number of graphene publications vs. year (Source from wwww.google.com when searching for "number of publications in graphene"); (b) number of published patents in graphene until 2014 (Source from the worldwide patent landscape in 2015). The data for 2013 and 2014 is shaded light blue to show the quick change over the period with the peak year as shown in 2014.

In fact, information about how graphene was prepared is very important because the properties of graphene strongly depend on preparation methods [37]. In my opinion, the reported methods generally fit into two major approaches which are

- **Top-down**

  Some typical examples for this approach (exfoliation from bulk) are graphene exfoliated from HOPG [7] or obtained by chemical exfoliation of pristine graphite oxide [38]. Graphene oxide (GO) is produced from purified natural graphite by the Hummers method [39, 40]. Moreover, one can also mention some others such

as liquid-phase exfoliation [41], chemical self assembly of graphene sheets from graphite via electrostatic interactions [42], electrochemical exfoliation [43] and graphite intercalation compounds (as stacks of individual doped graphene layers) [44].

One can see that the advantages of these methods are scalability and high graphene quality. However, it is difficult to obtain single layer of defect-free graphene because of film impurity and large numbers of defects created during exfoliation and cost for mass-production is very high (see Fig. 1.3).

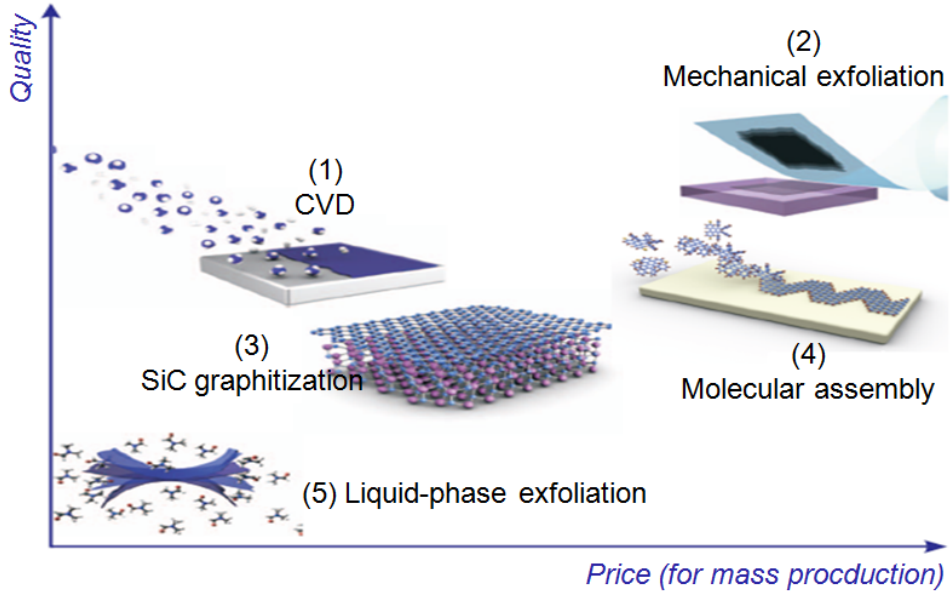

Fig. 1.3: Quality vs. Cost for graphene production. Reported by Novoselov et al. [45].
(1) CVD growth: *high graphene quality, low cost. Used for applications such as coating, bio, transparent conductive layers, electronics, photonics*;
(2) Mechanical exfoliation: *high graphene quality, high cost. Used for research and prototyping*;
(3) SiC graphitization: *high graphene quality, high cost. Used for electronics, RF transistors*;
(4) Molecular assembly: *high graphene quality, high cost. Preferred for nanoelectronics*;
(5) Liquid-phase exfoliation: *low quality, low cost, for applications such as coating, composites, inks, energy storage, bio, transparent conductive layers.*

In particular, reduction of GO into graphene-like sheets by removing the oxygen

results in a graphitic structure that is also one atomic layer thick, but it still contains many defects [46, 47].

- **Bottom-up**
  The other way by which graphene can be obtained is bottom-up approach (atom by atom growth). Some common methods are chemical vapor deposition (CVD) from organic precursors of methane and other hydrocarbon sources on metal substrates [48–51], epitaxial growth on bulk SiC by thermal decomposition [52, 53], electron beam evaporation [54, 55], splitting carbon nanotubes to form graphene ribbons [56], etc. These are some of the most attractive methods to produce high-quality of graphene, in some case over large area.

The presence of graphene material has opened new possibilities not only for fundamental physics research but also for industrial applications. The development of electronic device technology based on silicon still depends on scaling down of the size of the transistor [57]. According to the semiconductor industry roadmap, the size and the speed of the silicon transistor will soon reach its lower limit due to the poor stability of silicon at 10 nm and below when it oxidises, decomposes and uncontrollably migrates [58–60]. In this context, it is expected that graphene could be used to improve silicon-based devices, in particular in high-speed electronics and optical modulators [59]. In order to benefit from the ultrafast carrier transport in graphene, integrating graphene with the current silicon technology is highly desirable. A combination between graphene and silicon may overcome not only the traditional limitations in size of devices but also in performance that silicon-based technology is facing. Graphene on silicon will pave the way to fabricate devices beyond CMOS technology (depicted as Figs. 1.4 (b, c)). Therefore, there have recently been several attempts to grow graphene on Si wafer [49, 50, 54, 55, 61–66]. However, direct deposition of carbon atoms while maintaining the substrate at a given temperature [54, 55] produces graphene films with poor crystalline quality. Graphitization of SiC buffer layers preformed on Si wafer [61–64] requires very high temperature which renders it not directly compatible with standard Si processing technology. It has been proposed to use catalysts on Si wafer [49, 50, 65, 66] to reduce the thermal mismatch between graphene and the substrate and to avoid out-diffusion of Si atoms from the substrate during growth. However, it could still generate contamination for nano-scale integrated applications due to inter-diffusion between catalyst material

and the Si substrate. So, direct growth of graphene on bare Si substrate without any other material (catalysts) is very attractive.

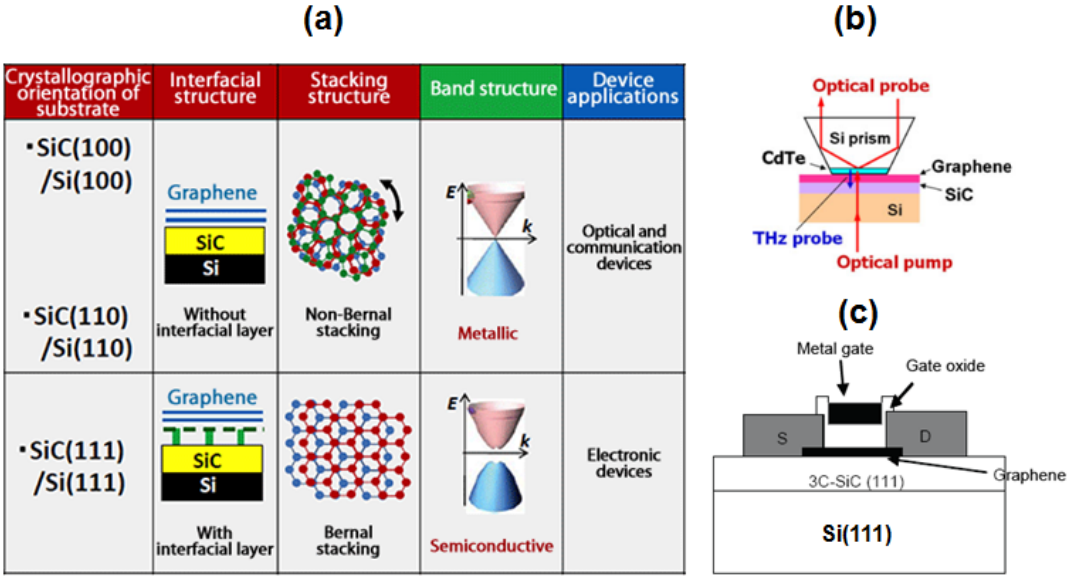

Fig. 1.4: (a) Realization of multifunctional graphene on Si utilizing different crystallographic orientations of Si substrate, adapted from [67]; (b) Terahertz emission in graphene on $3C$-SiC/Si(110), adapted from [68]; (c) G-FET on $3C$-SiC/Si(111), adapted from [69].

For our study of the growth of graphene on Si using electron beam evaporation, we choose Si(111) 7×7 surface [1] as a substrate for graphitic carbon growth using an amorphous carbon (a-C) and/or a $3C$-SiC layer [2] as a buffer for the following reasons:

- The Si(111) surface has an interesting multi-layer reconstruction driven by the minimization of dangling bonds at the surface [70]. It exhibits a six-fold symmetry and is the most stable surface among various orientations of Si [71–73]. Therefore, it should be an appropriate substrate for growing a $3C$-SiC buffer layer with high crystalline quality [74].

- Graphene film on $3C$-SiC/Si(111) has semiconducting properties which are suitable

[1] A reconstructed silicon surface with surface lattice unit cell is 7 times larger than the (1×1) Si(111) surface.

[2] A polytype of SiC.

for the fabrication of electronic devices (Fig. 1.4 (a)) in contrast to graphene film on other silicon surfaces [62, 75, 76].

1.2. Outline

This thesis is organized as follows.

Chapter 2 will describe the structure of the samples produced in this study. Also, the experimental techniques used to produce and characterise our graphene layers will be presented.

Chapter 3 will review experimental results regarding graphene on Si obtained by other groups.

In chapter 4, experimental results from characterization of graphene on Si(111) by Auger electron spectroscopy (AES), X-ray photoemission spectroscopy (XPS), low energy electron diffraction (LEED), reflection high energy electron diffraction (RHEED), scanning electron microscope (SEM), atomic force microscope (AFM) and scanning tunneling microscope (STM) will be analysed and discussed in detail. Also, a calculation of the silicon diffusion profile through the buffer layer during carbon growth will be presented in order to explain how the quality of graphene depends on the details of the growth process.

In the last chapter, experimental results will be summarised and possible new directions of work will be suggested.

Chapter 2

STRUCTURAL PROPERTIES, STUDIED METHOD AND EXPERIMENTAL TECHNIQUES

2.1. Introduction

In this chapter, the structural properties of Si(111) 7×7 as well as other relevant materials deposited on it will be described. The experimental setup using a mini electron-beam evaporator will be presented. Experimental techniques used for characterization of graphene layers will also be presented in the final section of the chapter.

2.2. Structure of C/Si(111) samples

By annealing at high temperature (above 1000 °C) in UHV, followed by slow cooling to room temperature, a (111)-oriented Si surface will reconstruct into Si(111) 7×7 [70]. It still exhibits a six-fold symmetry so that it is expected to be an appropriate substrate for graphitic carbon growth. However, due to the huge lattice mismatch between graphene sheets (a_G = 2.46 Å) and Si(111) 7×7 ($a_{Si_{7\times7}}$ = 26.9 Å), it is not easy to grow directly graphene at room temperature on Si(111) 7×7. Interestingly, the Si(111) 7×7 reconstructs into 1×1 at ∼ 870 °C [77]. At this temperature, the lattice mismatch between them is decreased to about 36% and thus keeping the substrate at this temperature might be considered in order to grow graphene directly on Si(111). Therefore, some groups followed this path [54, 55], but these graphene films exhibit poor crystallinity. In order to improve the crystalline quality, a buffer layer is necessary to reduce the lattice mismatch. Some grew a thick SiC film, followed by SiC graphitization at very high temperature (above 1300 °C) in UHV [61–64] or used metal/insulating

catalysts on Si wafer as a diffusion barrier during CVD growth of graphene [49, 50, 66]. To be compatible with standard Si transistor processing technology, growing graphene on Si wafer without any catalysts is still preferable. In this context, we investigated direct formation of graphene using a buffer layer on Si(111) substrate (no graphitization) as shown in Fig. 2.1. In this thesis, an a-C film deposited at room temperature and/or

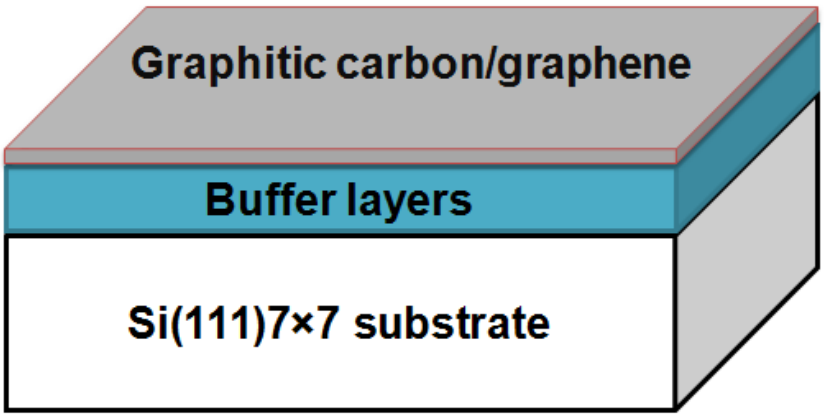

Fig. 2.1: Structural model for growing graphene on Si(111) 7×7 substrate.

silicon carbide (SiC) grown on Si(111) are considered as a buffer layer.

2.3. Crystallographic structures of relevant materials

2.3.1. Real and reciprocal lattice vectors

For 3D crystals, the position vector of a lattice point in real space (r-space) is given by

$$\mathbf{R}_{xyz} = x\mathbf{a}_1 + y\mathbf{a}_2 + z\mathbf{a}_3, \tag{2.1}$$

where x, y and z are integers; $\mathbf{a}_1$, $\mathbf{a}_2$ and $\mathbf{a}_3$ are real space unit vectors.
A reciprocal lattice is then defined by

$$\mathbf{G}_{hkl} = h\mathbf{b}_1 + k\mathbf{b}_2 + l\mathbf{b}_3, \tag{2.2}$$

where h, k and l are integers; $\mathbf{b}_1$, $\mathbf{b}_2$ and $\mathbf{b}_3$ are reciprocal unit vectors.

The relationship between the real and reciprocal lattice vectors is given by [78]

$$\mathbf{G}_{hkl} \bullet \mathbf{R}_{xyz} = 2\pi n, \tag{2.3}$$

where n is any integer.

Therefore, the reciprocal unit vectors can be obtained as

$$\mathbf{b}_1 = 2\pi \frac{\mathbf{a}_2 \times \mathbf{a}_3}{\mathbf{a}_1 \cdot (\mathbf{a}_2 \times \mathbf{a}_3)}, \mathbf{b}_2 = 2\pi \frac{\mathbf{a}_3 \times \mathbf{a}_1}{\mathbf{a}_1 \cdot (\mathbf{a}_2 \times \mathbf{a}_3)}, \mathbf{b}_3 = 2\pi \frac{\mathbf{a}_1 \times \mathbf{a}_2}{\mathbf{a}_1 \cdot (\mathbf{a}_2 \times \mathbf{a}_3)} \tag{2.4}$$

and, vectors $\mathbf{a}_1$, $\mathbf{a}_2$ and $\mathbf{a}_3$ are related to $\mathbf{b}_1$, $\mathbf{b}_2$ and $\mathbf{b}_3$ as $\mathbf{b}_i.\mathbf{a}_j = 2\pi\delta_{ij}$ with $\delta_{ii} = 1$, $\delta_{ij} = 0$ if $i \neq j$.

In order to describe crystal planes, the Miller indices are defined as (hkl) to denote the crystallographic plane of Bravais lattices. For example, it can be shown that (hkl) plane in a cubic system is normal to the vector $[hkl]$ whose origin is at a point (0,0,0) of the lattice and that it intersects the axes at distance *1/h*, *1/k* and *1/l* from the origin.

For 2D crystals, Fig. 2.2 illustrates a simple case for a two dimensional real space which consists of $\mathbf{a}_1$ and $\mathbf{a}_2$ unit vectors. As defined for the reciprocal space, the corresponding reciprocal unit vectors $\mathbf{b}_1$ is perpendicular to $\mathbf{a}_2$ and $\mathbf{b}_2$ is perpendicular to $\mathbf{a}_1$.

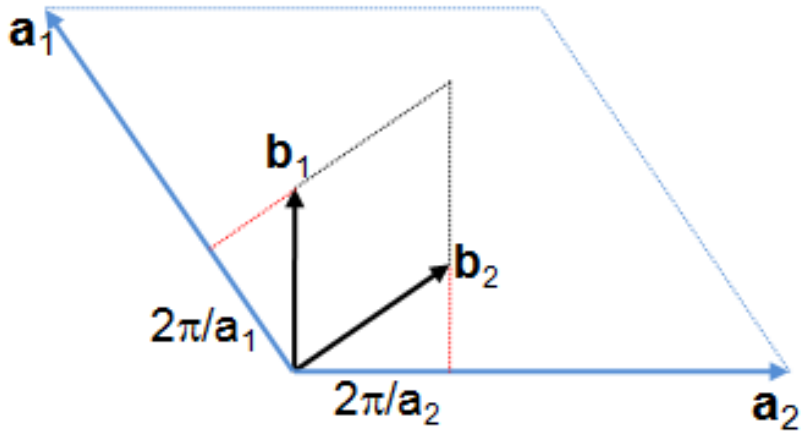

Fig. 2.2: The relationship between a real and reciprocal lattice vectors.

2.3.2. Reciprocal characterization

In order to determine a real space lattice structure, electron diffraction (LEED and RHEED) is one of the most popular experimental techniques. This technique uses the wave-like character of the electrons. Recall that the momentum and the wavelength are linked by the de Broglie relation

$$\lambda = h/p, \tag{2.5}$$

where p is the magnitude of momentum and h is Planck's constant.

This equation can be written as

$$\mathbf{k} = \mathbf{p}/\hbar, \tag{2.6}$$

if we define the wavevector $\mathbf{k}$ parallel to the direction of propagation with a magnitude $k = |\mathbf{k}| = 2\pi/\lambda$

For a simple example, the diffraction of an electron wave on a crystalline sample consists of an incoming wavevector $\mathbf{k}_i$ and a scattered wavevector $\mathbf{k}_f$ as illustrated in Fig. 2.3. If

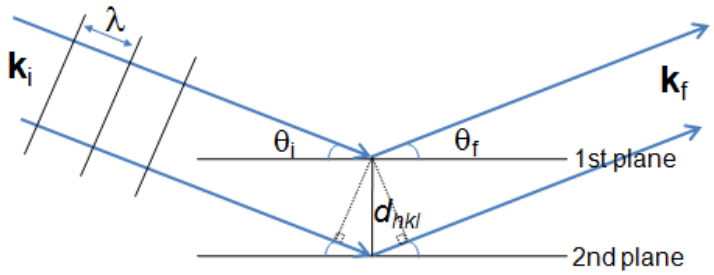

Fig. 2.3: Electron diffraction from two parallel planes.

the scattering is elastic, $|\mathbf{k}_i| = |\mathbf{k}_f| = |\mathbf{k}| = k$. In this case, if considering $\theta_i = \theta_f = \theta$, the change in wavevectors is defined as

$$\Delta\mathbf{k} = \mathbf{k}_f - \mathbf{k}_i \tag{2.7}$$

The magnitude is

$$|\Delta\mathbf{k}| = \frac{4\pi}{\lambda} sin\theta \tag{2.8}$$

Comparing the diffraction condition $\Delta\mathbf{k}\bullet\mathbf{R}_{xyz} = 2\pi n$ (n is any integer) with equation

(2.3), we have

$$\Delta \mathbf{k} = \mathbf{G}_{hkl} \tag{2.9}$$

Since the lattice spacing $d_{hkl} = \frac{2\pi n}{|\mathbf{G}_{hkl}|}$, we obtain Bragg's diffraction condition

$$2d_{hkl}\sin\theta = n\lambda \tag{2.10}$$

2.3.3. Crystallographic structure in the real and reciprocal space

a. Si(111) 7×7 surface reconsctruction

The presence of one dangling bond per unit cell on the (1×1) Si(111) surface [79] leads to a highly reactive surface (surface instability), although the density of dangling bonds as well as the surface tension are higher for other surfaces [80, 81] (Fig. 2.4 (a)). As a

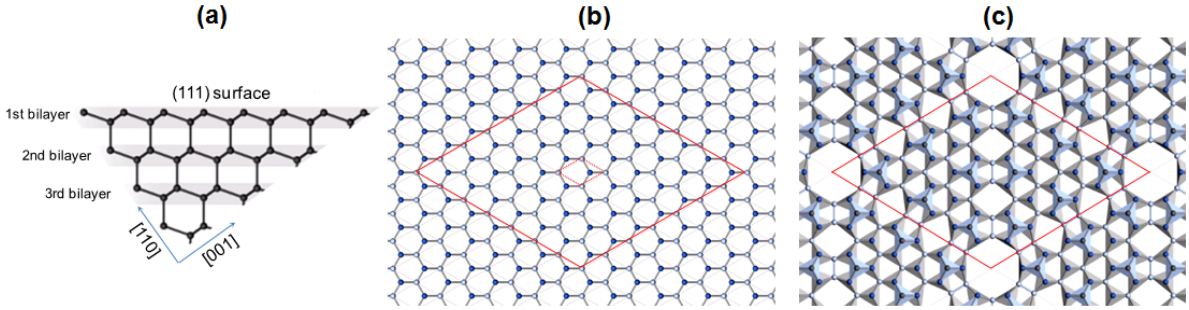

Fig. 2.4: (a) Side view of single crystalline network of silicon atoms on Si(111); (b) (7×7) unit cell obtained by repeating the primitive unit cell (dashed rhombus in red) and (c) top view of Si(111) surface after surface reconstruction. Images adapted from Ref. [82].

result, a reconstruction will occur in the first bilayer. Fig. 2.4 (b) shows the top view of the Si(111) surface with the silicon atoms in the first bilayer in which blue atoms are in the top half of the bilayer and gray ones in the bottom half of the bilayer. By repeating the primitive unit cell, a 7×7 structure can be generated. Under appropriate annealing temperatures, these silicon atoms will re-arrange to form a 7×7 reconstructed surface (see Fig. 2.4 (c)).

By using the dimer adatom stacking (DAS) model of Takayanagi et al. [83], one can identify 19 dangling bonds in total for each 7×7 unit cell: 12 for adatoms, 6 for rest-atoms,

and 1 inside the corner hole. So, the number of dangling bonds is reduced from formerly 49 for the unreconstructed Si(111) surface to 19 in the (7×7) reconstructed surface unit cell as shown in Fig. 2.5. As a result, the Si(111) surface becomes more stable after reconstruction.

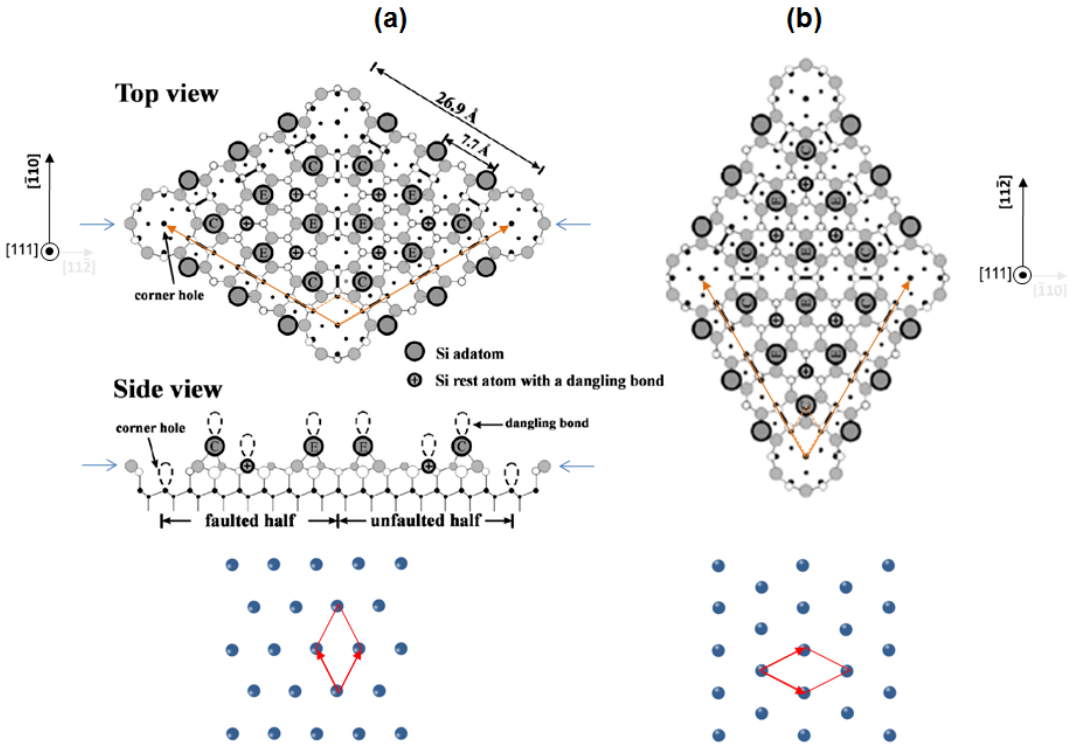

Fig. 2.5: (a) Top view along [111] of the DAS model of the Si(111) 7×7 reconstructed surface by Takayanagi et al. [83]. The rhomboidal surface unit cells consist of faulted and unfaulted half cells, separated by rows of dimers. There are 12 adatoms in the topmost Si layer (layer 0 - indicated with C at corner sites and E at edge center sites) + 6 rest atoms in layer 2 (marked with a + sign) + a corner hole atoms in layer 3 = 19 in the (7×7) reconstructed surface unit cell. The unit cell vectors along $[\bar{1}10]$ and its corresponding reciprocal lattice; (b) The unit cell vectors along $[11\bar{2}]$ and its corresponding reciprocal lattice. Images adapted from Ref. [84].

In the reciprocal space, the Si(111) 7×7 surface is presented in a hexagonal lattice as constructed in the bottom part of Fig. 2.5 from $[\bar{1}10]$ and $[11\bar{2}]$ basis vectors. This will lead to diffraction patterns which will be illustrated in the next section.

b. Silicon carbide

silicon carbide (SiC) is a hard material with a large bandgap which is well-suited for many applications such as high temperature operation, high radiation conditions and high power [85]. One of the more recent applications of SiC is large scale production of epitaxial graphene. Although SiC single crystal wafers are now commercially available, the growth of SiC on silicon single crystals is desirable because SiC wafers remain quite expensive. Although more than 250 different SiC polytypes exist [86], cubic $3C$-SiC is the only polytype that grows on Si substrates. Most of the properties vary only slightly from one polytype to another. In general, there are three common SiC polytypes which have similar properties as shown in Fig. 2.6.

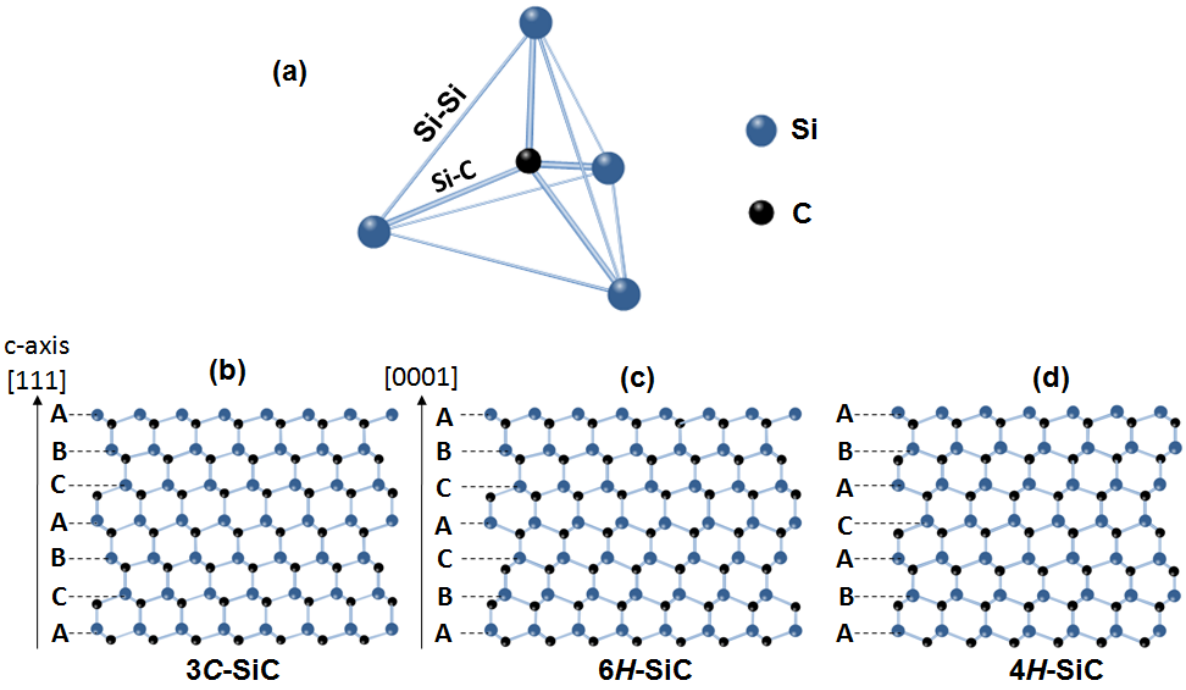

Fig. 2.6: (a) The building block of SiC - tetrahedron of C atom bonded to four Si atoms; Stacking of layers in real space compared among (b) $3C$-, (c) $6H$-, and (d) $4H$-SiC.

Each carbon atom is surrounded by four Si atoms in the tetrahedron as shown in Fig. 2.6 (a) or vice versa. The distances between Si-Si bonds and Si-C bonds are ~ 3.08 Å and ~ 1.89 Å, respectively. With the definition of c-axis along one of the Si-C bonds, a side

Polytypes	Stacking order	Lattice constant (Å)	Band gap (eV)
3C-SiC (β-SiC)	**ABCA**	4.36	2.3
6H-SiC (α-SiC)	**ABCA**CBA	3.08	3.0
4H-SiC (α-SiC)	ABACA	3.08	3.3

Table 2.1: The most three common polytypes of SiC and their structural properties, reported by Hmida et al. [85].

view of SiC crystal is shown in Figs. 2.6 (b), (c) and (d) with stacking of Si-C bilayers which contains a planar sheet of Si atoms coupled with the one of C atoms. The distance between two adjacent Si-C bilayers is $\sim$ 2.51 Å [87]. It is possible to form all of the SiC polytypes from these tetrahedrons by stacking them with 180° rotation around its c-axis [86]. Each polytype has a different stacking order depending on the so called Ramsdell notation as nX, where n is the number of stacking sequences required to describe the unit cell and X describes the crystal symmetry such as C for Cubic, H for Hexagonal or R for Rhombohedral [88] and etc. The structural properties of the most common polytypes are listed in Table 2.1.

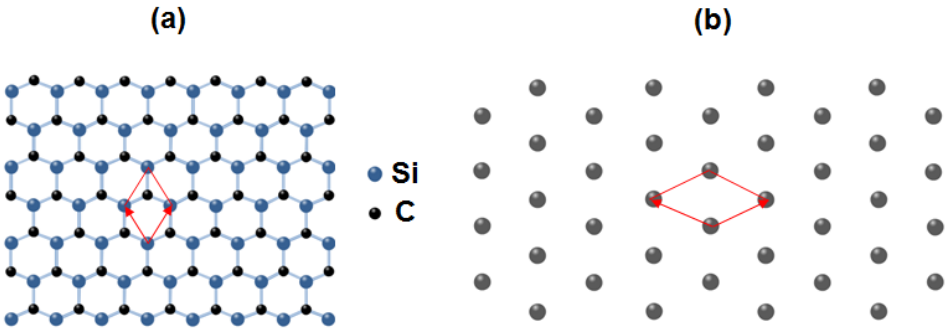

Fig. 2.7: (a) Top view along [0001] of the real space from three common SiC polytypes; (b) corresponding reciprocal lattice.

Fig. 2.7 shows the surface reciprocal lattice which is the same for these three polytypes.

c. Amorphous carbon

a-C is a form of carbon that does not have any long range order. Thus, it is known as a highly disordered carbon structure. The a-C contains a high concentration of dangling bonds with many hybridized bonds such as sp^2, sp^3 bonded carbons. By determining the

ratio of sp^3 to sp^2 bonded bonds, it is possible to distinguish different forms of *a*-C [89]. There are two common kinds of amorphous carbon: *ta*-C (tetrahedral amorphous carbon) considered as diamond-like carbon [90] which is produced by evaporation/sputtering techniques and *a*C:H or HAC (hydrogenated amorphous carbon) [91] by plasma deposition of hydrocarbons from ethylene. The ratio of sp^3/sp^2 bonds depends on the growth conditions (substrate temperature, hydrogen content, etc.). That is why the idea of using *a*-C as a buffer layer for obtaining graphene on Si(111) substrate in the context of this study will be presented in chapter 4.

A typical disordered structure of *a*-C is illustrated in Fig. 2.8.

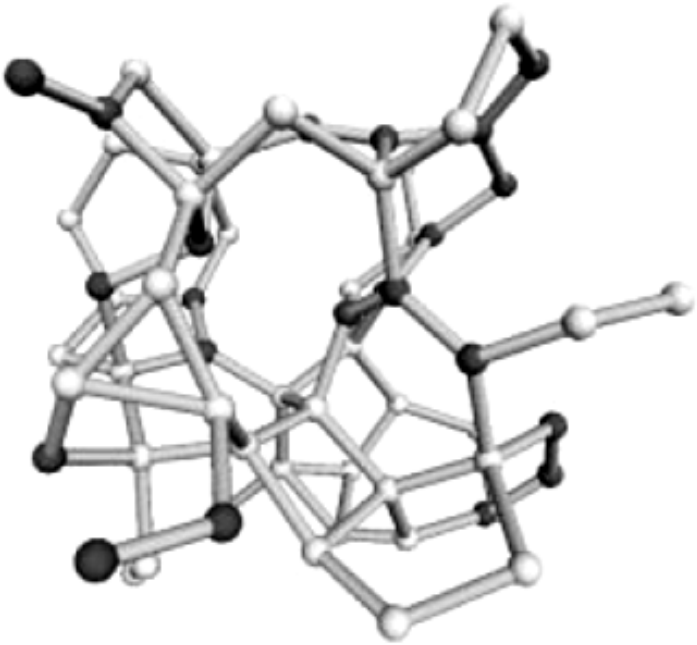

Fig. 2.8: Model of the 64 atom *ta*-C network with 22 three-fold coordinated atoms (sp^2 hybridized) (dark spheres) and 42 four-fold coordinated atoms (sp^3 hybridized) (light spheres). Figure adapted from Ref. [92].

d. Graphite - graphene

Graphite is a 3D crystalline structure which consists of stacked graphene layers (sheets). These sheets are held together by weak van der Waals forces with the interlayer distance $\sim$ 0.335 nm [93] which allows graphene sheets to be easily separated or slide past each

other. There are three common forms of graphite with different types of stacking order (hexagonal, rhombohedral and turbostratic) which have very similar physical properties. For turbostratic structure, there is no discernible stacking order. For hexagonal structure, it is characterized by AB or Bernal stacking with 4 carbon atoms per unit cell while ABC stacking contains 6 carbon atoms per unit cell in a Rhombohedral structure as illustrated in Fig. 2.9.

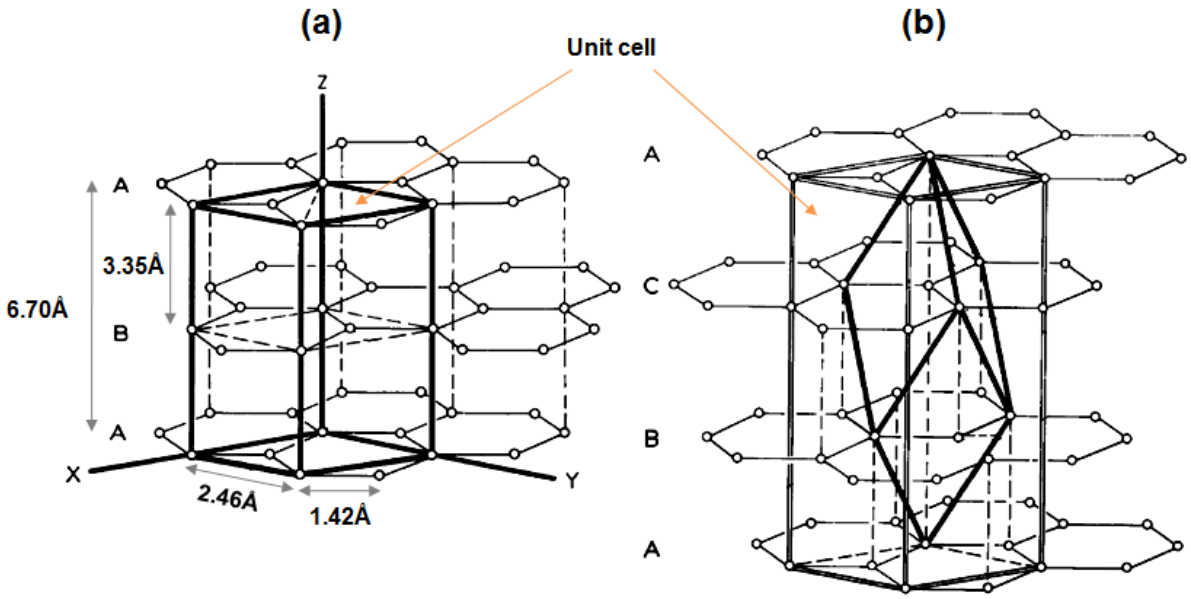

Fig. 2.9: (a) Hexagonal and (b) Rhombohedral lattice of graphite with different types of stacking order. Figures (a) and (b) adapted from Ref. [93].

As observed, carbon atoms in layer B sits directly above the center of a carbon ring of the layer A in the hexagonal structure. In the rhombohedral structure, the center of a carbon ring in the layer A sits directly below a corner of a carbon ring in the layer B, which is in turn directly below a nonequivalent corner of a carbon ring in the layer C.

Graphene can be described as a single atomic layer isolated from graphite. Unlike graphite, graphene is a quasi-two dimensional lattice in which carriers can only move in 2D and are described as massless Dirac fermions in contrast with massive carriers in normal metals and semiconductors. It possesses a series of unique properties as mentioned earlier that are related to its honeycomb structure. Carbon atoms are linked

by a chain of strong covalent sp^2 bonds which give rise to interesting conductivity of graphene. Fig. 2.10 (b) shows the crystal structure of graphene along with a unit cell in real space formed by basis vectors $\mathbf{a}_1$ and $\mathbf{a}_2$.

$$\mathbf{a}_1 = a\left(\frac{\sqrt{3}}{2}, \frac{1}{2}\right), \mathbf{a}_2 = a\left(\frac{\sqrt{3}}{2}, -\frac{1}{2}\right) \tag{2.11}$$

where a = $|\mathbf{a}_1| = |\mathbf{a}_2| = 2.46$ Å is the lattice constant (the distance between adjacent unit cells). In graphene, each unit cell contains two inequivalent carbon atoms which

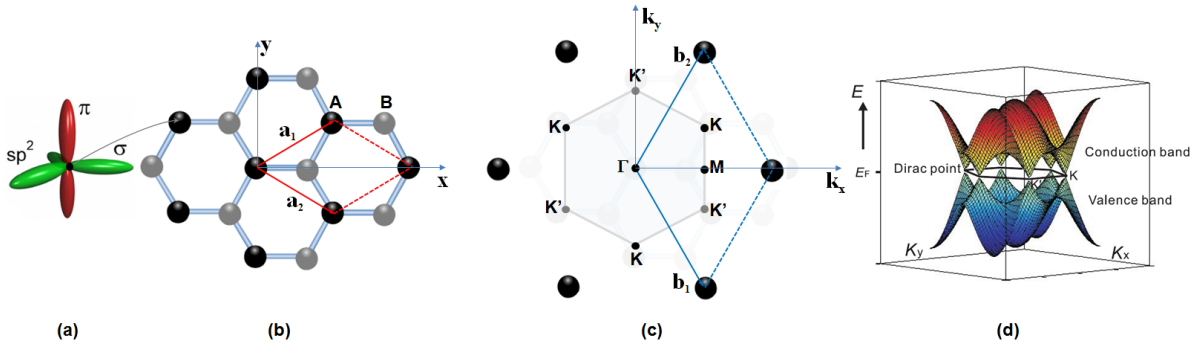

Fig. 2.10: (a) The sp^2 bonds of (b) Graphene lattice in real space with two lattice vectors $\mathbf{a}_1$ and $\mathbf{a}_2$; (c) Sketch of the first Brillouin zone in the reciprocal lattice: (d) The electronic band structure of graphene. Images (a) adapted from Ref. [94] and (d) adapted from Ref. [95].

are often labelled A and B (sublattices) because it is not possible to connect them with a lattice vector [96]. Fig. 2.10 (c) shows the two reciprocal lattice vectors $\mathbf{b}_1$ and $\mathbf{b}_2$ (k-space) given by

$$\mathbf{b}_1 = \frac{2\pi}{a}\left(\frac{\sqrt{3}}{2}, \frac{1}{2}\right), \mathbf{b}_2 = \frac{2\pi}{a}\left(\frac{\sqrt{3}}{2}, -\frac{1}{2}\right) \tag{2.12}$$

Their magnitude is

$$|\mathbf{b}_1| = |\mathbf{b}_2| = \frac{2\pi}{a} \tag{2.13}$$

Therefore, the boundary of the first Brillouin zone of a graphene lattice can be generated as in Fig. 2.10 (c) and its symmetry points are defined in Table 2.2 together with the corresponding electron band structure (Fig. 2.10 (d)).

For multilayer graphene ($\leq$ 10 layers [97]), graphene layers can be stacked in different

Point	K	K'	M	Γ
k-vector	$\frac{2\pi}{a}\left(\frac{1}{\sqrt{3}}, \frac{1}{3}\right)$	$\frac{2\pi}{a}\left(\frac{1}{\sqrt{3}}, -\frac{1}{3}\right)$	$\frac{2\pi}{a}\left(\frac{1}{\sqrt{3}}, 0\right)$	$(0, 0)$

Table 2.2: A list of the special points in the Brillouin zone along with their associated vector in k-space. The Γ point is referred to as the zone center.

sequences. The electronic properties of graphene change with the number of layers and the stacking order. As the number of layers increase, the stacking order can become more complicated, as in graphite. For example, in a lattice of bi-layer graphene, the stacking order can be either AA (each atom on top of another atom) [98] or AB (atoms in the second layer sits over the center of the hexagon in the first layer) [99]. For tri- and tetra-layer graphene, it can stack as ABA [100, 101], ABC [102, 103], ABAC [104], ABCB [105] or random stacking (turbostratic) [106, 107].

2.3.4. Summary

Structural properties of relevant materials are summarized in Table 2.3.

Parameters	Si	Si(111)	3*C*-SiC	3*C*-SiC(111)	6*H*-SiC	4*H*-SiC	*a*-C	graphite	graphene
Structure	d.c.	hex.	cubic	hex.	hex.	hex.	free	hex./rhom.	hex.
Band gap (eV)	1.12	1.12	2.3	2.3	3.0	3.3	-	0.04 [108]	gapless
Lat. constant a (Å)	5.43	3.84	4.36 [109]	3.08 [109]	3.08 [109]	3.08 [109]	-	2.46	2.46
Lat. constant c (Å)	-	9.41 [110]	-	7.55 [109]	15.11 [109]	10.08 [109]	-	6.70/10.04 [93]	-
Stacking order	-	AaBbCcAa [111]	-	**ABCA**	**ABCA**CBA	ABACA	-	ABA/ABCA	AA/AB/ABC /ABAC/ABCB/ turbostratic

Table 2.3: Structural properties of relevant materials; d.c. is diamond cubic, hex. is hexagonal and rhom. is rhombohedral.

2.4. Sample preparation

2.4.1. Principle of e-beam evaporation

Electron beam evaporation is a type of physical vapor deposition [112] described schematically in Fig. 2.11. A solid target is bombarded directly by an electron beam from a hot filament (tungsten - W) in ultra high vacuum. The electron beam generates heat, which causes atoms from the target to transform into the gaseous phase and then to precipitate on the substrate.

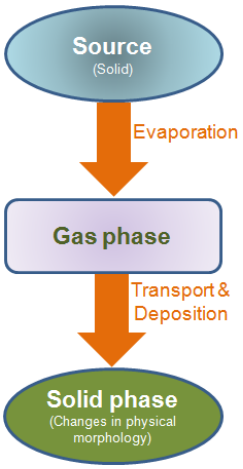

Fig. 2.11: Flow diagram of physical vapor deposition.

a. Evaporation and deposition rates

According to the kinetic theory of gases, the evaporation flux (Φ_{evap}) from a solid is given by Hertz-Knudsen law [113]:

$$\Phi_{evap} = \frac{dN_{evap}}{A_{evap}dt} = \frac{\alpha_{evap}N_A\left(P_{evap} - P_h\right)}{\sqrt{2\pi MRT}} \tag{2.14}$$

where N_{evap}, A_{evap}, α_{evap}, P_{evap}, P_h, M, R, N_A, and T are number of evaporated atoms (dimensionless), the area of the evaporation source (m^2), the coefficient of evaporation ($0 \leq \alpha_{evap} \leq 1$), the equilibrium vapor pressure of the evaporated material (N/m^2), the hydrostatic pressure acting on the evaporant (N/m^2), the molar mass (kg/mol), the ideal gas constant (J/mol.K), *Avogadro's* number, and the temperature of the material (K), respectively;

When $\alpha_{evap} = 1$ and P_h =0, the evaporation flux is maximum. An expression for the maximum value of Φ_{evap} is

$$\Phi_{evap} = \frac{dN_{evap}}{A_{evap}dt} = \frac{N_A P_{evap}}{\sqrt{2\pi MRT}} = \sqrt{\frac{N_A}{2\pi k_B MT}}P_{evap} \tag{2.15}$$

where k_B is the Boltzmann's constant (J/K).

For an electron beam evaporation, the heating power of the source is expressed by

$$W = I_e U_{HV} \tag{2.16}$$

where I_e, U_{HV} are the emission current (A), the high voltage for heating the rod (V), respectively.

This power is mostly radiated according to Stefan - Boltzmann:

$$W = \sigma A_{evap} T^4 \tag{2.17}$$

where $\sigma = 5.67 \times 10^{-8}$ W/m^{2}K^4 is the Stefan - Boltzmann constant.

Combining equation (2.16) and (2.17), we have:

$$T = \sqrt[4]{\frac{I_e U_{HV}}{\sigma A_{evap}}} \tag{2.18}$$

For example, if $W \sim 100$ W and $Aevap \sim 10^{-4}$ m^2, the temperature of the evaporated material is found T $\sim$ 2050 K.

In general, we can control the evaporation rate by changing the source power.

- As $N_A = 6.023 \times 10^{23}$mol^{-1}, $k_B = 1.38 \times 10^{-23}$J/K, the molar mass M in g/mol and P_{evap} in mbar, the evaporation flux Φ_{evap} in number of atoms/cm^2.s is rewritten:

$$\Phi_{evap} = 2.64 \times 10^{22} \frac{P_{evap}}{\sqrt{MT}} \tag{2.19}$$

- For a typical thickness of monolayer (1 ML) $\sim 10^{15}$ atoms/cm^2, the evaporation flux Φ_{evap} close to the source in ML/s becomes:

$$\Phi_{evap} = 2.64 \times 10^{7} \frac{P_{evap}}{\sqrt{MT}} \tag{2.20}$$

From (2.19) we can describe this evaporation rate in mass (g/cm^2.s) by multiplying the flux with the molar mass M (g/mol) as

$$R_{evap} = \Phi_{evap} M = 4.4 \times 10^{-2} \sqrt{\frac{M}{T}} P_{evap} \tag{2.21}$$

- The vapour pressure P_{evap} is determined by using Clausius - Clapeyron equation as

$$P_{evap} = Ke^{-\frac{\Delta H}{RT}} \tag{2.22}$$

- For a given material, the value K can be calculated by

$$K = P_0 e^{\frac{\Delta H}{RT_{boiling}}} \tag{2.23}$$

where ΔH, R, P_0 and $T_{boiling}$ are the vaporization enthalpy (J/mol), the ideal gas constant (J/mol.K), the standard pressure (1.013×10^5 Pa) and the boiling temperature (K), respectively. The values of ΔH and $T_{boiling}$ for different materials can be found in Ref. [114].

For most elements, $R_{evap} \sim 10^{-4}$ g/cm^2.s at $P_{evap} \sim 10^{-2}$ mbar [113].

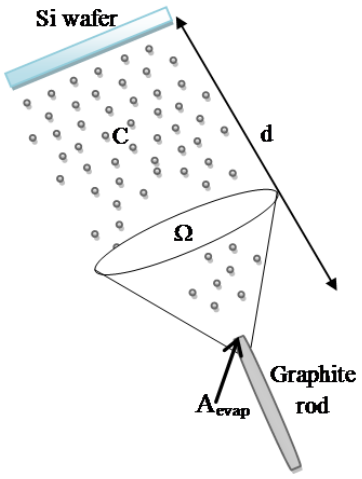

Fig. 2.12: Geometry of carbon evaporation.

Therefore, the mass of the evaporated material in time is

$$M_{evap} = \int_0^t \int_0^{A_{evap}} R_{evap} dA dt \tag{2.24}$$

Likewise, in order to govern the deposition rate at the wafer surface, the position and

the direction of the wafer in the chamber is depicted as Fig. 2.12.

$$R_{dep} = \frac{R_{evap} A_{evap}}{\Omega d^2 \rho} \cos\theta \tag{2.25}$$

where ρ, Ω, A_{evap} and d are the density of the deposited material (g/cm^3), the solid angle of the evaporation source (steradian), the area of the evaporation source (m^2) and the distance from the top of the rod to the wafer surface (m), respectively; $\theta \sim 0°$ (the wafer surface is perpendicular to the source). The flux is considered uniform in Ω [115].

Experimentally, the deposition rate R_{dep} can be calibrated using a quartz oscillator which is placed at about 10 cm in front of the source in the UHV chamber. Changes in the resonant frequency Δf of the quartz oscillator during deposition are related to the thickness of the deposited films on the surface of the quartz [116]:

$$\ell = -\frac{v_q \rho_q \Delta f}{2\rho_g f^2} \tag{2.26}$$

where v_q, ρ_q, ρ_g, and f are the velocity of longitudinal waves in quartz (m/s), the densities of quartz and graphite (kg/m^3), and the initial resonance frequency of the quartz oscillator (Hz), respectively.

For $v_q = 5900$ m/s, $\rho_q = 2650$ kg/m^3, $f = 6 \times 10^6$ Hz, the thickness ℓ from the equation (2.26) can be rewritten by

$$\ell = 22 \times 10^{-8} \frac{|\Delta f|}{\rho_g} \tag{2.27}$$

The density of graphite $\rho_g = 2230$ kg/m^3, so the film thickness can be easily determined from the equation (2.27) by measuring Δf.

b. Evaporation sources

Evaporation source is a filament which is made of a coiled tungsten wire consisting of several turns surrounding an electrically conducting target (crucible or rod). It emits electrons which are accelerated across a high voltage towards the evaporant target, hence providing the necessary heating power.

c. Evaporation materials

Evaporant materials can be one of the following two common forms [115]:

- Crucible form: The material is put in a conducting crucible made from a material with high melting point and low vapour pressure, which is heated by electron bombardment causing the contents to evaporate. *It is generally preferable for insulators or other poor electrical conductors and for materials with low melting point.*
- Rod form: The material in rod form is located in the middle of the evaporator body which is directly bombarded by electrons and then, rapidly rises to evaporation temperature. As material is evaporated, more can be fed into the evaporation zone by using the linear motion feedthrough. *It is suitable for conducting materials with high melting point.*

For this study, carbon is deposited using an e-beam evaporator from Tectra GmbH with a graphite rod of 99.997% purity from Goodfellow Cambridge Ltd.

d. E-beam power and deposition rate

The power supply of e-beam evaporator can reach an electron beam power up to $\sim$ 600 W. Deposition rate can be from sub-monolayers per minute up to several nm per second [115].

e. Advantages and disadvantages

- Advantages: It is possible to grow purest films because only the evaporant is heated in UHV chamber. The flux is stable, controllable, highly uniform over an area with the diameter of $\sim$ 4.5 cm in front of the source.

- Disadvantages: Due to degradation of the filament, it is impossible to keep the evaporation rate constant after an extended period.

2.4.2. Experimental setup

a. Main components needed to setup the experiment using graphite rod form of evaporation

Fig. 2.13 shows a typical e-beam evaporator of Tectra together with the basic components as follows:

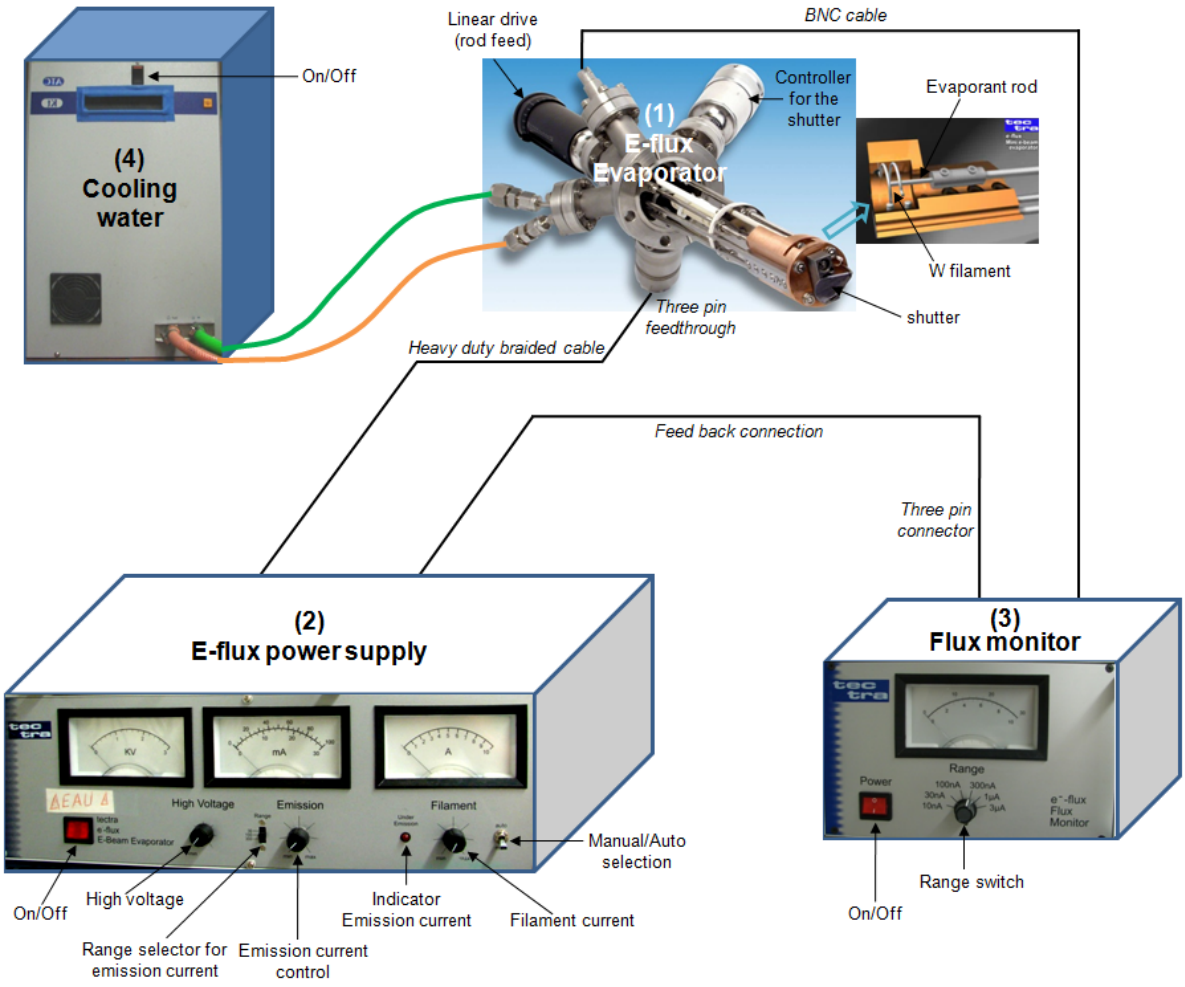

Fig. 2.13: Main components of our e-beam evaporator.

(1) E-flux evaporator *consists of a graphite rod (a max. length of* ~ 5 *cm and a standard diameter of* ~ 2 *mm), a coiled tungsten filament and shutter drive for opening and*

closing the flux.

(2) E-flux power supply *for providing a high voltage to the graphite rod during operation which extracts an electron current from a nearby hot filament and then, raises the temperature to create a hot tip on the graphite rod.*

(3) Flux monitor *for collecting the ions from carbon atoms which were ionised by the incoming electron beam and thus, generates a small positive current which is related in magnitude to the carbon flux.*

(4) Water cooling *reduces outgassing from surrounding areas.*

b. Principle of operation

Fig. 2.14 (a) shows several steps to get carbon evaporation by using the graphite rod form.

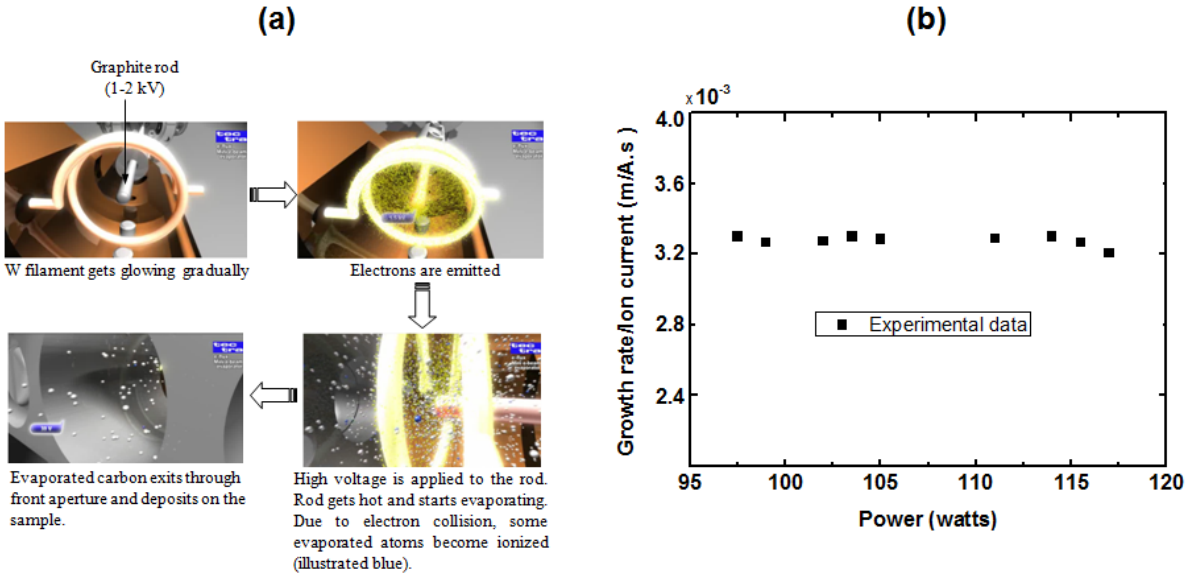

Fig. 2.14: (a) A simulation process for carbon evaporation from the graphite rod form (Source from Tectra company [115]; (b) The ratio between deposition rate and ion current as a function of the heating power were measured at the position $d \sim 10$ cm, HV = 1.5 - 1.6 kV, $I_F = 8$ A and $I_e = 60$ - 80 mA with the vapour pressure $\sim 10^{-5}$ - 10^{-4} mbar calculated using equation (2.22) (the gauge reading pressures $\leq 6.0 \times 10^{-8}$ mbar).

In principle, a filament surrounding the graphite rod will emit hot electrons when a filament current of 7 - 8 A is applied. Then, these electrons will bombard directly the

graphite rod tip due to a positive high voltage. As a result, the graphite rod will be locally heated to very high temperature and a continuous flux of carbon atoms will be produced. By adjusting the high voltage and the emission current, a stable and controllable carbon flux can be obtained. During evaporation, some carbon atoms will become ionised (illustrated blue) due to electron collision. They will be collected by a negatively biased electrode at the front aperture. This ion current is a measure of the deposition rate of carbon atoms by using the quartz oscillator on the wafer surface as shown in Fig. 2.14 (b).

Due to carbon evaporation, the rod will become shorter and so, a higher filament current will be required to maintain the same flux. When the rod becomes very short and far away from the center of the filament, it may also be necessary to increase the power to maintain the flux.

c. Experimental conditions for carbon evaporation

After the high voltage is set at 1.5 kV with the emission current at zero, we increase gradually the filament current (I_F). Once I_F reaches 7 - 8 A, there are two possibilities for the emission current (I_e) as follows:

- I_e should be seen to rise until the LED *(under emission)* goes out [3].
- If no emission current is observed, the graphite rod may be too far away from the filament. In this case, we should drive the rod forward slowly. Once it is penetrated further into the evaporator body, the emission current must rise. The best position is $\sim$ 1 - 2 mm further than the position where the emission current starts to rise.

Then, we turn the "*Emission*" dial clockwise about 10 - 15 mA until the LED lights up. At this moment, we turn the "*Filament*" dial slightly clockwise until the LED goes out again. This may be enough power to evaporate carbon. For the graphite rod, the emission current should be more than 60 mA at 1.5 kV for carbon evaporation according to our experimental procedure.

[3]The LED is an indicator which shows that selected emission current can not reach at highest allowed filament current.

2.5. Experimental techniques

2.5.1. Ultra-high vacuum

Ultra-high vacuum (UHV) is characterized by pressures lower than 10^{-9} mbar. At such low pressures, the mean free path (MFP) of a gas molecule is approximately hundred kilometers by the equation [117]

$$\lambda = \frac{1}{\sqrt{2}\pi d^2 n} = \frac{k_B T}{\sqrt{2}\pi P d^2} \tag{2.28}$$

where d, n, k_B, P and T are the molecular diameter (m), the number of molecules per m^3, Boltzmann′s constant, the pressure (Pa) and the temperature (K) in the chamber.

It means that gas molecules will collide with the chamber walls many times before colliding with each other. Therefore, almost all interactions take place on various surfaces in the chamber.

The samples under investigation are subject to surface contamination arising from the adsorption of molecules that comes mostly from desorption of water or other adsorbed gases from the walls of the chamber and from outgassing from other internal surfaces. Buildup of such contamination is a function of the pressure in the chamber, according to Hertz-Knudsen equation (2.15). For example,

- at $P \sim 10^{-6}$ mbar, it takes about one second to adsorb one molecule thick layer (1 ML) on a reactive surface.
- at $P \sim 10^{-10}$ mbar, it takes about 10^4 seconds (2.75 hours) for 1 ML to form on the same surface.

Obviously, lower pressure leads to less contaminantion. Therefore, UHV is necessary whenever surface contamination must remain low for a prolonged period.

At LPME, the UHV chamber is equipped with STM (VP2 from Park Instrument), AES (Omicron), LEED (Omicron) and RHEED (Riber) for surface characterization of the sample.

2.5.2. Low energy electron diffraction (LEED) and reflection high energy electron diffraction (RHEED)

a. Principle of LEED and RHEED

LEED and RHEED are two effective tools for analyzing the surface structure of solids, including thin films. In this section, we will present their useful aspects on how to determine the lattice constant of our materials.

The principle of these two techniques is based on the theory of electron/X-ray diffractions which can be found in Refs. [118, 119]. Fig. 2.15 shows the typical schematic of the incident beam diffraction leading to a special case of LEED. Due to the normal incidence

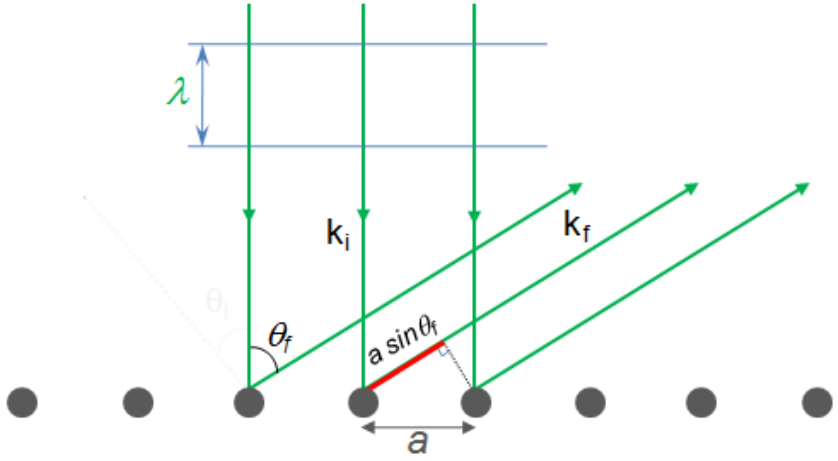

Fig. 2.15: Electron diffraction in the case of LEED with incident electron beam normal to the surface ($\mathbf{k}_i$ and $\mathbf{k}_f$ are the incident wavevector and the scattered wavevector, respectively).

of the incoming beam ($\theta_i = 0$), the diffraction condition becomes:

$$a\sin\theta_f = n\lambda \tag{2.29}$$

Therefore, the lattice constant a can be given by

$$a(\text{nm}) = \frac{n\lambda}{\sin\theta_f} = \frac{1.23}{\sqrt{E}} \cdot \frac{n}{\sin\theta_f} \tag{2.30}$$

where $n \in N_0$ is the diffraction order; E is a beam energy of incident electrons (eV); θ_f

is diffracted angle with respect to the surface normal which can be easily calculated by measuring some relevant parameters from the experiment [120] as described in Fig. 2.16 (a).

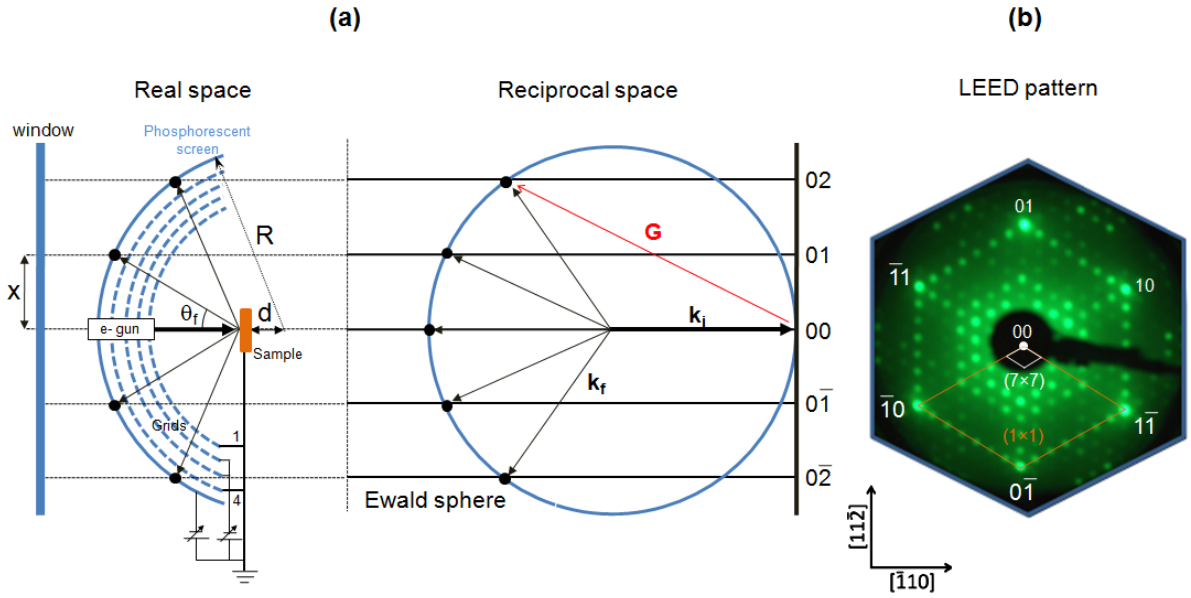

Fig. 2.16: (a) Real and reciprocal space of electron diffraction (**G** is the reciprocal lattice vector which is related to $\mathbf{k}_i$ and $\mathbf{k}_f$ as section 2.3.2). The spots induced by the diffraction beams are labelled by (00), (01), etc.; (b) LEED pattern of Si(111) 7×7 surface reconstruction at 38 eV.

From the geometry described in Fig. 2.16 (a), we can deduce that

$$\theta_f = \text{arctg}\left(\frac{x}{\sqrt{R^2 - x^2} - d}\right) \tag{2.31}$$

where x, R, and d are the distance between the screen center and the first diffraction spot, the spherical radius of the screen, the distance from sample to the optical center of the screen, respectively. Technical data of the SpectalLEED are presented in detail in Ref. [120].

b. LEED geometry

In our LEED system, the electron beam is produced from a LaB_6 filament. Energy can be adjusted between 30 and 200 eV, corresponding to a wavelength between 0.225 and 0.123 nm. The diffracted electrons (elastically scattered) produce spots on a fluorescent screen while the secondary electrons (inelastically scattered) produce only diffuse background. The sample is grounded (Fig. 2.16 (a)). A series of grids is used to suppress the inelastic background. After passing through grid 1 (ground), the electrons are accelerated towards the screen. Negative potential applied to grids 2 and 3 (suppressor grids) repel secondary electrons while grid 4 is grounded to reduce field penetration of the screen to the suppressor grids when a high voltage is applied to the screen in order to render the diffraction beams visible. Electrons strike the phosphor to emit photons and the image is captured through a window by using a video camera.

c. RHEED geometry

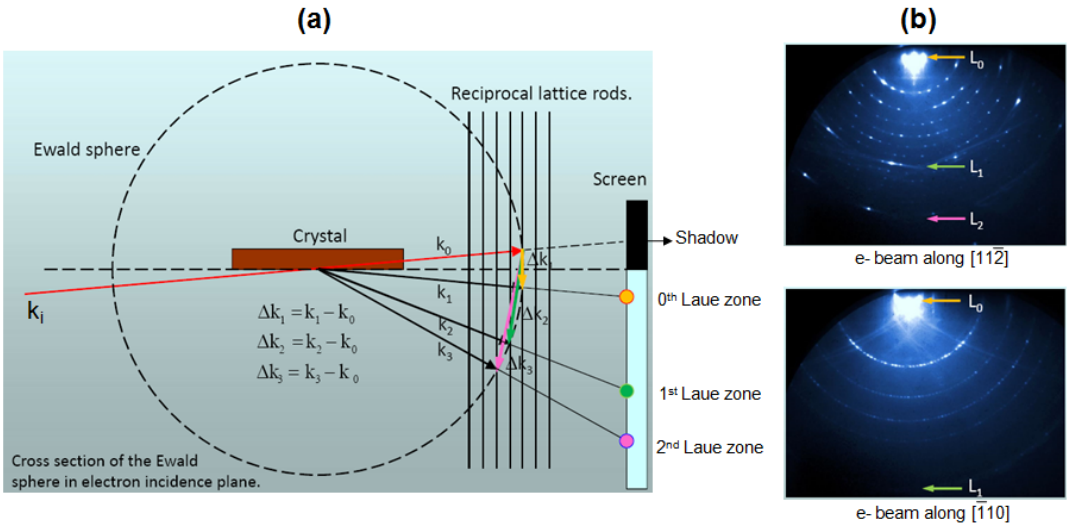

Fig. 2.17: (a) A typical RHEED geometry with a description of the intersection between the Ewald sphere and the reciprocal lattice rods; (b) RHEED patterns of Si(111) 7×7 surface reconstruction with an e-beam along different directions from corresponding reciprocal lattices as constructed in section 2.3.3.a. Images adapted from Ref. [121].

Unlike LEED, electrons emitted from an electron gun in RHEED are incident upon a sample at a grazing angle of $\sim$ 1 - 3° (side-on projection) with an energy of typically 10 keV and emerge as a series of diffracted beams which are observed on a phosphor-coated screen. A typical RHEED geometry is illustrated in Fig. 2.17.

- **Interpretation of the RHEED patterns**

  RHEED patterns can be classified into reflection and transmission patterns [122]. For single crystal films, both kinds of patterns are often observed depending on surface morphology. However, for polycrystalline films (consist of various randomly oriented islands), the transmission patterns are usually observed. In order to interpret how the patterns form, let's consider the following specific cases.

  – **For a smooth single crystal surface**

    In this case, electrons are reflected completely from the surface *(reflection mode)*. Direction of diffracted beams is obtained from an Ewald sphere can be constructed in the reciprocal space composed of a set of one-dimensional rods perpendicular to the surface (Fig. 2.18 (a)).

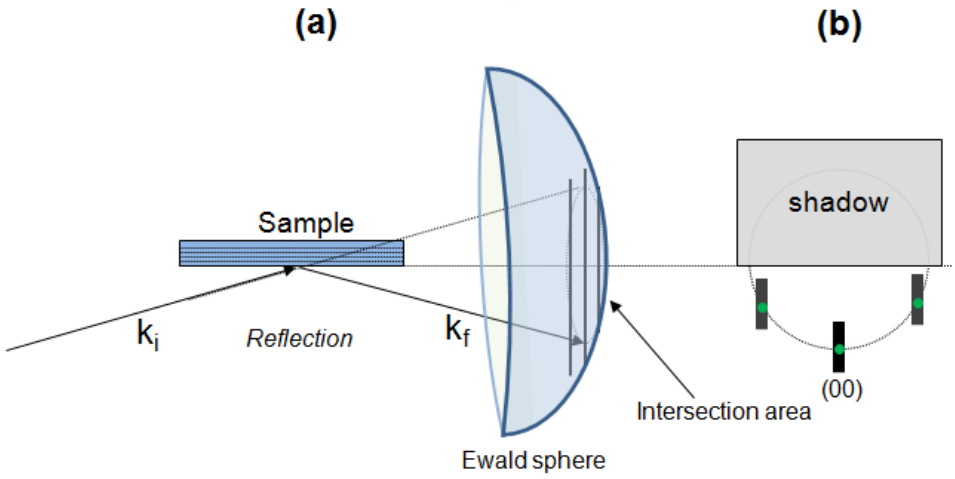

Fig. 2.18: Schematic of electron scattering geometry on single crystalline film with smooth surface.

These rods are often broadened because of imperfections in the surface and temperature dependent fluctuation [122]. The intersection of the Ewald sphere

with each reciprocal rod will produce a reflected beam that is elongated into a streak. These streaks are arranged on so-called Laue circles. In Fig. 2.18 (b), the dashed circle illustrates the 0^{th} Laue circle. In RHEED geometry, only the lower part of the diffraction pattern can be observed because the upper part is shadowed by the substrate. The specular diffraction streak is labelled as (00).

– **For a single crystal film with islands**

Fig. 2.19 (a) shows some islands with identical orientation. Besides electrons reflected from the surface, most of them enter the crystalline islands from one surface and are scattered out through another surface *(transmission mode)*. Because diffraction occurs through three-dimensional objects, the reciprocal space is composed of dots. Thus, the corresponding diffraction pattern consists of spots (Fig. 2.19 (b)). The specular spot is usually missing in the RHEED transmission pattern due to the interference of electron scattering from different atomic layers perpendicular to the surface [123].

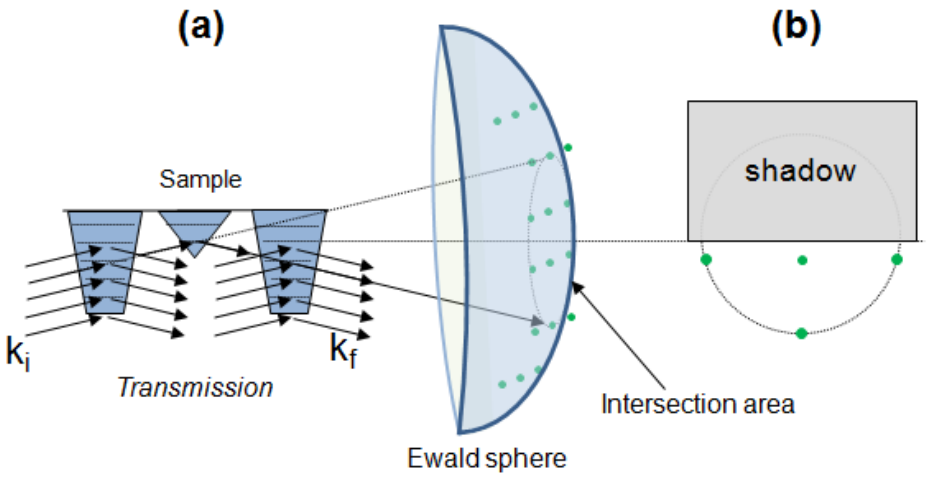

Fig. 2.19: Schematic of electron scattering geometry on single crystalline film with islands.

– **For a polycrystalline film**

Because it contains many different crystallites with different orientations (islands), the film is usually rough. In this case, the electrons penetrate through

crystallites and a diffraction pattern of transmitted electrons is formed as shown in Fig. 2.20 (a). All islands have their own crystallographic orientation and are not coherently related to each other. Therefore, the reciprocal space is a sum of individual reciprocal spaces with different orientations. If the crystallites are randomly oriented, the reciprocal space structure can be viewed as a set of concentric spheres. One of these spheres is shown in dark grey centered at the origin of the reciprocal space which is located at the end of $\mathbf{k}_i$. The intersection of the Ewald sphere with each reciprocal sphere produces a circle, called the Debye ring [122]. The corresponding diffraction pattern consists of concentric rings (Fig. 2.20 (b)).

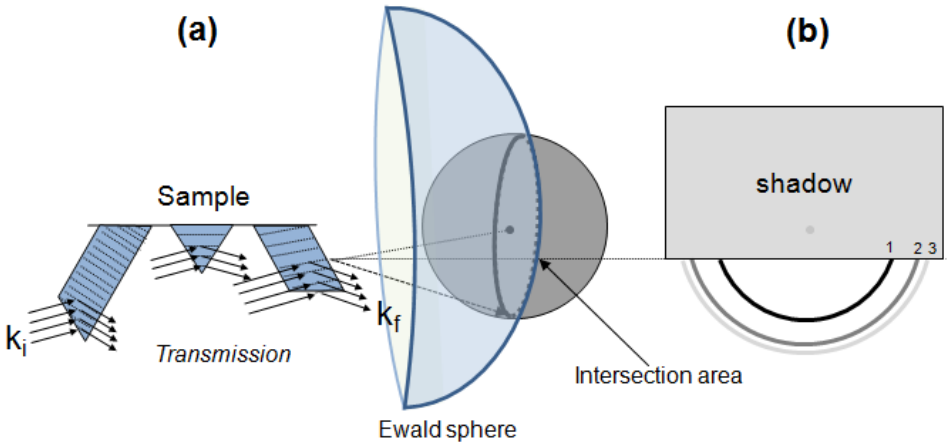

Fig. 2.20: Schematic of electron scattering geometry on polycrystalline film.

- **How to determine the lattice constant by RHEED**

  We start with Bragg's law,

$$2d_{hkl}\sin\alpha = n\lambda \tag{2.32}$$

  where d_{hkl}, λ, α, and n are the lattice spacing with (hkl) Miller indices, the incident electron wavelength, the incident angle, and the order of diffraction ($n \in N_0$), respectively.

  One can consider that the reflection is normally strongest from the first-order plane (n=1) and the reflected intensity decreases as n increases [119]. Thus, Bragg's condition is rewritten as

$$2d_{hkl}\sin\alpha = \lambda \tag{2.33}$$

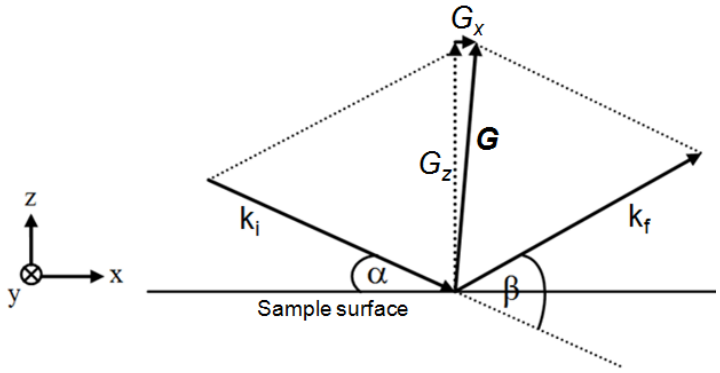

Fig. 2.21: Graphical representation of the scattering vector.

In the geometry of Fig. 2.21, the scattering vector $\mathbf{G}$=$\mathbf{k}_f$-$\mathbf{k}_i$ is given by [123]

$$\begin{pmatrix} G_x \\ G_y \\ G_z \end{pmatrix} = \begin{pmatrix} \frac{4\pi}{\lambda}\sin\left(\frac{\beta}{2}\right)\sin\left(\alpha-\frac{\beta}{2}\right) \\ 0 \\ \frac{4\pi}{\lambda}\sin\left(\frac{\beta}{2}\right)\cos\left(\alpha-\frac{\beta}{2}\right) \end{pmatrix} \tag{2.34}$$

where β is the total angle of deflection from the initial beam.

In the case of symmetric diffraction ($\beta = 2\alpha$), it reduces to

$$\begin{pmatrix} 0 \\ 0 \\ \frac{4\pi}{\lambda}\sin\alpha \end{pmatrix} \tag{2.35}$$

so that Bragg's law can be written as

$$d_{hkl} = \frac{2\pi}{G_z} \tag{2.36}$$

Depending on the kind of structure, the lattice spacing is given by [119]

- $\frac{1}{d_{hkl}^2} = \frac{4}{3}\cdot\frac{h^2+hk+k^2}{a^2} + \frac{l^2}{c^2}$ for hexagonal structure.
- $\frac{1}{d_{hkl}^2} = \frac{h^2+k^2+l^2}{a^2}$ for cubic structure.
- $\frac{1}{d_{hkl}^2} = \frac{h^2+k^2}{a^2} + \frac{l^2}{c^2}$ for tetragonal structure.
- etc.

where a, c are the lattice constants; h, k, l are the Miller indices.

Hence, for a cubic structure, Bragg's law is expressed as

$$G_z = 2\pi\sqrt{\frac{h^2+k^2+l^2}{a^2}} \tag{2.37}$$

From (2.35) and (2.37), the lattice constant of the film will be

$$a = \frac{\lambda\sqrt{h^2+k^2+l^2}}{2\sin\alpha} \tag{2.38}$$

Similarly, for a hexagonal structure, Bragg's law is expressed as

$$G_z = 2\pi\sqrt{\frac{4}{3}\cdot\frac{h^2+hk+k^2}{a^2}+\frac{l^2}{c^2}} \tag{2.39}$$

From (2.35) and (2.39), the lattice constant of the materials can be determined by using corresponding RHEED patterns. For the following examples,

- **For a single crystalline film (2D)**

  Because electrons are reflected only from the surface, $\mathbf{k}_i$ is drawn with its end on a node of the reciprocal space. This point is indexed as (00); it corresponds to a diffracted beam in the plane and perpendicular to the surface containing the incident beam, while other spots are characterized by end points of diffracted beams as (01), $(0\bar{1})$ and so on.

  In this case, we can obtain the lattice constant for the hexagonal structure as

  $$a = \frac{\lambda}{\sin\alpha}\sqrt{\frac{h^2+hk+k^2}{3}} \tag{2.40}$$

  If $r \ll L$, $\sin\alpha \approx \alpha = \frac{r}{2L}$

  Hence,

  $$a = \frac{2\lambda L}{r}\sqrt{\frac{h^2+hk+k^2}{3}} \tag{2.41}$$

  where L, r are the distance between the sample and the screen, the distance between two nearest streaks, respectively.

  For example, Fig. 2.22 (b) shows a RHEED pattern from a $3C$-SiC film on

Si(111) ($\lambda = 0.12$ Å (10 keV), $r \sim 1.48 \pm 0.1$ cm; $L = 33.48 \pm 0.1$ cm), the lattice constant of carbide film is then found to be: $a = 3.13 \pm 0.19$ Å (very close to the expected value of 3.08 Å for SiC film).

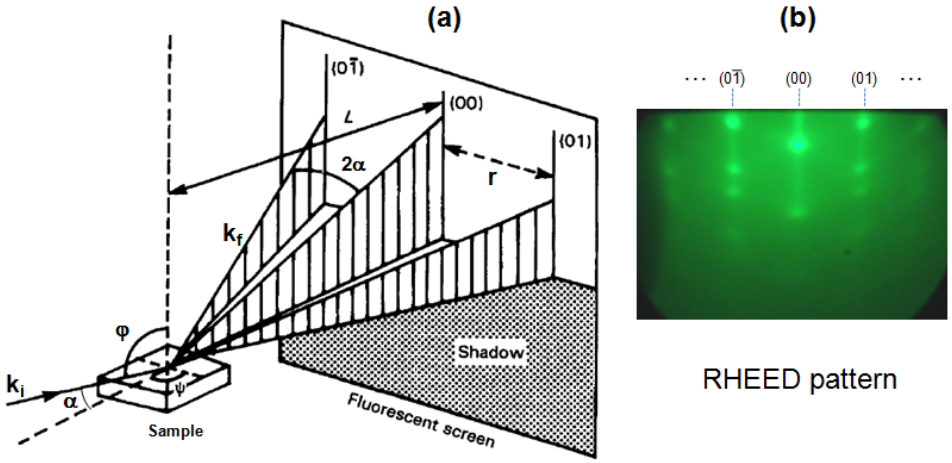

Fig. 2.22: (a) A construction of RHEED geometry for determining the lattice constant of a single crystalline films; (b) RHEED pattern of $3C$-SiC formation on Si(111). Image (a) adapted from Ref. [124].

– **For a polycrystalline film (3D)**

Diffraction rings appear in the RHEED image, indicating that the deposited carbon is really polycrystalline material. In other words, the film comprises many small domains with different crystallographic orientations. So, the reciprocal space contains individual reciprocal spaces with different orientations. In the case of graphitic carbon films on Si(111), it is expected that individual crystals have a hexagonal structure. For a reciprocal lattice point with indices $(hkil)$ [4], the corresponding sphere appears at $|\mathbf{G}| = G_z$ given by equation (2.39).

On the other hand, the diffraction ring is given by

$$\beta = 2\alpha = \frac{R}{L} \tag{2.42}$$

where α is very small, R is the ring radius, and L is the distance from the

[4]Where i is defined by h+k=-i as the third index in order to describe a crystallographic plane in the hexagonal structure.

sample to the phosphor screen.

Combining (2.42) with the Bragg condition, the lattice spacing will be found

$$d_{hkil} = \frac{\lambda L}{R} \tag{2.43}$$

where L, λ are known, R is measured directly on the screen.

From (2.39) the expected radii G_e (theory) can be calculated along with the measured radii G_m (experiment). Therefore, it is possible to determine the lattice constant for the film (see section 4.3.2.c).

For example, a RHEED pattern of one of our materials was produced at the substrate temperature of 1000 °C with diffraction rings as shown in Fig. 2.23.

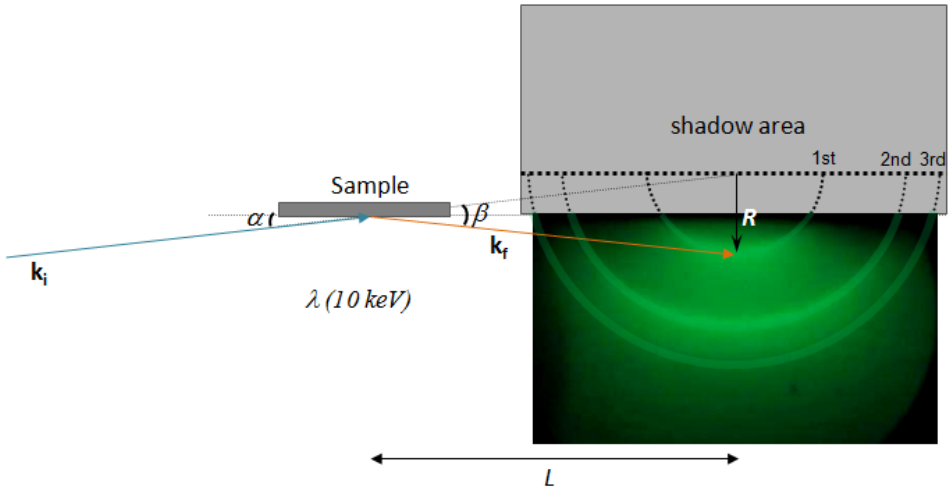

Fig. 2.23: A typical RHEED pattern of polycrystalline graphene on Si(111).

2.5.3. Auger electron (AE) and X-ray photoelectron (XP) spectroscopies

a. Principle of AES and XPS

Auger electron and X-ray photoelectron spectroscopies are powerful tools for analysis of the chemical composition of surfaces. The basic principle of these techniques are summarized below.

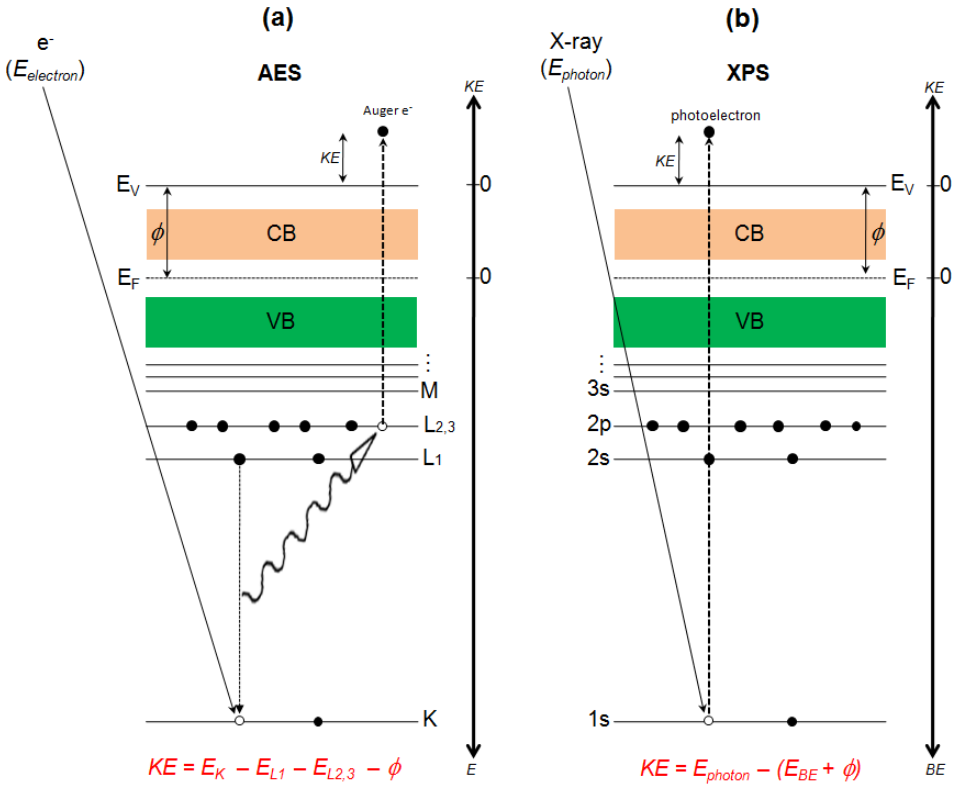

Fig. 2.24: The mechanism of AES and XPS processes.

In AES, an incident electron (typically $E_{electron} = 3$ keV) or another energetic particle (Fig. 2.24 (a)) excites the atoms causing emission of an electron and leaving a hole vacancy. An electron from a level with lower binding energy drops down to fill this vacancy. As a result of this, the energy released causes the emission of an Auger electron with a kinetic energy

$$KE = E_K - E_{L1} - E_{L2,3} - \phi, \tag{2.44}$$

where ϕ is the work function (eV).

In XPS, excitation of the atom is caused by photons (X-ray) (Fig. 2.24 (b)) resulting in the escape of photoelectrons into vacuum with a kinetic energy

$$KE = E_{photon} - (E_{BE} + \phi), \tag{2.45}$$

where ϕ and E_{BE} are the work function (eV) and the binding energy (eV), respectively.

In general, the kinetic energy is different for each element of the periodic table and

depends on the energy levels of the hole. When the Auger electrons or photoelectrons are collected, various peaks appear on the spectra:

- *For AES,* Auger electron transitions are usually designated by three capital letters written as A_{L1L2L3} with L1: *initial core hole location*; L2: *initial location of relaxing electron*; and L3: *location of second hole (initial location of Auger electron)*
  For example: C_{KLL} for an Auger electron emitted from the L level of a carbon atom and created from the relaxation of the excited atom by an electron from the L level to fill a hole in the K level as illustrated in Fig. 2.25 (a).

- *For XPS,* photoelectron peaks are labelled by electron orbitals as $1s$, $2s$, $2p$, etc. For example: C $1s$ designates a peak due to emission of electrons from the $1s$ level of carbon atoms (Fig. 2.25 (b)).

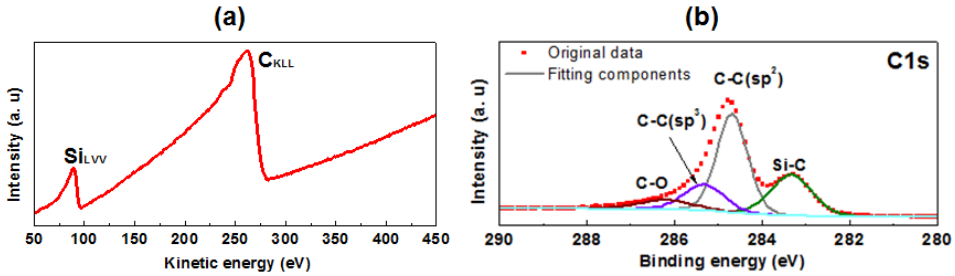

Fig. 2.25: (a) AES and (b) XPS C $1s$ core level spectra of graphene on Si(111).

AES analyses for our samples were performed *in situ* using an Auger spectrometer (CMA 100/150) from Omicron NanoTechnology GmbH and XPS measurements were made with a K-Alpha spectrometer from Thermo Scientific with a monochromatic Al Kα X-ray source (E_{photon} = 1486.6 eV) and a resolution of 0.1 eV (see next chapter).

b. Depth profiling of AES and XPS

Fig. 2.26 illustrates an Auger electron or a photoelectron emitted from a depth d in the sample.

At a given kinetic energy, a parallel beam with the intensity I_0 of electrons travelling through a solid material of thickness d is attenuated according to Beer-Lambert law. So,

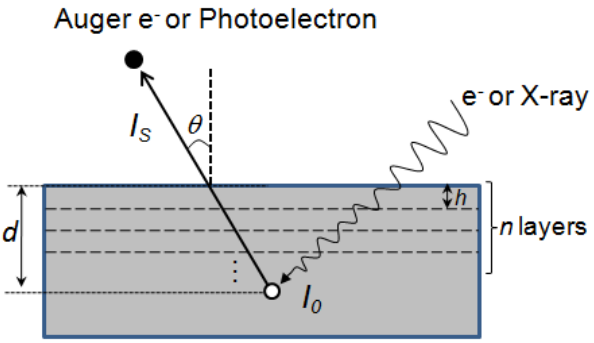

Fig. 2.26: The schematic diagram for determining the depth of AES and XPS processes

the intensity I_S of this electron reaching the surface is

$$I_s = I_0 e^{-\frac{d}{\lambda \cos\theta}} \tag{2.46}$$

where λ is inelastic mean free path of an electron in a solid; θ is the angle between direction of the beam and surface normal.

Assuming negligible attenuation of the incoming beam, the total Auger or photoelectron intensity can be written as a geometric series for a system of n epitaxial layers of equal composition.

$$I_S = I_0 \left(1 + e^{\frac{-h}{\lambda \cos\theta}} + ... + e^{\frac{-(n-1)h}{\lambda \cos\theta}}\right) = I_0 \sum_{i=0}^{n-1} e^{\frac{-ih}{\lambda \cos\theta}} = I_0 \frac{1 - e^{\frac{-nh}{\lambda \cos\theta}}}{1 - e^{\frac{-h}{\lambda \cos\theta}}}, \tag{2.47}$$

By measuring the intensity of photoelectrons, Eq. (2.46) can be solved for the depth or Eq. (2.47) for the number n of epitaxial layers if I_0, I_s and λ are known.

2.5.4. Raman spectroscopy (RS)

a. Principle of Raman

Raman effect can be described as inelastic scattering of light (usually a laser). The interaction of an incoming photon with a solid excites molecules/atoms to a - 'virtual' - energy state. Upon relaxation to a lower state, a photon can be emitted (Fig. 2.27 (a)).

- Much of the light is scattered elastically, meaning that the scattered photon has

the same wavelength (or energy) as the incoming photon. This is often referred to as Rayleigh scattering.

- A small fraction of the incoming photons are scattered at a wavelength which is shifted from the original one, meaning that the photons have lost or gained energy (longer or shorter wavelength) through the (de-)excitation of lattice vibrations (phonons) or molecular vibrations. If the scattered photon has less energy than the incident photon ($\lambda_s > \lambda_i$), the process is called Stokes scattering and vice versa, it is callled anti-Stokes ($\lambda_s < \lambda_i$).

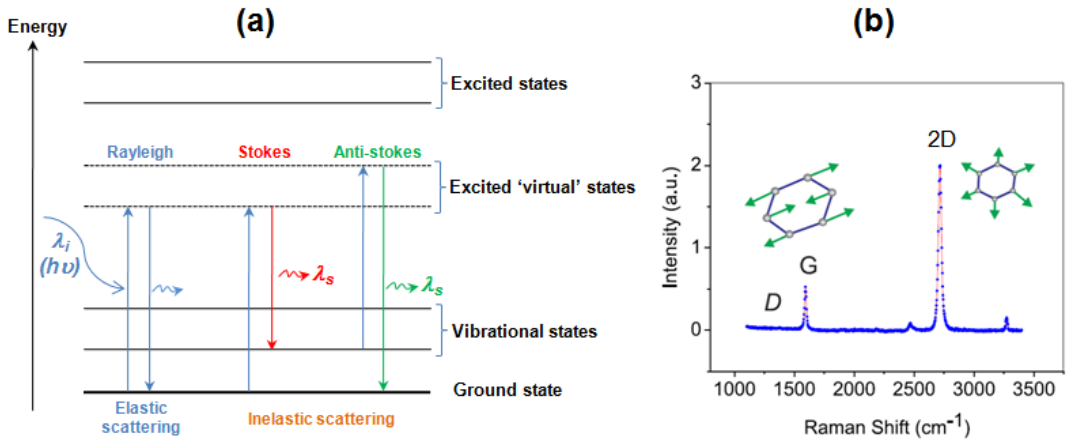

Fig. 2.27: (a) Model of Raman effect which is caused by inelastic light scattering (Stokes and anti-Stokes); (b) Various vibrational modes from carbon atoms in a typical graphene lattice of free-defects. Figure (b) adapted from Ref. [125].

The energy difference between the incoming and scattered photons causes a Raman shift which can be determined by the spacing between vibrational energy levels and the ground state. Therefore, the different vibrational modes can be identified by recognizing Raman shifts on the spectrum as illustrated in Fig. 2.27 (b).

In Raman spectroscopy, Raman shift is typically described in wavenumber $\tilde{\nu}$ (the number of wavelength per unit distance) which is related to the shift in wavelength between the incoming photon (λ_i) and the scattered photon (λ_s) according to the following formula [126]:

$$\Delta\tilde{\nu} = \tilde{\nu}_i - \tilde{\nu}_s = \frac{1}{\lambda_i} - \frac{1}{\lambda_s} \tag{2.48}$$

where $\Delta\tilde{\nu}$ is the Raman shift (cm^{-1}).

b. Raman for graphene

In recent years, Raman spectroscopy has become an important tool in the study of carbon based nanostructures, especially for graphene [127, 128]. Raman spectra of graphene are charaterized by three main bands labelled D, G and G':

- The D band ($\sim$ 1350 cm^{-1}) represents disorder or defects in the graphene lattice. If the crystallite size of graphene is smaller than the wavelength of light, the D band is often observed. This feature is due to the breathing of the carbon hexagons that becomes enhanced at the borders of the crystallite areas owing to the loss of translational symmetry [129]. Its intensity is proportional to the amount of disorder (crystallite boundary) in the sample. It is characteristic of scattering from K to K' (inter-valley phonon). As the amount of disorder in graphene increases, three another weak disorder peaks appear:
  - D' ($\sim$ 1620 cm^{-1}) is due to scattering from K to K (intra-valley phonon) which is given rise by single vacancy defects [130]. It is usually observed in the Raman spectra of disordered graphene with much smaller intensity than the D band.
  - D + G ($\sim$ 2940 cm^{-1}) and D' + G ($\sim$ 3250 cm^{-1}) are combination scattering peaks [129].

  If the graphene lattice is perfect, no D band is observed on Raman spectrum (Fig. 2.27 (b)).

- The G band ($\sim$ 1600 cm^{-1}) is associated with the in-plane vibration of the sp^2 bonded carbon in graphene due to the σ bond streching [127]. It is caused by one phonon intravalley scattering process at the Γ point. The presence of the G band indicates that the sample contains a system of sp^2 bonded carbon.

- The G' band ($\sim$ 2700 cm^{-1}) is the result of two-phonon resonance scattering process in the highest optical branch near the K point of the Brillouin zone [131]. It is more appropriately referred to as the second order overtone of the D band. So, it is also named as 2D band and is very sensitive to the stacking order of the graphene layers [128]. Therefore, it is also used for determining the number of graphene layers.

By using the ratio of peak intensities I_D/I_G, one can use Raman spectra to evaluate the degree of disorder in graphene. As disorder in graphene increases, the ratio I_D/I_G displays two different behaviors [128].

- **Regime 1** (low defect density): I_D/I_G will increase with the presence of a higher number of defects up to a regime of high defect density which is referred to as nanocrystalline graphite. The main effects in the evolution of the Raman spectrum as follows:
  - The D peak appears and I_D/I_G increases;
  - The D' peak appears at ~ 1620 cm^{-1};
  - All peaks broaden due to disorder.

  The ratio of I_D/I_G varies inversely with the crystallite size L_a according to the formula proposed by Tuinstra and Koenig as [132]

  $$\frac{I_D}{I_G} = \frac{C(\lambda)}{L_a}, \tag{2.49}$$

  where $C(\lambda) = \frac{560}{E_{laser}^4} = 2.4 \times 10^{-10}$ nm$^{-3} \cdot \lambda^4$ was fitted by Cançado et al. [133]; L_a, I_D and I_G are the crystallite size, the integrated peak areas of D and G peaks, respectively.

- **Regime 2** (high defect density): I_D/I_G begins to decrease due to the number of ordered carbon rings decreases which results in a more amorphous carbon structure, leading to the attenuation of all Raman peaks. The main effects in the evolution of the Raman spectrum in this stage occur as follows:
  - The G peak shifts from 1600 to ~ 1510 cm^{-1};
  - $I_D/I_G \propto L_a^2$;
  - $I_D/I_G \to 0$.

  For this case, a new relation is proposed according to the formula by Ferrari and Robertson as [127]

  $$\frac{I_D}{I_G} = 0.0055 L_a^2, \tag{2.50}$$

  where L_a, I_D and I_G are the crystallite size, the integrated peak areas of D and G peaks, respectively.

In this context, graphene is considered to be in the nanocrystalline graphite regime in which the mean crystallite size can be determined by

$$L_a(\text{nm}) = \left(2.4 \times 10^{-10}\right) \lambda_{laser}^4 \left(\frac{I_D}{I_G}\right)^{-1}, \tag{2.51}$$

where λ_{laser}, I_D and I_G are the excitation laser wavelength used in the Raman measurement (nm), the integrated peak areas of D and G peaks, respectively.

Raman data were obtained on our samples by using a LabRam HR system with a 514 nm laser excitation source and an objective of 100×. No outgassing was possible before performing the Raman measurements.

2.5.5. Scanning tunneling microscopy (STM) and atomic force microscopy (AFM)

a. STM principle

STM is a technique that allows for imaging electrically conducting surfaces at the atomic scale. It is explained in detail in the literature by quantum tunneling effect [134]. The general setup of a STM is illustrated in Fig. 2.28 (a).

A sharp tip is mounted on a piezoelectric tube with electrodes for controling the x, y, z positions. The tunneling tip is commonly made from W or Pt/Ir by electrochemical etching or mechanical cutting. After approaching the tip close to the sample surface, a tunneling current I_t flows between tip and sample as a bias voltage V_t is applied to the sample. This current can be used as the feedback signal in a Z-feedback loop. If the tunneling current exceeds its preset value, the distance between the tip and the sample is increased and vice versa, the feedback decreases the distance if the current falls below this value.

For a typical distance Z of a few angstroms, the electron transport will occur by tunneling as shown in Fig. 2.28 (b). The tunneling current is given by

$$I_t = I_0 \cdot e^{-2\cdot\kappa\cdot Z} = I_0 \cdot e^{-2\frac{\sqrt{2m\Phi}}{\hbar}Z} \tag{2.52}$$

where $I_0 \propto \rho V_t$ is a function of the applied voltage (V_t) and the density of states in both

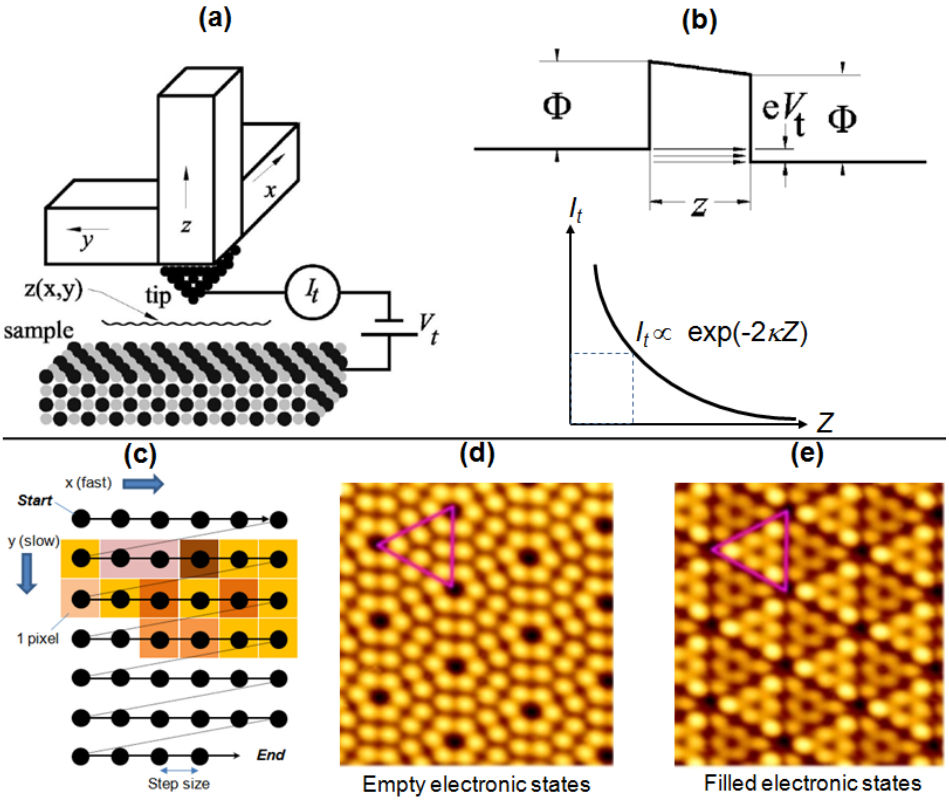

Fig. 2.28: (a) Schematic of atomically sharp tip and electronic connection; (b) The tunneling current I_t as a function of the distance Z between STM tip and sample surface; (c) A schematic of line by line scanning from top to bottom; Atomic resolution STM images of Si(111) 7×7 surface reconstruction with (d) empty (V_t=1.7 V) with 6 adatoms per triangle and (e) filled (V_t=-1.7 V) electronic states of the surface (with rest/adatoms of stacking fault appearing brighter in a solid purple triangle). Images (a) and (b) adapted from Ref. [135]; (d) and (e) adapted from Ref. [136].

tip and sample (ρ) [137]; e, m, Φ, and Z are electron charge, mass of electron, work function of the sample, and the tip - sample distance, respectively.

The tip is scanned line by line across the sample surface, following one of the two common modes of operation:

b. Mode of operation

- **Constant height mode:** Because the tip - sample distance is fixed, variation of I_t is displayed to form the image. Feedback is deactivated, so faster scan rates are

achievable. This mode is appropriate for flat surfaces.

- **Constant current mode:** Because I_t is kept constant during scanning, an electronic feedback circuit is required for moving the tip up and down. Therefore, only Z variation form the image. This mode scans more slowly but works for rough surfaces.

A computer converts each I_t or Z values to a color (or grey) scale which is plotted versus x, y positions to generate the image in pixel by pixel (Fig. 2.28 (c)). By changing the bias, the STM image can map out electronic structure of surfaces with atomic precision:

- When V_t is positive with respect to the tip, the image comes from empty electronic states on the surface (Fig. 2.28 (d)).
- When V_t is negative, the image corresponds to filled electronic states on the surface (Fig. 2.28 (e)).

The images were obtained in this study by using constant current mode at room temperature in UHV (VP2 from Park Instrument) at LPME - UNamur (Belgium). The tip is made of W wire (0.5 mm in diameter) prepared by electrochemical etching as described in Ref. [138]. The tip is degassed by flashing *in situ* a few times before use.

c. AFM principle

Unlike STM, AFM operates by measuring forces between a sharp tip which is attached to one end of a flexible cantilever and the sample surface at very short distances. Bending of the cantilever can be measured by reflecting a laser beam from the cantilever. Fig. 2.29 (a) is a schematic diagram of a typical AFM. The AFM tip has a very low spring constant and the detector (usually photodiode) is so sensitive that forces less than a nanoNewton can be detected to avoid damaging the surface and the tip [141]. The oscillation frequency of the cantilever depends on the tip-surface separation [142].

$$\omega(Z) = \omega_0 \sqrt{1 - \frac{1}{k}\frac{dF}{dZ}}, \tag{2.53}$$

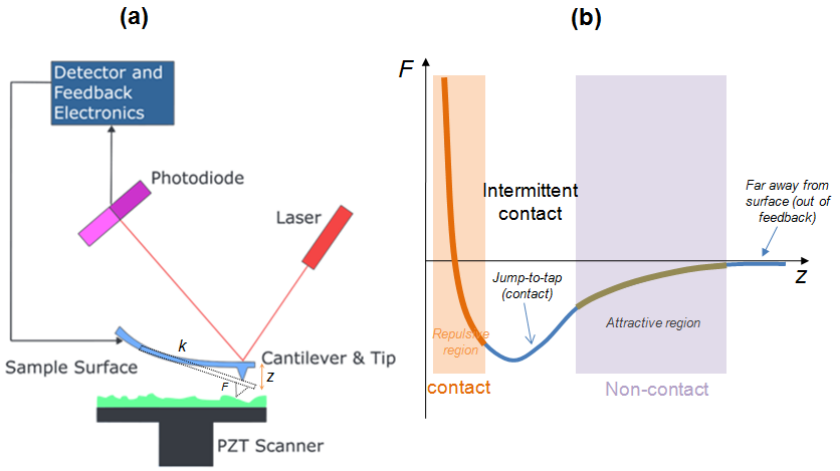

Fig. 2.29: (a) Schematic of AFM mechanism and (b) Force F as a function of tip-sample separation Z [139]. The image (a) adapted from Ref. [140].

with

$$\omega_0 = \sqrt{\frac{k}{m^*}},$$

where ω_0, k, m^* and Z are the resonant frequency, the cantilever spring constant, the effective mass (the mass of the cantilever + the mass of the tip), the distance between the sample surface and the mean position of the cantilever, respectively.

Therefore, there are three different modes of operation depending on the degree of contact between tip and sample surface (Fig. 2.29 (b)): [143]

d. Mode of operation

- **Contact mode** *(tip-surface separation:* < 5 Å):

  The AFM tip gently touches the sample surface and records the small force (repulsive) between the probe and the surface according to Hooke's law:

  $$F(\mathrm{N}) = -kx, \tag{2.54}$$

  where x is cantilever deflection.

  In this case, the electronic feedback circuit can adjust the tip height in order to maintain a constant force and deflection of the cantilever is displayed vs. (x,y).

- **Tapping (intermittent-contact) mode** *(tip-surface separation:* 5 - 20 Å):

  The cantilever is oscillated at or slightly below its resonant frequency. During scanning, the AFM tip lightly taps on the sample surface. This will slightly damp its oscillation. By maintaining constant amplitude, the distance between the tip and the surface can be measured.

- **Non-contact mode** *(tip-surface separation:* 20 - 100 Å):

  The AFM tip does not touch the surface and the cantilever oscillates at just above the resonant frequency. When the tip is closer to the surface, attractive van der Waals force will cause the resonant frequency and the oscillation amplitude to decrease. By using a feedback loop to adjust the probe height in order to maintain a constant amplitude of oscillation, the surface topography can be measured.

The main advantage of AFM is that it can be used for both insulating and conducting samples. In our work, AFM images were recorded in tapping mode with a Nanoscope III from Veeco Instruments (Santa Barbara, CA, USA). The probe (Tap300Al-G from Budget Sensors) composed of a silicon cantilever with the resonant frequency around 300 kHz and a typical spring constant of around 40 N/m, and an integrated silicon tip with a nominal apex radius of curvature lower than 10 nm. So-called soft-tapping conditions were used, i.e., the ratio between the set-point amplitude and the free amplitude of the cantilever vibration was always kept above 0.8.

2.6. Summary

According to the structure as proposed for growing graphene film on Si(111) substrate, the crystallographic properties of each of the relevant materials have been presented. The principle of electron beam evaporation is described as the physical vapor deposition from a solid source (graphite rod). Evaporation rate of the source is calculated by using different physical parameters as a function of heating power or vapor pressure. The main components needed to setup the experiment using graphite rod form, operating principle as well as experimental conditions for carbon evaporation are also provided in detail. Finally, a description of experimental techniques used to analyse the structural and electronic properties of our materials has been given.

Chapter 3

GROWING GRAPHENE ON Si: STATE OF THE ART

3.1. Introduction

There have recently been several attempts to grow graphene on Si wafer by using different methods. This chapter reviews the state of the art in growing graphene on Si wafers.

3.2. Electron beam evaporators

Hackley et al. [54] grew graphitic films on Si(111) 7×7 substrate by using an electron beam evaporator with a graphite rod as carbon source. The carbon films were grown at different substrate temperatures (560 °C, 600 °C, 660 °C, 700 °C and 830 °C) onto a B-doped Si wafer ($\rho = 24 - 30$ Ω·cm). Before carbon deposition, the substrate was covered by a thin buffer of approximately 20 nm of undoped-Si at 560 °C in order to provide a reproducible and smooth 7×7 surface reconstruction. Then, it is followed by few minutes of carbon growth ($\sim 10^{13}$ atoms/cm^2.s) at this temperature which is considered as a buffer before slowly heating the substrate to higher temperature. Changes in the property of carbon films during carbon depostion were monitored using RHEED (Fig. 3.1).

It reveals that carbon film grown at 560 °C is present as *a*-C because the RHEED pattern of Si(111) 7×7 surface washes out with the appearance of a very faint and broad diffraction ring. For the carbon growth at higher temperatures from 600 °C to 700 °C, a transformation from *a*-C to SiC occurs. The brightest diffraction streaks with low background, observed at 700 °C, indicate the improvement of the crystalline SiC structure.

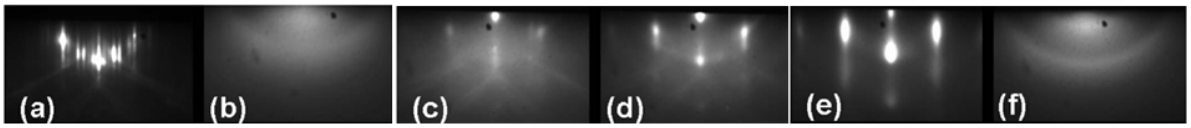

Fig. 3.1: RHEED patterns of pure Si(111) with a coverage of ∼ 20 nm of undoped-Si (a) and after carbon deposition at 560 °C (b), 600 °C (c), 660 °C (d), 700 °C (e) and 560 °C followed by annealing at 830 °C (f). Images adapted from Ref. [54].

Also, the intensity of Si-C peak at 282.6 eV on C 1s core level spectra increases gradually with increasing substrate temperature. It shows that above 700 °C the deposition of carbon leads to the formation of a SiC film instead of a graphitic film as shown in Fig. 3.2 (a).

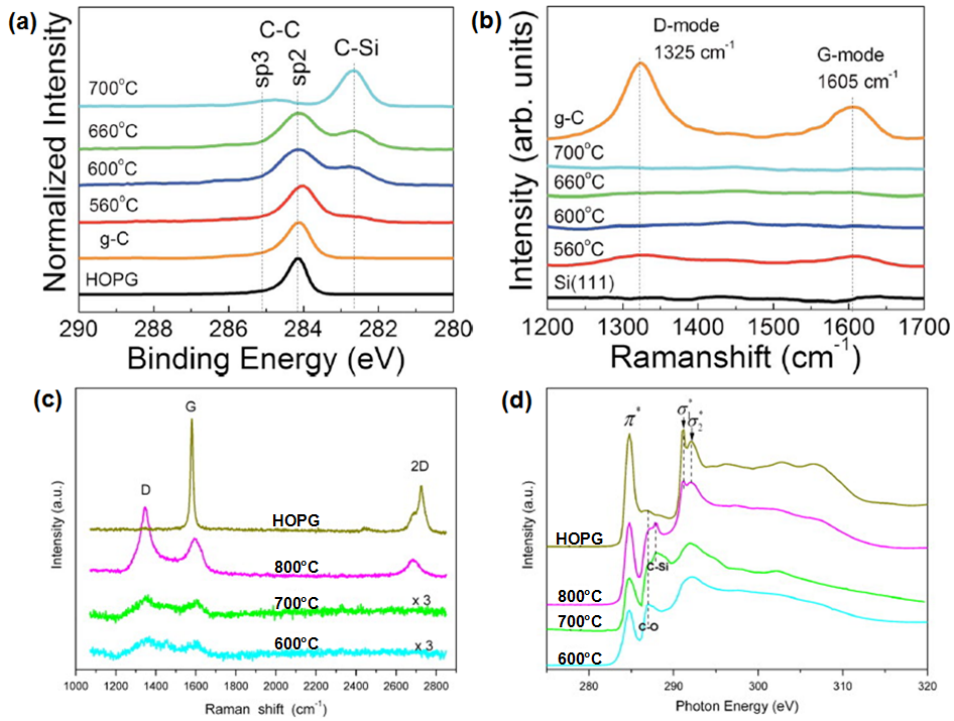

Fig. 3.2: (a) XPS spectra of C 1s core level and (b) Raman spectra (Source from Ref. [54]); (c) Raman spectra and (d) Near edge X-ray absorption fine structure (NEXAFS) at various sample temperatures (Source from Ref. [55]).

However, for an extended carbon growth as long as $\sim$ 60 minutes at 560 °C (thicker a-C layer) before annealing up to 830 °C during carbon deposition, it results in the sharp diffraction ring on RHEED image (Fig. 3.1 (f)) instead of SiC streaks, implying the growth of a graphitic polycrystalline film. This is consistent with the existence of the sp^2 peak at 284.1 eV on the C 1s XPS spectra, confirming the importance of growing a carbon buffer layer at low temperature prior to the formation of a graphitic film at higher temperature.

Tang et al. [55] and his co-workers reported their investigations on the formation of graphene on Si(111) but with different results. A Si buffer layer of $\sim$ 5 nm was first grown on Si(111) substrates at 800 °C for obtaining a smooth Si(111) 7×7 surface reconstruction before depositing carbon with a thickness of $\sim$ 3 nm (0.2 nm/min) at different substrate temperatures (600, 700 and 800 °C) (Figs. 3.2 (c, d)). Graphene films formed after a SiC layer is produced by Si-C interaction during carbon deposition on the substrate at 800 °C and a-C is found at lower temperature. Indeed, Raman measurements show the G and 2D bands at 1595 and 2687 cm^{-1}, respectively. Comparison with HOPG confirms the presence of sp^2 bonded carbon in the 800 °C sample while no graphitic carbon was found at lower temperature. Likewise, NEXAFS spectra of the 800 °C sample show an evidence of the σ bond at 291.2 eV and 292.1 eV in the same state as the one from HOPG while it is absent in other samples.

In both cases, one can see that the substrate temperature plays a key role for graphene formation. At lower substrate temperature, mobility of carbon atoms is insufficient to produce graphene. At higher temperature, carbon atoms react with Si to form SiC. This SiC could stabilize the substrate surface and prevent the reaction of C with Si atoms from the substrate. Graphitic carbon/graphene films deposited on top of SiC layers on Si(111) exhibit very poor crystallinity.

3.3. MBE growth

Among techniques known for graphene production on different substrates as mentioned earlier, SiC graphitization is able to produce large area epitaxial graphene layers directly on the substrate [144]. In this case, SiC wafer becomes a template for graphene growth during sublimation of Si atoms at very high temperature. Many different polytypes of

SiC such as $6H$-SiC, $4H$-SiC and $3C$-SiC have been used for this purpose [53, 145, 146]. However, the high cost of SiC substrate is a major obstacle for practical applications of graphene on SiC wafer. In order to overcome this problem, some groups have studied graphitization in UHV with the aim of growing graphene after first obtaining thick SiC films on Si substrate.

By forming a $\sim$ 100-nm-thick $3C$-SiC film on Si at 1000 °C by using a gas-source MBE method, Suemitsu et al. [62] obtained graphene layers by annealing up to $\sim$ 1230 °C in UHV. In order to evaluate the electronic properties of graphene produced with this method, different crystallographic orientations of the Si wafer such as (111), (100) and (110) were studied. The crystalline quality of the $3C$-SiC film can be controlled by adjusting the growth temperature at an appropriate working pressure as shown in a T-P diagram (Fig. 3.3):

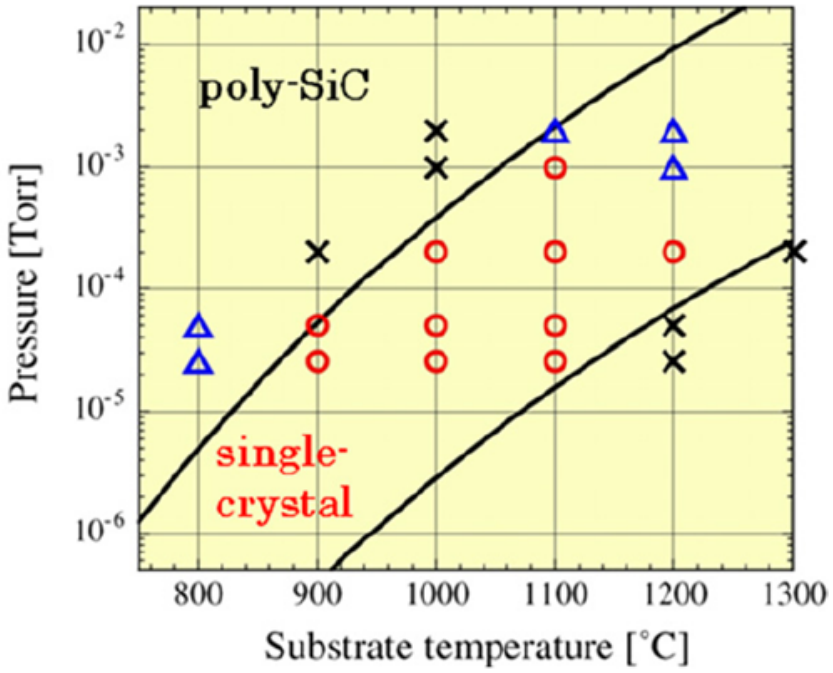

Fig. 3.3: Crystallinity of the $3C$-SiC film grown on Si(100) substrate in the T-P diagram where the circles, triangles and crosses denote single-crystalline, poly-crystalline and amorphous films, respectively. Image adapted from Ref. [62].

According to their structural analyses, $3C$-SiC/Si(111) has a similar property to $6H$-

SiC(0001) [5] in forming the graphene layers because its top four layers are stacked as ABCA [6]. This explains the reason why $3C$-SiC/Si(111) surface is used for graphene formation. Raman measurements were recorded on $3C$-SiC/Si(111) (bottom), $3C$-SiC/Si(100) (middle) and $3C$-SiC/Si(110) (top) after $\sim$ 30 min of graphitization as shown in Fig. 3.4 (a).

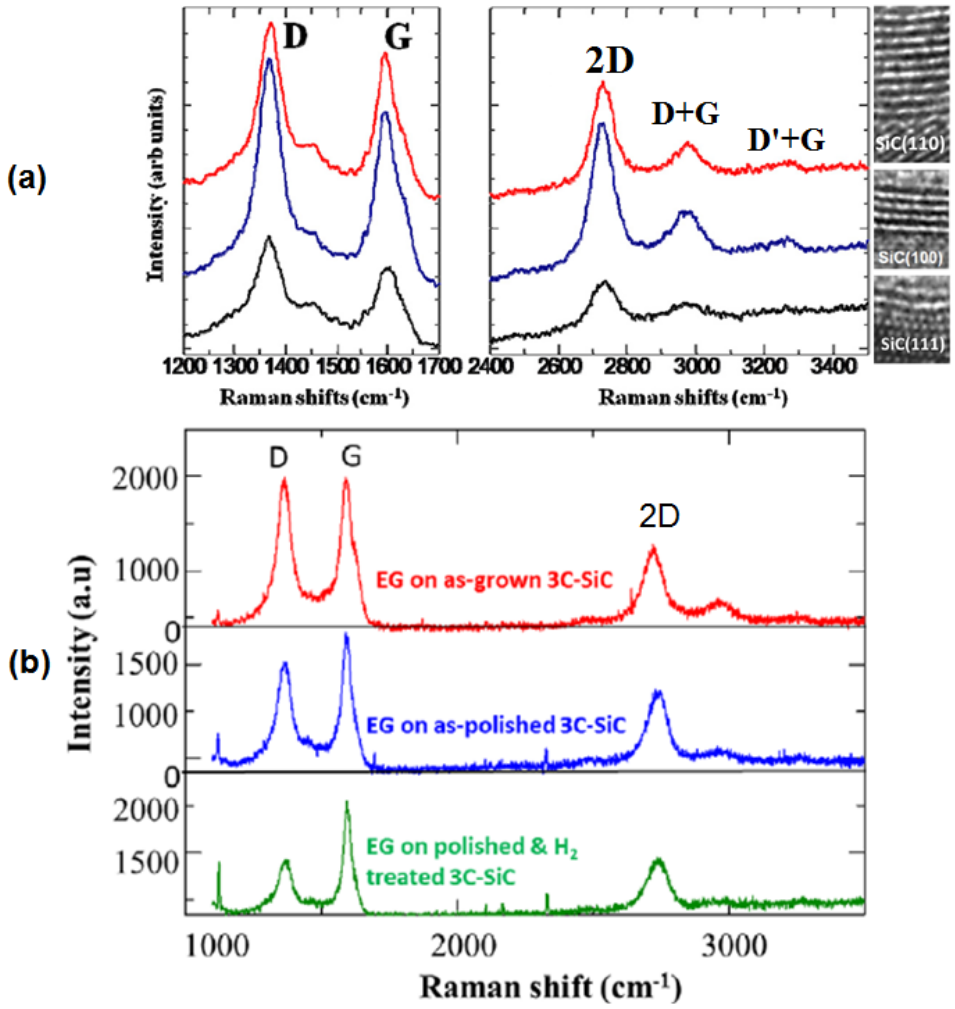

Fig. 3.4: (a) Comparison of the Raman spectra of epitaxial graphene on $3C$-SiC/Si(111) (bottom), $3C$-SiC/Si(100) (middle) and $3C$-SiC/Si(110) (top) together with corresponding TEM images of graphene layers. Image adapted from Ref. [62]; (b) Raman spectra of graphene formed on $3C$-SiC/AlN/Si(111) with and without surface treatments. Image adapted from Ref. [75].

[5] Surface orientation of (0001) hexagonal structure.
[6] $3C$-SiC/Si(111) wafer is expected to graphitize as $6H$-SiC wafer.

One can see that G ($\sim$ 1590 cm^{-1}) and 2D ($\sim$ 2720 cm^{-1}) bands are clearly visible, indicating that epitaxial graphene was grown on three major low-index [7] orientations of 3C-SiC films despite of their different surface symmetries. More interestingly, the epitaxial graphene on Si-terminated 3C-SiC/Si(111) has a Bernal stacking [8] with an interfacial buffer layer while the epitaxial graphene on C-terminated 3C-SiC/Si(110) and 3C-SiC/Si(100) shows a non-Bernal stacking without an interfacial buffer layer [62, 75, 76]. This results in the difference in the electronic properties of graphene on 3C-SiC/Si(111) compared to others [76]. The band structure of Bernal stacking graphene has semiconducting properties while non-Bernal stacking graphene is metallic [147]. However, growing high quality of graphene on Si wafers has still remained a challenge due to the large lattice mismatch ($\sim$ 20%) between Si and SiC. Therefore, a further study was performed by inserting an AlN (Aluminum Nitride) interlayer between Si and 3C-SiC layers which can reduce not only the lattice mismatch with SiC but also suppress the Si out-diffusion from the Si substrate during the graphitization [75]. Also, a CMP (chemomechanical polishing) was applied for SiC surface to reduce the surface roughness before annealing in an ambient containing H_2. As a result, the quality of graphene is higher with a D to G band intensity ratio as low as 0.4 [75] (Fig. 3.4 (b)).

Another study was also reported by Fukidome et al. [148] using the same MBE source in order to obtain $\sim$ 80 nm of 3C-SiC on p-Si(110) substrate (B-doped, 5 - 15 Ω·cm). Following SiC growth, the sample was annealed by resistive heating at 1200 °C to epitaxially graphitize the 3C-SiC surface. It shows that the domain size of graphene layers, calculated from the I_D/I_G ratio, strongly depends on annealing time as confirmed by Raman spectra in Fig. 3.5.

It is clear that longer growth time can improve the domain size, but increase the number of graphene layers.

Consequently, the graphitization of 3C-SiC layers on various Si wafers with different quality has been demonstrated. However, graphene films still present lower quality than exfoliated graphene [7] as well as epitaxial graphene on SiC single crystals [52]. This may be due to poor crystalline quality of the 3C-SiC film preformed on Si or AlN/Si wafers.

[7] The (100), (110) and (111) surfaces considered above are the so-called low index surfaces of a cubic crystal system (the 'low' refers to the Miller indices being small numbers: 0 or 1 in this case.

[8] A type of stacking order as in graphite in which atoms in the second layer sits over the center of the hexagon in the first layer.

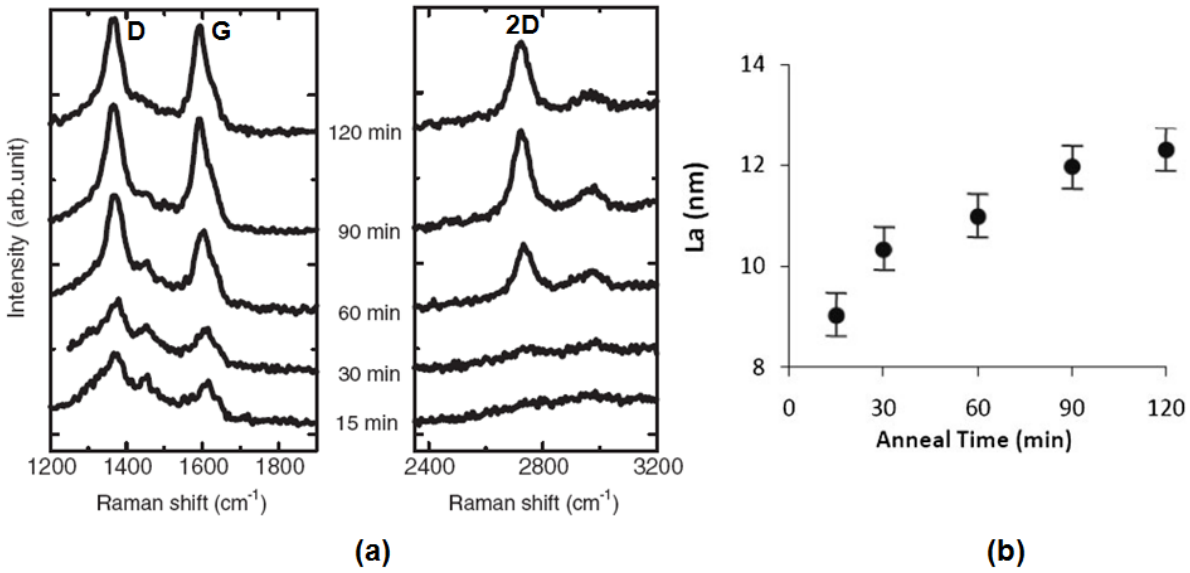

Fig. 3.5: Raman measurements: (a) Time evolution of epitaxial graphene, (b) The grain size (La) vs. the annealing time of graphitization. Images adapted from Ref. [148].

3.4. CVD growth

Gupta et al. [63] investigated thermal decomposition of $3C$-SiC films preformed on Si(111) substrates, instead of using a bulk SiC crystal for cost reduction and better integration of the material with Si-based electronic devices. After a $\sim$ 250 nm thick $3C$-SiC film was grown at 1000 °C on p-doped Si(111) wafer by using hot wall low-pressure CVD, the sample was transfered into the UHV chamber for annealing at 950 °C for a few minutes in order to compensate [9] the SiC surface from a silicon source (Si sublimation). It is reported that the number of graphene layers is very sensitive to the annealing temperatures. From XPS measurement, it was found that $\sim$ 0.4 to $\sim$ 7.8 graphene layers were formed depending on annealing temperature. Raman measurements confirmed the graphitic nature of the samples (Fig. 3.6).

[9]The Si flux in this case is used to compensate for Si loss during annealing.

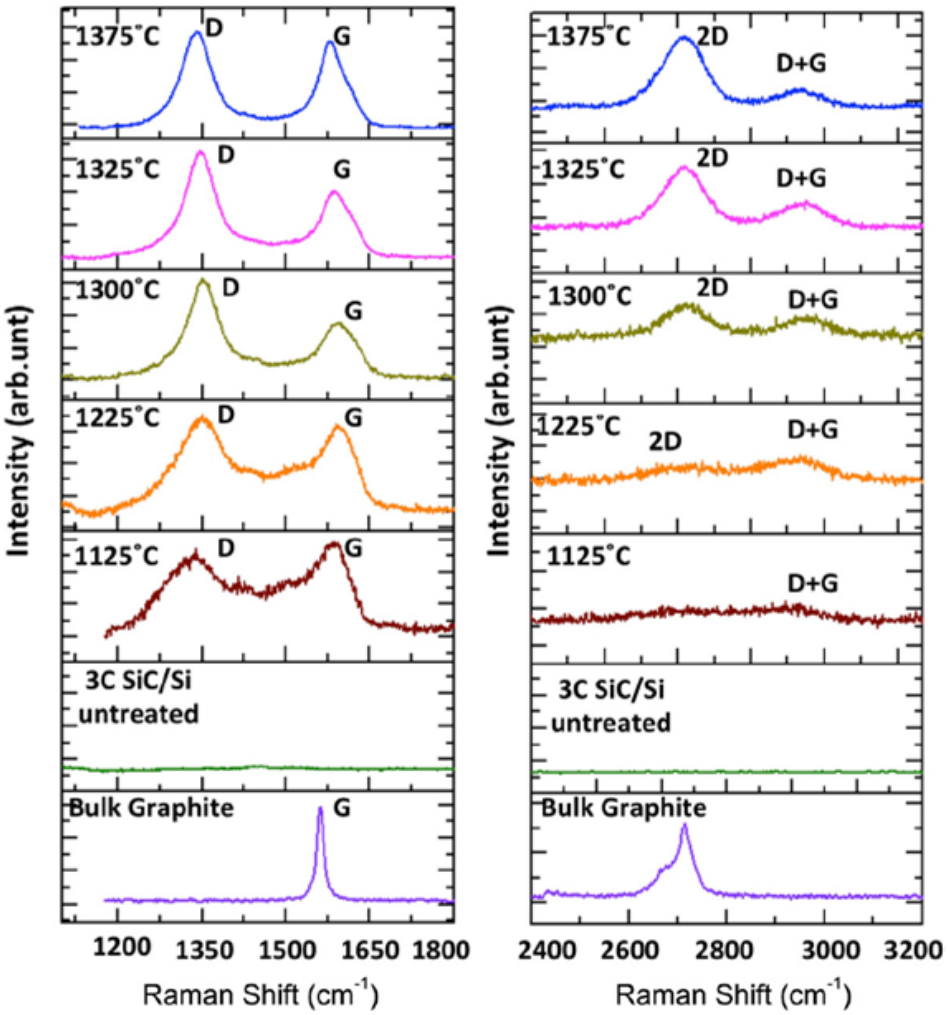

Fig. 3.6: Raman spectra of bulk graphite, untreated $3C$-SiC/Si (111) substrate, samples annealed at 1125, 1225, 1300, 1325 and 1375 °C (bottom-to-top) for 10 min. Figure adapted from Ref. [63].

The width of both G and 2D bands decreases with increasing annealing temperature, suggesting an improvement in crystalline structure. The crystallite size is estimated to be about 10 - 15 nm depending on annealing temperature by using the formula of Cançado et al. [133]. Although graphene obtained at the substrate temperature of 1375 °C is improved, it still presents a high number of defects with a broad D band which should be derived from structural disorder, vacancies, distortions and strain in graphene lattice [128, 149].

Further characterization was done by STM on the sample annealed at 1300 °C. Although the surface is rough with wrinkles, the atomic structure of graphene on $3C$-SiC/Si(111) was found. Fig. 3.7 (a) shows a STM image of 20×20 nm^2 with a Moiré pattern around the center of the image, revealing the presence of more than one graphene layer with Bernal stacking order (Figs. 3.7 (b, c)).

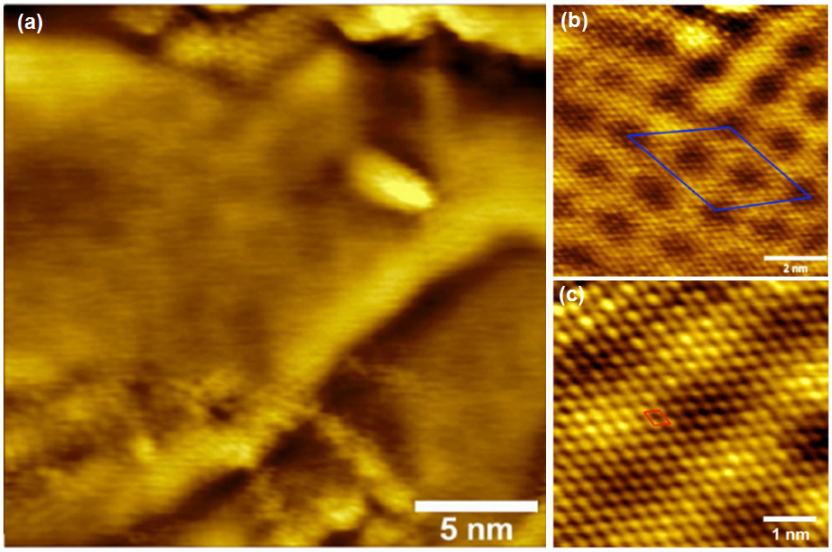

Fig. 3.7: STM images of graphene on $3C$-SiC/Si(111) after annealing at 1300 °C: (a) 20×20 nm^2 with wrinkles ($V_S = 70$ mV, $I_T = 0.3$ nA); (b) and (c) Moiré pattern with hexagonal symmetry ($V_S = 50$ mV, $I_T = 0.2$ nA). A blue insert is a $(6\sqrt{3} \times 6\sqrt{3})R30°$ unit cell. Images adapted from Ref. [63].

By using CVD growth, Cho et al. [150] reported a different way to grow graphene on various silicon wafers such as (100), (110) and (111) by heating the substrate in the environment of a carbon gas source. The carbon in the gas reacts with the silicon surface which results in the formation of SiC ($3C$-SiC). The substrate temperature was varied between 950 and 1200 °C. According to these authors, the growth of SiC layer is self-regulated due to the limitation of Si out-diffusion and carbon in-diffusion at a given temperature. Therefore, graphene starts forming on $3C$-SiC with carbon supplied from the gas phase.

Indeed, they showed by Fourier transform infrared spectroscopy (FT-IR) that no SiC was formed at 950 and 1000 °C, while it formed at higher temperature (Fig. 3.8). SiC

thickness was found to increase with annealing temperature.

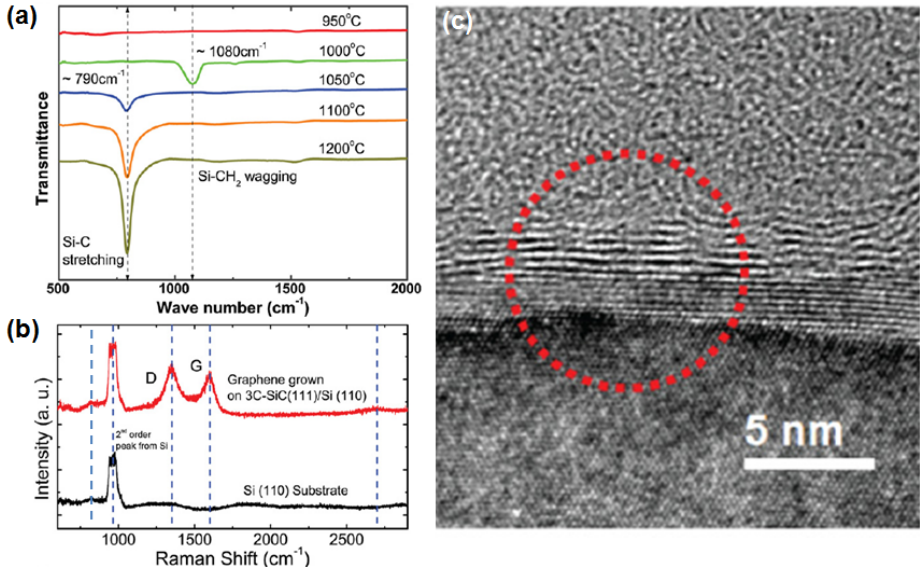

Fig. 3.8: (a) FT-IR spectra of the carburized Si(110) substrate at various annealing temperatures; (b) Raman spectra of $3C$-SiC/Si(110) before and after graphene formation at 1100 °C; (c) High-resolution TEM image of graphene/$3C$-SiC/Si(110) structure. Images adapted from Ref. [150].

For the 1100 °C sample, the peaks detected at $\sim$ 800 cm^{-1} and $\sim$ 970 cm^{-1} of Raman spectra are refered to transverse and longitudinal optical phonons (TO and LO) of $3C$-SiC layers together with the peaks at $\sim$ 1350 cm^{-1} and $\sim$ 1580 cm^{-1} which are identified as the D and G bands, respectively. This confirms the graphitic nature of the samples. High resolution tunneling electron microscope (TEM) confirms formation of graphene on top of SiC with a measurement of inter-layer distance $\sim$ 0.25 nm between SiC layers and $\sim$ 0.34 nm between graphene layers (Fig. 3.8 (c)).

Although epitaxial graphene on Si wafers is promising, it is always facing the challenge of Si out-diffusion. This is a well-known harmful factor that reduces the quality of epitaxial graphene grown on $3C$-SiC/Si. In order to solve this problem, many studies have been carried out by pre-growing a thick SiC film on Si substrate such as $\sim$ 600 nm [146], $\sim$ 1.5 μm [151] and from 0.7 to 2 μm [152]. However, the quality of epitaxial graphene on Si still remains mediocre. Therefore, some groups used catalysts as a buffer on Si wafer before graphitization.

Michon et al. [153] used AlN layers on n-type Si(111) as a template for direct growth of graphene. About 200 nm thick AlN films were obtained by MBE. Then, the sample is heated resistively at 1150, 1250 and 1350 °C in a hot wall CVD system with propane as the carbon source. As a result, $\sim$ 2 - 10 graphene layers were obtained on top of AlN/Si(111) while still preserving the morphology of the AlN layer beneath the graphitic layers. Raman measurements recorded as in Fig. 3.9 (a) with the characteristics of D, G, and 2D bands confirm graphene formation.

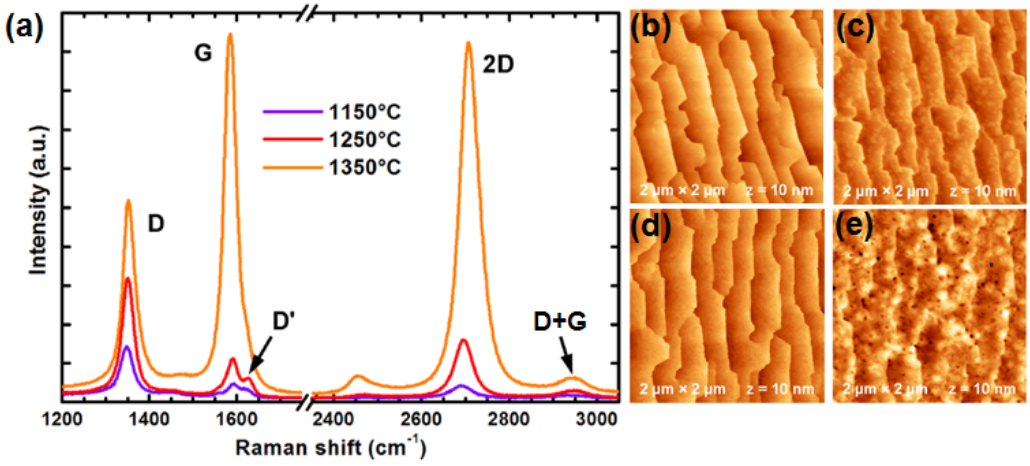

Fig. 3.9: (a) Raman spectra of AlN/Si(111) templates after graphene growth; (b) AFM images of AlN/Si(111) after annealing at 1150 °C; After graphene growth at 1150 °C (c), 1250 °C (d) and 1350 °C (e). Images adapted from Ref. [153].

The structural quality of graphene film is improved by increasing the substrate temperature, but limited at high temperature due to the crystalline quality of the AlN film. In fact, the crystal size is $\sim 5-6$ nm for the 1150 and 1250 °C samples ($I_D/I_G > 1$) while it is $\sim$ 30 nm in the 1350 °C sample ($I_D/I_G < 1$). However, the surface was observed with pits and hillocks as high as $\sim$ 6 nm at 1350 °C.

Instead of direct growth of graphene on Si, Lee et al. [65] grew $\sim$ 3 μm of a single crystal Ge film on Si(110) wafer by using a solid phase epitaxy [154]. The small difference in thermal expansion mismatch between Ge and graphene is expected to reduce wrinkle formation in graphene. As a result, a highly uniform monolayer graphene was synthesized on hydrogen-terminated Ge surfaces via low-pressure CVD at $\sim$ 900 °C (Fig. 3.10 (a)).

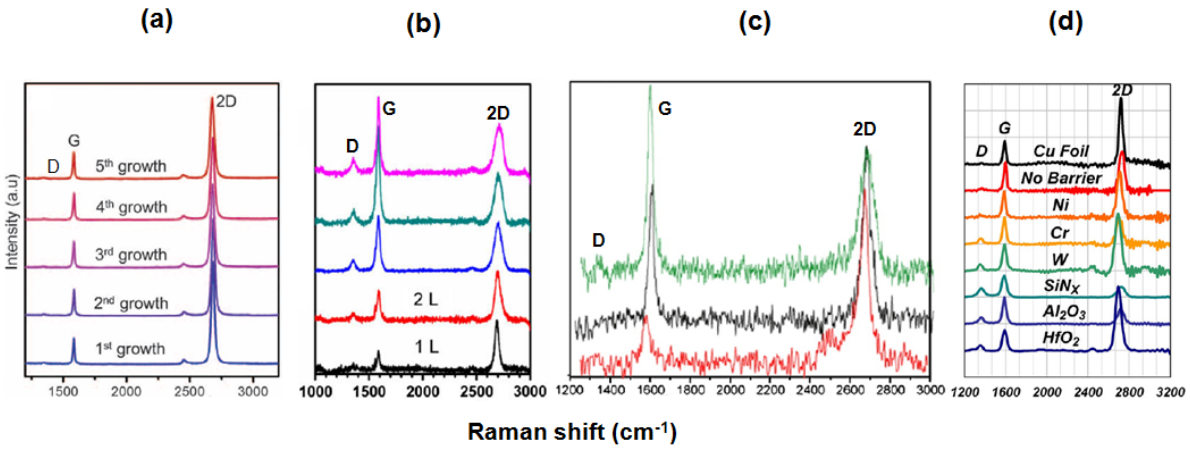

Fig. 3.10: Raman spectra of graphene on Si wafers by using various catalysts were reported by Lee et al. [65] (a), Park et al. [50] (b), Liu et al. [155] (c) and Howsare et al. [66] (d).

Similarly, several groups reported the use of an electron beam evaporator to grow a $\sim$ 300 nm [50] or $\sim$ 500 nm [155] thick nickel film on SiO_2/Si substrates, followed by CVD growth of graphene at $\sim$ 1000 °C. Howsare et al. [66] reported the growth of graphene on Si by using various configurations as Cu/metal(Ni, Cr, W)/SiO_2/Si or Cu/insulator (Si_3N_4, Al_2O_3, HfO_2)/Si.

Using catalysts as a solution to overcome the Si out-diffusion seems to lead to large area of transferable graphene with lower defect density (Fig. 3.10). However, the inter-diffusion between the catalyst and the substrate could introduce undesirable impurities as well as defects, wrinkles, and cracks which potentially degrade the performance of graphene-based devices.

3.5. Laser irradiation

Wei et al. [61] reported the use of a laser beam to melt a poly(methyl methacrylate) (PMMA)-coated Si(111) wafer as carbon source. Laser irradiation of 532 nm with a power of 3.1 W and a spot size of $\sim$ 20 μm causes the PMMA film to evaporate and decompose before melting the surface of silicon. The carbon atoms are then absorbed

and dissolved in melted silicon and a few graphene layers could be formed during the cooling process due to carbon extraction from the molten silicon. It is found that there is no graphene on the silicon surface if the laser power is below the melting point of silicon (< 1414 °C). A SEM image of a laser processed Si surface is shown in Figs. 3.11 (a) and (b).

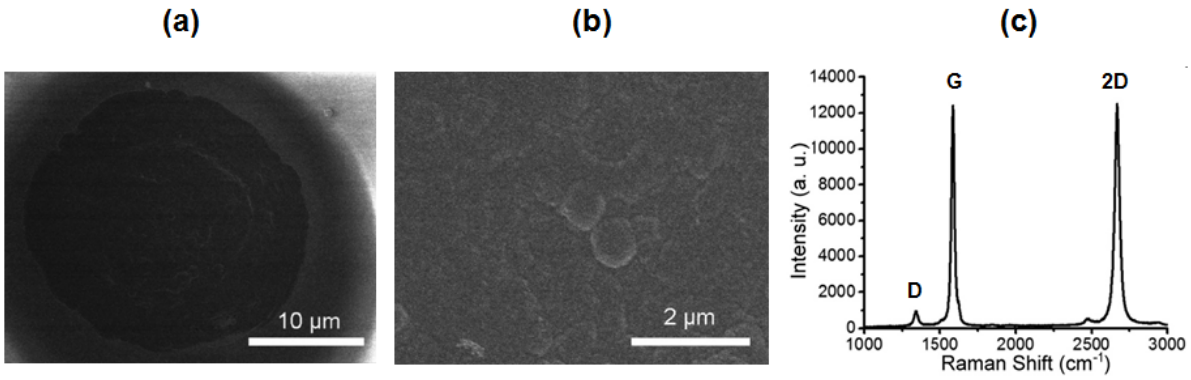

Fig. 3.11: (a) SEM image of laser processed Si surface and (b) a magnified SEM image of the center of the laser irradiated area; (c) Raman spectra recorded from the central area. Images adapted from Ref. [61].

Although the D, G and 2D bands were detected by Raman measurements in Fig. 3.11 (c) which is indicative of the formation of a few layers of graphene with low defects, the need for melting temperature to dissolve carbon in molten silicon is not desirable because it leads to inhomogeneous films and high surface roughness.

3.6. Transfer processes

Graphene transfer is a fast and simple process to obtain graphene directly on any substrates. Graphene used for this purpose is often prepared by CVD growth on copper foils [156] or by exfoliation of HOPG [7]. Some groups succeeded in transfering graphene on Si(111) wafers.

Ochedowski et al. [64] demonstrated that it is possible to exfoliate graphene flakes from HOPG on Si(111) 7×7 substrate using a stamping procedure by means of a wobble stick

in a UHV system at room temperature (Fig. 3.12 (a)). The advantage of this process is to avoid the physisorbed contaminations and to allow direct covalent bond formation with Si(111) 7×7 surface due to its specific reconstruction with unterminated bonds at the adatom positions via the attractive forces such as van der Waals or hydrogen bonds under ambient conditions. Although the flake size reaches several hundred nanometers, film adhesion is poor due to the huge lattice mismatch between graphene and the substrate. Indeed, Li et al. [157] indicated that adhesion energy of the relaxed interface decreases drastically with increasing the percentage of lattice mismatch. This could be a considerable drawback for further growth.

Another way to transfer graphene on Si wafer in ambient conditions was reported by Brus et al. [158]. They transfered graphene onto Si(111) after passivating with hydrogen (H_2) or methyl groups (CH_3). Following the process described in Fig. 3.12 (b), graphene is transferred on top of the passivated silicon surface from CVD grown graphene on copper foil [156].

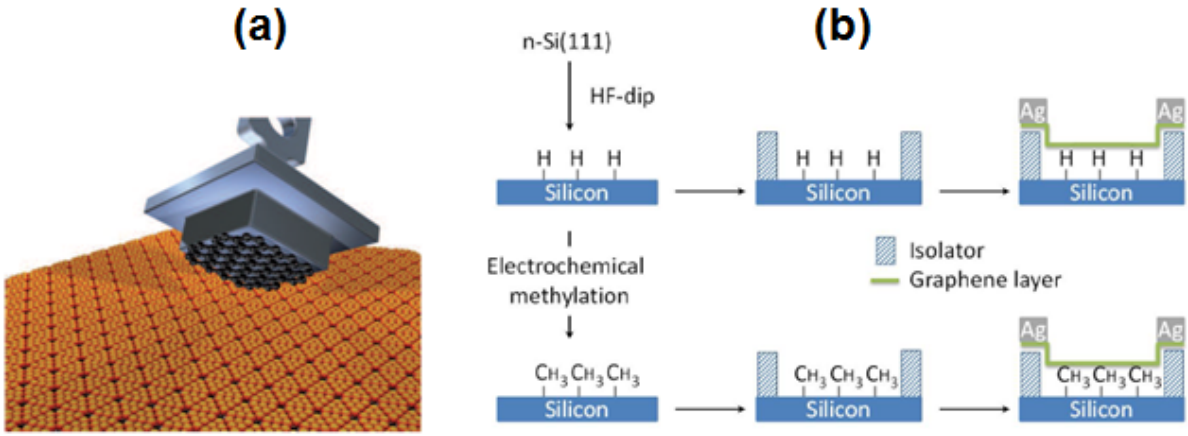

Fig. 3.12: (a) Direct exfoliation from HOPG on Si(111) 7×7 surface reconstruction by means of a wobble stick in UHV, adapted from Ref. [64] and the preparation steps of graphene on Si(111) heterojunctions with hydrogen and methyl termination of the silicon surface prior to the graphene transfer, adapted from Ref. [158].

3.7. Summary

From the above review, one can see that the production of defect-free graphene with low surface roughness and large area graphene on Si wafer is still a challenge. Direct formation of graphene using a buffer of *a*-C or SiC layer produces films of poor quality. Besides solutions using graphitization of SiC buffer layers on Si wafers at very high temperature, different catalysts were suggested for preventing the Si out-diffusion from the substrate in order to improve the crystalline quality of graphene films. However, the inter-diffusion between the catalysts and the substrate may introduce undesirable impurities as well as defects, wrinkles, and cracks that are not compatible with nano-scale integrated applications.

Chapter 4

EXPERIMENTAL RESULTS AND DISCUSSION

4.1. Introduction

This chapter focuses on the experimental process on how to prepare Si(111) 7×7 surfaces, followed by the growth of carbon layers at appropriate conditions using various recipes for obtaining graphene. A long story from graphitic carbon to graphene on Si(111) will be written with a continuous attempt in looking for graphene on silicon wafer after electron beam evaporation. In this context, several structural models were proposed for graphene formation on Si(111). In addition, a calculation of the silicon diffusion profile will be discussed in detail before the end of the chapter.

4.2. Preparation of Si(111) 7×7 substrate

n-type Si(111) ($\rho > 50$ Ω·cm) samples were used for this study. A pure silicon surface was obtained by *in situ* cleaning procedures in a UHV chamber with a base pressure of $\sim 10^{-10}$ mbar. The samples are characterized by LEED, AES and STM.

The sample (a single crystalline substrate of untreated Si(111)) is loaded in the UHV. Due to surface contamination (a native oxide layer and some organic/inorganic materials from air exposure), no LEED pattern is observed and the AES spectrum is shown in Fig. 4.1.

Besides the peak from oxidized silicon at ∼ 75 eV, O and C peaks are detected at kinetic energies of ∼ 500 eV and ∼ 260 eV confirming the presence of contaminants on the sample. Therefore, it needs to be cleaned before further steps.

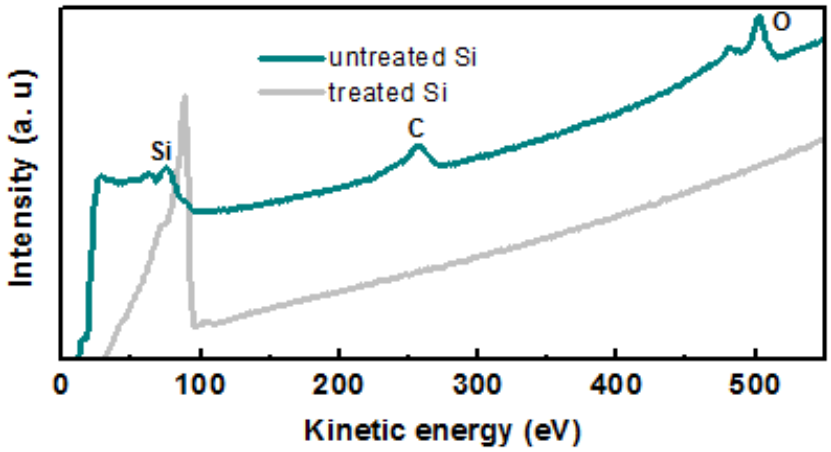

Fig. 4.1: AES spectra of untreated silicon (dark cyan) and after Ar^+ sputtering, followed by annealing up to $\sim$ 1050 °C (gray). Without Ar^+ sputtering, AES spectrum of clean Si surface shows similar results after annealing.

First, the sample is degassed around 450 °C for 12 hours by using direct heating current in the UHV chamber with a pressure below 1.0×10^{-9} mbar. In order to remove the contaminants, we tried with the two following ways:

- With Ar^+ sputtering [10]: The Si(111) surface is sputtered for 2 - 3 minutes by Ar^+ ions from an ion gun at 1 keV, followed by annealing up to 1050 °C. The pressure during sputtering was kept around 7.0×10^{-6} mbar with an ion current of about 30 - 40 μA (read by Keithley 4200).
- Without Ar^+ sputtering [11]: Direct annealing of the Si(111) surface up to 1050 °C.

During the procedure if the pressure rises above 5.0×10^{-9} mbar, the substrate temperature is reduced for a while. When the pressure is low enough, the heating process starts again until 1050 °C with a chamber pressure below 1.0×10^{-9} mbar. The sample is then cooled down to room temperature at 20 °C $\cdot$ min^{-1}.

The resulting AES spectrum is the gray curve in Fig. 4.1 while LEED pattern shows a very good surface of the Si(111) (7×7) reconstruction (Fig. 4.2 (a)). STM images confirm a cleaned surface at large scale and atomic resolution as shown in the inset of

[10] A few atomic layers of silicon surface as well as surface contamination will be removed by Ar^+ sputtering before annealing.

[11] Surface contamination is desorbed during annealing.

Fig. 4.2 (b) together with corresponding height profiles which show some steps (olive green) and the distance between two adjacent corner holes of the (7 × 7) surface (orange) (Fig. 4.2 (c)).

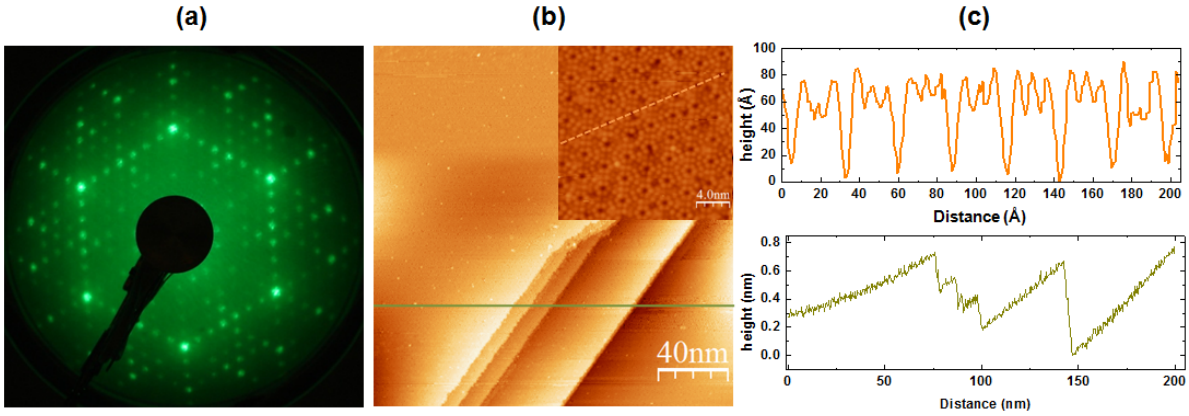

Fig. 4.2: (a) LEED pattern at 57 eV, (b) STM image of Si(111) surface on an area of 200 × 200 nm^2 ($V_S = +3$ V, $I_T = 0.25$ A) with an inset of atomic resolution (($V_S = +2$ V, $I_T = 0.2$ A)) and (c) height profile of corresponding STM images. The sample was prepared by Ar^+ sputtering before annealing. By doing this way, we often found steps after annealing.

4.3. Growing graphene on Si(111) 7×7 substrate

4.3.1. Experimental details

Carbon is deposited using an e-beam evaporator from Tectra GmbH with a graphite rod of 99.997% purity from Goodfellow Cambridge Ltd. Silicon is evaporated from resistively heated n-type silicon in the same chamber where carbon is deposited.

The samples are prepared *in situ* by evaporating carbon on the Si(111) surface. The substrate temperature is measured with an IR pyrometer (Raytek MM2MH (450 °C - 2250 °C) at the wavelength of 1.6 μm with the emissivity set at 0.65). The carbon deposition rate is measured by a quartz crystal oscillator. The pressure in the chamber is kept below 1.0×10^{-8} mbar during the evaporation.

The carbon deposition rate is held constant at $\sim 1.2 \times 10^{13}$ atoms/cm$^2 \cdot$ s until the carbon flux is shut off. For the case of using SiC as a buffer, the sample is exposed to carbon and silicon as shown schematically in Fig. 4.3. Following a method described by Liu et al. [159], the Si(111) surface is first covered by a $\sim$ 3 nm thick Si buffer at a substrate temperature of 800 °C from a silicon source in order to smooth the (7×7) surface. Next, the sample is exposed to carbon flux for 30 min (surface carbonization) at the same temperature. Then, it is slowly heated up to 1000 °C for co-deposition from Si and C flux in order to obtain a good crystallinity of $3C$-SiC film (the ratio between Si and C flux is approximately $\sim 1.5 : 1$).

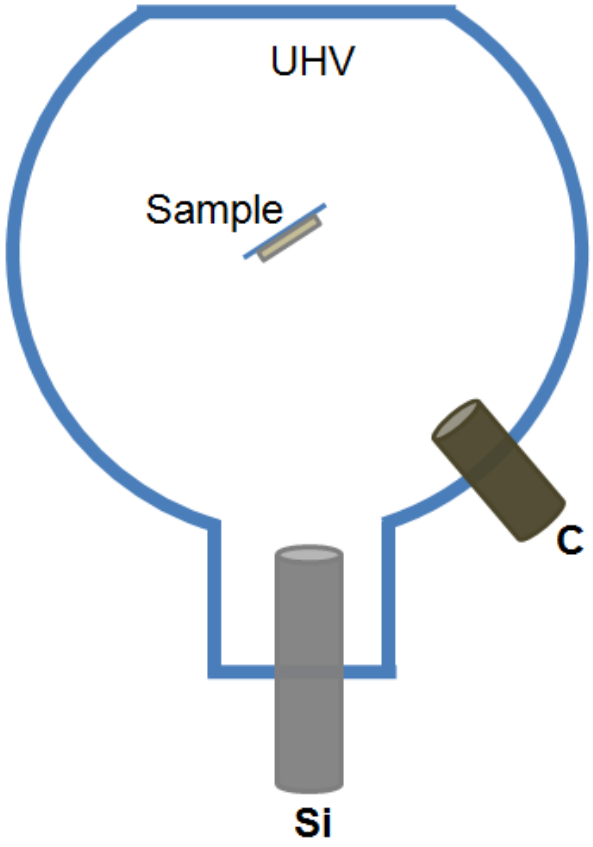

Fig. 4.3: Si and C sources in the UHV chamber.

Reflection high energy electron diffraction, Auger Electron Spectroscopy and STM analyses were performed *in situ* while Raman, XPS, HR-SEM and AFM were performed after transportation through air. After the *ex situ* measurements, the samples were re-introduced in the UHV chamber and AES measurements (after outgassing the samples

at $\sim$ 350 °C for 20 min) gave similar results to those reported below.

4.3.2. Proposed structural models for direct deposition of carbon layers

We found in the literature that graphitic carbon films form on Si(111) substrate via carbon buffers deposited first at low temperatures (it is called amorphous carbon (a-C)) before annealing to a high temperature during carbon deposition ($\sim$ 830 °C). However, the role of a-C layers has not been fully understood yet. We therefore investigated the influence of carbon buffer thickness on the formation of graphitic carbon films on Si(111) substrate.

a. Model 1: C/*a*-C/Si(111)

This part is adapted from ***Trung et al., Applied Physics Letters 102, 013118 (2013)***.

The procedure for obtaining graphene formation on Si(111) using a carbon buffer layer deposited at room temperature is shown in Fig. 4.4.

First, the samples are covered by a carbon layer with varying thickness at room temperature; this layer is called the buffer layer. Then, the substrate temperature is gradually increased (in about 4 min) to 820 °C and is maintained at this temperature for five minutes. The carbon flux is then shut off and the sample is cooled down to 200 °C at 20 °C $\cdot$ min^{-1}, and then free-cooled to room temperature. Four different samples (#1, #2, #3 and #4) with different buffer layer thicknesses ($\sim 3.5 \times 10^{15}$ atoms/cm^2 (1 ML), $\sim 5.2 \times 10^{15}$ atoms/cm^2 (1.5 ML), $\sim 1.1 \times 10^{16}$ atoms/cm^2 (3 ML) and $\sim 1.4 \times 10^{16}$ atoms/cm^2 (4 ML), respectively) were analyzed. The SiC and HOPG crystals used as references were analyzed in the same UHV system after outgassing at $\sim$ 600 °C for several hours (except for the XPS and Raman measurements). An oxide layer is still present on the SiC after such outgassing [160] while the HOPG showed no oxygen contamination.

Figs. 4.5 (a) and (b) display the Auger spectra and their derivatives around the C_{KLL} transition and compare them to the spectra of SiC and HOPG.

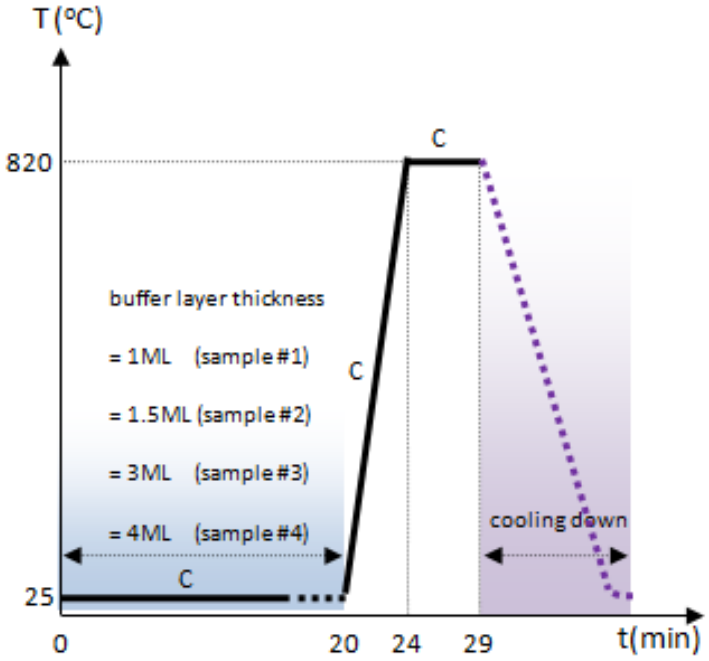

Fig. 4.4: A growth process for graphene formation on Si(111) 7×7 substrate where C stands for carbon source ON. The Si(111) substrates were cleaned by Ar^+ sputtering, followed by annealing up to ∼ 1050 °C as mentioned in section 4.2.

Clearly, one can see in Fig. 4.5 (a) that the shape of the curve of sample #1 is similar to the one from the carbide while samples #2, #3 and #4 are similar to the graphitic carbon signal (HOPG). The difference between the spectra appears more clearly on the differentiated spectra (Fig. 4.5 (b)). The energy difference D between the maximum and the minimum of the curve (illustrated in Fig. 4.5 (b) for the HOPG spectrum) is given in Table 4.1. These differences can be used to determine the ratio of sp^2-bonded

SiC	#1	#2	#3	#4	HOPG
11.0	11.0	22.0	22.6	22.6	22.7

Table 4.1: Values of D (cf. Fig. 4.5 (b) for the four samples, SiC and HOPG (in eV)

carbon to sp^3-bonded carbon in carbon compounds [89, 90]. We can conclude from those values that carbon atoms in sample #1 are in the same state as in silicon carbide (sp^3 hybridization) while those in samples #2, #3 and #4 are sp^2-bonded to other carbon atoms, as in HOPG.

SiC formation on sample #1 is confirmed by its LEED pattern displayed in Fig. 4.5 (c).

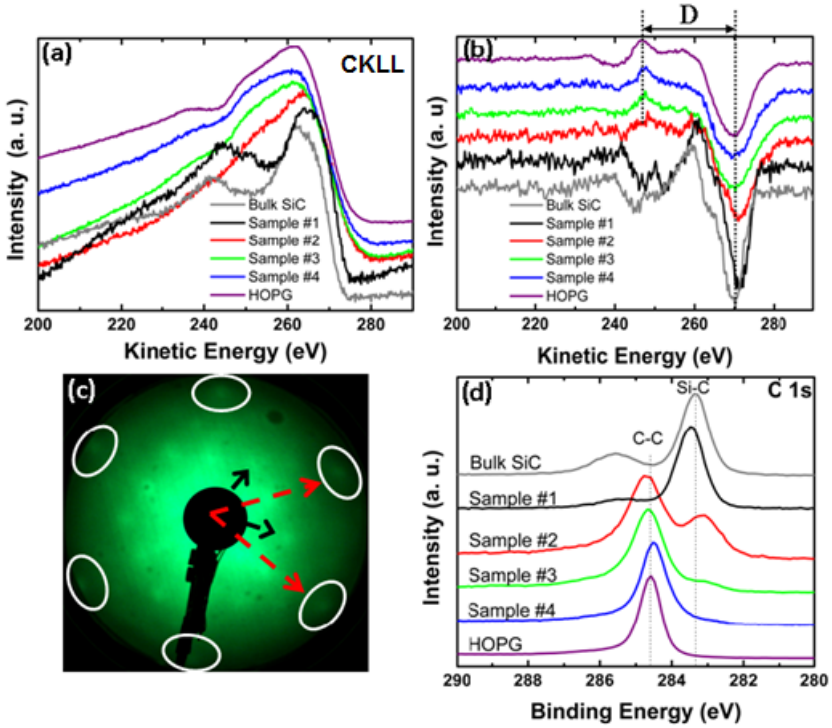

Fig. 4.5: (a) AES spectra around the C_{KLL} transition of the four samples as well as HOPG and SiC; (b) The differentiated spectra; (c) C 1s XPS spectra of samples #1 to #4 (and HOPG and SiC as references); (d) LEED pattern at 50.2 eV of sample #1 showing spots corresponding to the SiC formation (lattice constant of ~ 3.1 Å).

There are six main diffraction spots (marked by circles and highlighted by red arrows) corresponding to a lattice constant of 3.1 Å. This is consistent with 3C-SiC(111) which is the SiC polytype expected to grow on Si(111) at these temperatures [161].

The black arrows point out diffraction spots that, although not well-resolved, could correspond to the $\sqrt{3} \times \sqrt{3}$ reconstruction which has been observed for this surface [62, 146].

The graphitic nature of the carbon film on samples #2, #3 and #4 and the carbide nature of the film on sample #1 are further confirmed by XPS data on C 1s core level shown in Fig. 4.5 (d). The spectrum of sample #1 is very similar to the SiC spectrum (except for the component at 285.5 eV which corresponds to the native oxide found on SiC [160]). The main peak of sample #2 appears at 284.7 eV, corresponding to C-C bonding, while a weaker component corresponding to the SiC formation is seen at 283.2 eV. The spectrum of sample #4 is practically identical to the one of HOPG, indicating

a graphitic nature for the carbon film on this sample.

Raman measurements were performed in the 1200 - 2800 cm^{-1} range to investigate the vibrations related to C-C bonds in the samples. The spectra recorded are plotted in Fig. 4.6, where baselines have been substracted. Lorentzian fittings have been carried out in order to analyze quantitatively the data. I_D/I_G ratios of the integrated areas have been calculated as well as the related crystallite sizes (L_a) according to the equation (2.50) (supposing a regime in which our materials evolve from amorphous carbon to nanocrystalline graphite). A careful inspection of the data reveals that sample #1 does not show the typical sp^2 related signatures of C-C bonds, however a strong signal at $\sim$ 1450 cm^{-1} appears (marked by *). Such feature has been observed previously in amorphous SiC systems, showing its depletion as graphitization occurs in the systems [162, 163]. This tendency is confirmed in our samples, as will be discussed below: graphitic bonds are present in the rest of the samples, accordingly, the intensities of the features at 1450 cm^{-1} are less important (gray curves in Fig. 4.6).

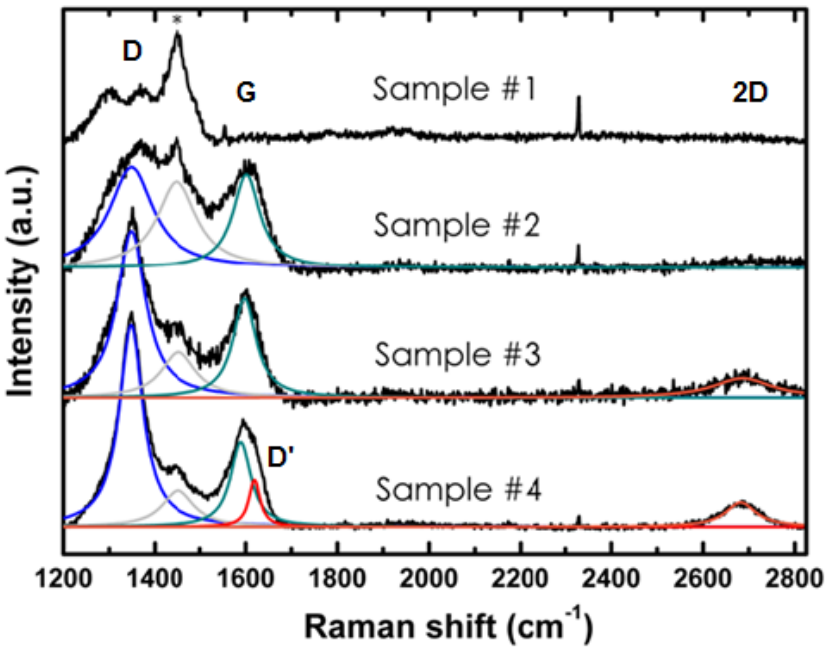

Fig. 4.6: Raman measurements of the studied samples, the different spectra have been vertically shifted to better illustrate the differences. The different peaks appearing in the spectra of samples #2, #3 and #4 have been fitted to single Lorentzians.

The G band (at 1600 cm^{-1}, green fitted bands in Fig. 4.6) is present in samples #2, #3 and #4 confirming the presence of graphitic bonds, in good agreement with our AES characterization. The disorder-related features are also present in these samples (D bands at 1350 cm^{-1}, blue fitted bands and D' band at 1620 cm^{-1}, red fitted band). Analysis of the I_D/I_G ratios of our materials shows an increase in crystallite size: for sample #2, $L_a = 17$ Å; for sample #3, $L_a = 19$ Å and for sample #4, $L_a = 22$ Å. For samples #3 and #4, the 2D band appears (orange fitted bands in Fig. 4.6), suggesting a higher degree of stacking order when compared with sample #2. Overall, the depletion of the 1450 cm^{-1} feature and the presence of sp^2 related features (D, G and 2D bands) in our samples confirm the success in growing graphitic films on silicon substrate.

From the above analysis, we conclude that in order to grow graphitic carbon on Si(111) the minimum thickness of the buffer layer is about 3 ML (sample #2 marks the transition between SiC and graphitic carbon; sample #3 being considered as graphitic).

STM imaging strongly supports the previous conclusions. Fig. 4.7 (a) shows a large scale image of the sample #4. The steps of the Si(111) substrate are still clearly resolved but the root mean square roughness of the surface ($\sim$ 1.2 Å; between the substrate steps) is much higher than the one of the bare Si(111)7×7 ($\sim$ 0.3 Å). Despite this roughness, we managed to achieve atomic resolution on samples #2, #3 and #4 as shown in Figs. 4.7 (b), (c) and (d), respectively. Although the resolution on the images of samples #2 and #3 is not good, a triangular lattice is still visible. Height profile analysis reveals that the lattice constant is indeed $\sim$ 2.5 Å, as expected for graphitic surfaces. Those images present the triangular symmetry corresponding to the Bernal (ABA) stacking of the carbon layers [164]. However, the image of sample #4 (d) displays the honeycomb lattice of free-standing graphene. This can be explained by a rotational mismatch between the layer being scanned and the one underneath, restoring the symmetry between the two carbon atoms of the graphene unit cell [164]. The observation of both the triangular and the honeycomb structure is similar to what has been reported already for HOPG [165] and for epitaxial graphene on SiC(000$\bar{1}$) [53]. We must point out that the roughness of the surface as well as the small size of the crystallites (cf. Raman analysis) prevented us from reaching systematically the atomic resolution on the different samples.

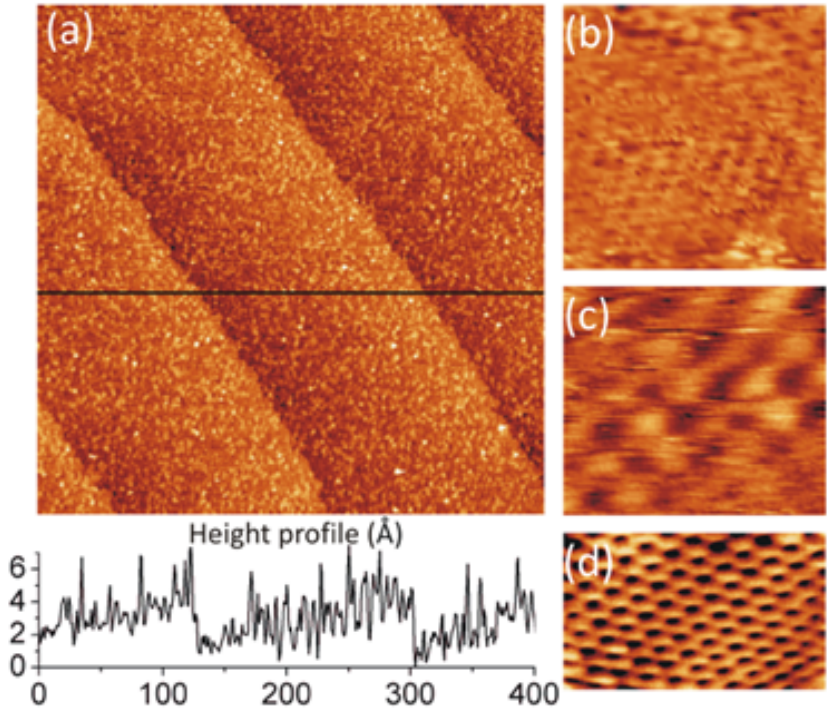

Fig. 4.7: STM images of samples #2, #3 and #4. a) Large scale (400×400 nm^2) image of sample #4 with a height profile ($V_{Sample} = +3$ V, $I_{Tunnel} = 0.35$ nA); b) 2.5×2.5 nm^2 image of sample #2 ($V_S = -1$ V, $I_T = 6$ nA; c) 1×1 nm^2 image of sample #3 ($V_S = -1.5$ V, $I_T = 4$ nA; d) 2.5×1.5 nm^2 image of sample #4 ($V_S = -1$ V, $I_T = 4$ nA) showing the honeycomb lattice of a graphene sheet.

In summary, we succeeded in growing graphitic layers directly on Si(111) through the deposition of a buffer layer of amorphous carbon at room temperature using electron beam evaporation (the minimum thickness of which is evaluated at 3 ML). In particular, we obtained real space (STM) images of such films. However, the need for an amorphous buffer layer induces a roughness on the substrate that we believe limits the size of the graphitic nanocrystals.

b. Model 2: C/*a*-C/3*C*-SiC/Si(111)

In addition, it is also known that the deposition of carbon atoms leads to the formation

of a SiC film instead of a graphitic film if the annealing is higher than 700 °C due to Si out-diffusion from the substrate and intermixing with the deposited carbon [54]. In order to improve the film quality on Si(111), the challenge is to prevent the Si-C bonds during graphitic carbon formation. Therefore, we produced a few SiC layers first on Si(111) which is considered as a crucial barrier to suppress silicon out-diffusion from the substrate. Following several carbon buffer layers deposited at room temperature ($\sim 1.4 \times 10^{16}$ atoms/cm^2 ($\sim$ 4 ML)), the sample is slowly heated up to 1000 °C. We found graphene with different qualities depending on the time of carbon deposition.

The growth process is described in Fig. 4.8.

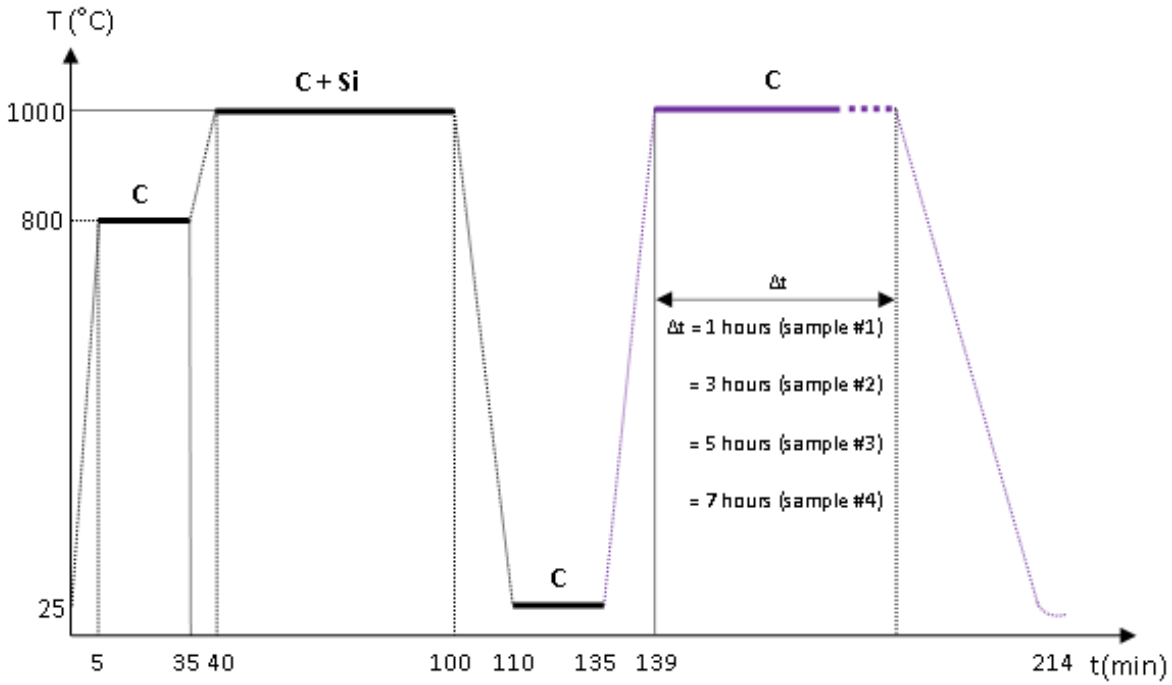

Fig. 4.8: A growth process for graphene formation on Si(111) 7×7 substrate where Si and C stand for silicon and carbon sources ON, respectively. The Si(111) substrates were cleaned by direct annealing up to $\sim$ 1050 °C as mentioned in section 4.2.

After one hour for SiC formation under carbon and silicon flux, we stop the flux and gradually decrease the substrate temperature to room temperature for 20 min of carbon deposition. Carbon deposition is continued at 1000 °C for 1 hour (sample #1), 3 hours (sample #2), 5 hours (sample #3) and 7 hours (sample #4). The carbon flux is then

shut off and the sample is cooled down to 200 °C at 20 °C · min^{-1}, and then free-cooled to room temperature.

Fig. 4.9 shows the RHEED patterns of the samples after SiC growth and carbon deposition on top of SiC layers.

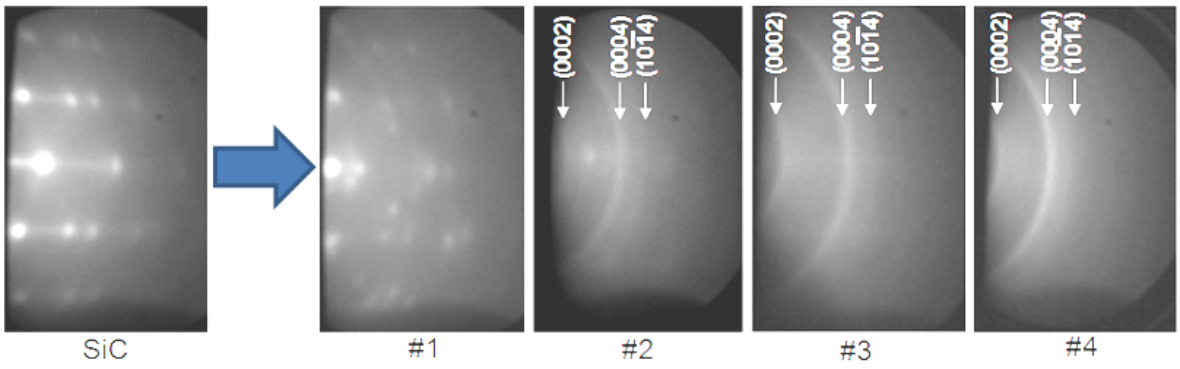

Fig. 4.9: RHEED patterns of the respective samples under various growth times on Si(111).

For one hour of carbon deposition, the SiC streaks become weaker, while very faint rings and some extra spots appear in the RHEED pattern (sample #1). This is probably caused by Si out-diffusing from the substrate and bonding with carbon at the surface. The diffraction rings appear more clearly in samples #2 and #3 together with very faint SiC streaks, meaning that carbide formation still occurs during carbon growth. If the deposition time is longer, the SiC streaks vanish and the rings become sharper in the pattern of sample #4. The sharp concentric rings are characteristic for polycrystalline graphitic material [54, 55]. These rings can be indexed as marked in Fig. 4.9.

By using the rings (0002) and (10$\bar{1}$4) in the sample #3, the lattice spacing can be found from equation (2.43) to be $d \simeq 3.39$ Å (close to the expected value of graphite: 3.35 Å (error ∼1.1%)).

The AES spectra and their derivatives around the C_{KLL} transition on our samples were recorded in Figs. 4.10 (a) and (b), respectively. Compared with the spectra of SiC and HOPG, it is clear that the curve shape of samples #2, #3 and #4 are similar to the one of HOPG while that of sample #1 is typical of silicon carbide. It is seen more clearly on the differentiated spectra (Fig. 4.10 (b)) with the energy difference D (∼ 22.6 eV

for samples #2 → #4 as in HOPG and ∼ 11 eV for sample #1 as in SiC) between the maximum and the minimum of the curve.

XPS data on C 1s core level confirms the properties of graphitic carbon in samples #2, #3 and #4 and carbide in sample #1 (Fig. 4.10 (c)). One can see that a transition from Si-C bonds to C-C bonds occurs gradually in time of carbon growth. In other words, the fraction of sp^2 bonded carbon depends on the time of carbon deposition. The main peak of sample #2 at 284.7 eV corresponds to C-C bonding which is practically identical to the one of HOPG and a weaker component at 283.3 eV corresponds to Si-C formation. It is consistent with the appearance of the faint SiC streaks in the RHEED pattern on this sample.

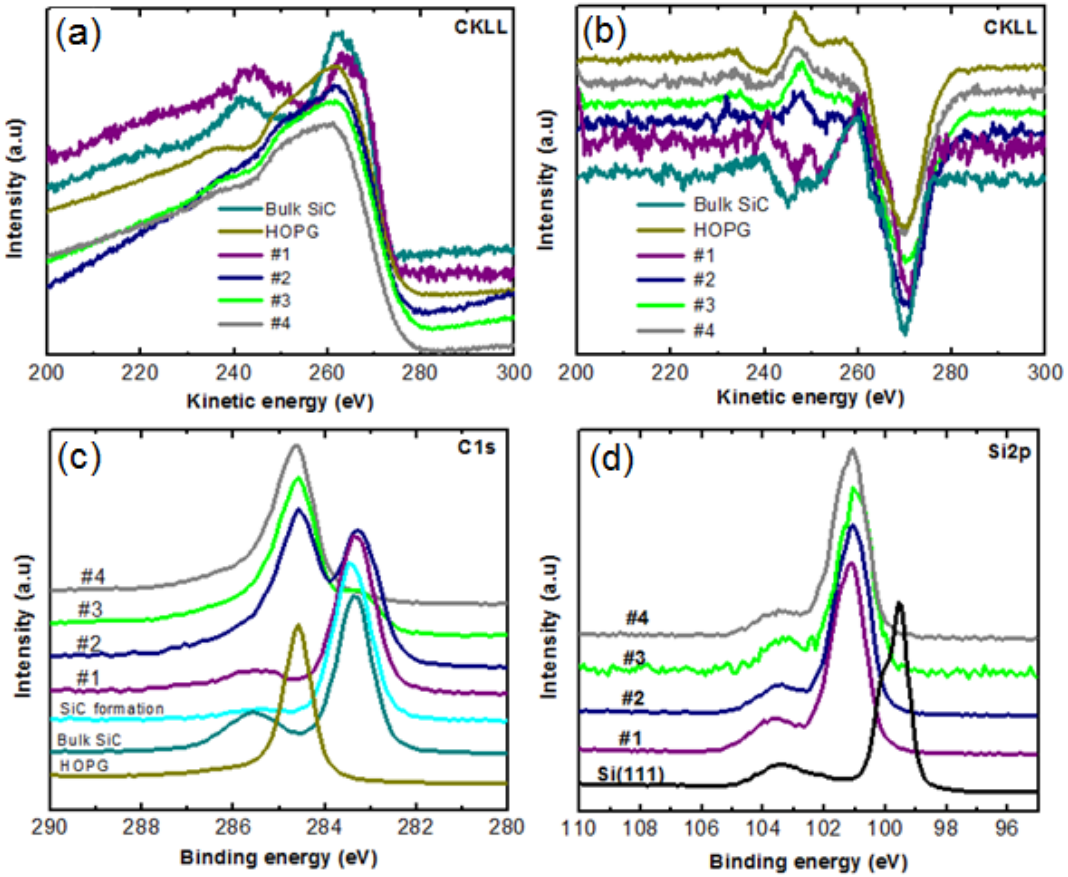

Fig. 4.10: (a) AES spectra around the C_{KLL} transition of SiC growth and after carbon deposition on top of SiC layers (samples #1 → #4); (b) Differentiated spectra with respect to the kinetic energy; (c) C 1s and (d) Si 2p XPS spectra of corresponding samples (pure Si(111), HOPG and SiC as references).

Likewise, Fig. 4.10 (d) shows the Si 2p spectra which mirror the results from the C 1s core level. Compared with bare Si(111), the strong peak at 101 eV corresponds to SiC formation in all samples. The broad peak at 103.5 eV corresponds to oxidation after exposure to atmosphere.

Raman measurements were performed using a 514 nm laser to investigate the C-C vibrations in the four samples (Fig. 4.11).

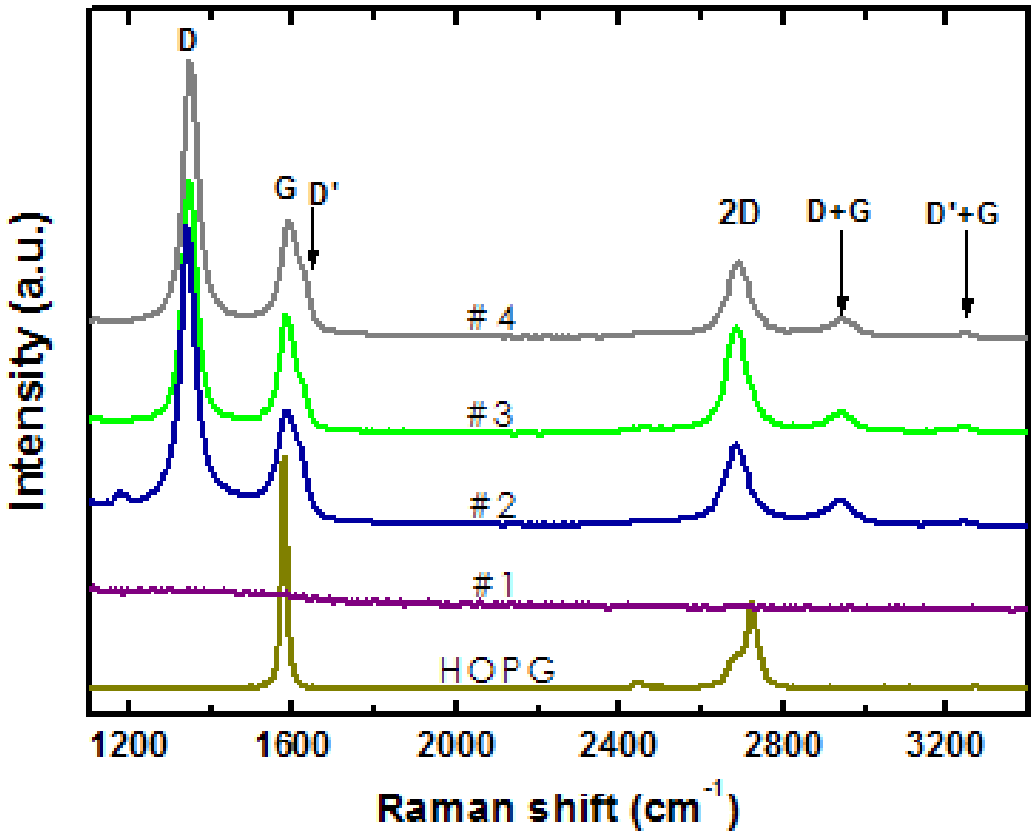

Fig. 4.11: Raman measurements for different studied samples #1, #2, #3, and #4.

Sample #1 does not show the typical sp^2 related signatures of C-C bonds while graphitic bonds are present in remaining samples with the appearance of G (1587 cm^{-1}), 2D (2696 cm^{-1}) and defect-related D (1350 cm^{-1}) and D' (1620 cm^{-1}) bands. This confirms the graphitic nature of the grown layers in good agreement with our AES and XPS characterization. In general, the presence of G and 2D bands is considered as characteristic

for graphene [128]. Thus, it can be inferred that graphene layers formed on the surface of samples #2 → #4. Compared to HOPG, a few layers of graphene could be grown on our samples. According to our process, a thin SiC layer had been produced before graphene formation, which may induce a Raman shift of graphene related bands. Indeed, the G band of epitaxial graphene grown on C- and Si-terminated SiC has often similar frequency ($\sim$ 1586 - 1590 cm^{-1}), which is upshifted from $\sim$ 6 - 10 cm^{-1} compared to that of HOPG ($\sim$ 1580 cm^{-1}) [144, 166]. This is due to stress caused by the lattice mismatch between graphene and SiC. However, the 2D band is quite different in comparison with the one of HOPG (2726 cm^{-1}). For epitaxial multi-layer graphene on C-face SiC, it is $\sim$ 2730 cm^{-1} (higher) while it is 2702 cm^{-1} (lower) on Si-face SiC [167]. This is attributed to the interface interaction between graphene and Si-face SiC ($\sim$ 30 % of carbon atoms from the first graphene layer are covalently bonded to SiC [168, 169]), while such covalent bonds are absent at the interface between graphene and C-face SiC [53, 169]. The frequency of G and 2D bands of our materials is similar to that of epitaxial graphene on Si-face of 3C-SiC. A similar observation was made by Ouerghi et al. [146] who produced epitaxial graphene on Si-face 3C-SiC/Si(111) in UHV. However, a sharp D band implies that our graphene films contains a large number of defects.

To evaluate the quality of graphene layers, the crystallite size La of those graphitic samples was estimated by using the equation (2.51) as in Table 4.2.

Samples	#2	#3	#4
I_D/I_G	2.29	2.11	2.18
I_{2D}/I_G	0.72	1.2	0.7
La(nm)	7.3	7.9	7.7

Table 4.2: I_D/I_G and I_{2D}/I_G ratios and average domain size of corresponding samples derived from the I_D/I_G ratio.

In order to learn the structural properties of our materials, sample #4 was analysed by STM. Fig. 4.12 shows large scale STM images of 3C-SiC (a) and after graphene formation on top of it (b) with a RMS $\sim$1.35 nm. Despite of the high surface roughness, atomic resolution is also found at smaller scales of 80×80 Å^2 (Fig. 4.12 (c)) and 35×35 Å^2 (Fig. 4.12 (d)) on the same sample. The triangular shape can be explained by the fact that the AB stacking of the layers as in graphite breaks the symmetry, leading to two inequivalent carbon atoms per unit cell [165].

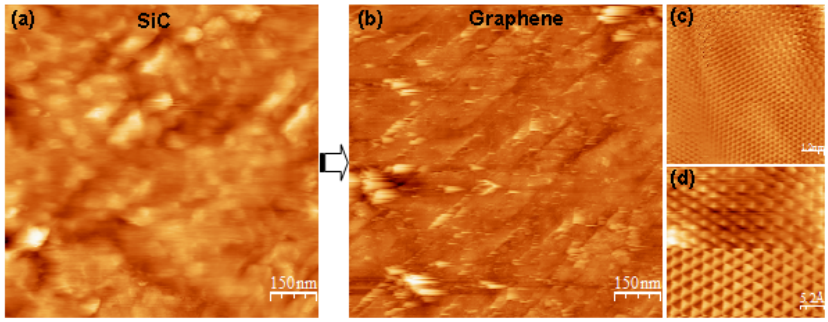

Fig. 4.12: STM images of sample #4 (a) 1×1 μm^2 (V_{Sample} = +4.0 V, I_{Tunnel} = 0.6 nA) after SiC growth and (b) 1×1 μm^2 (V_{Sample} = +4.0 V, I_{Tunnel} = 0.35 nA) after graphene formation on top by more carbon deposition at the substrate temperature of 1000 °C; (c) 80×80 Å^2 (V_S = −0.1 V, I_T = 10 nA) and (d) 35×35 Å^2 (V_S = −0.1 V, I_T = 10 nA) showing atomic resolution of the AB stacking order in the graphene hexagonal lattice.

In summary, we have grown graphene on Si(111) through prior formation of several SiC layers, followed by a few layers of *a*-C deposited at room temperature. They could act as a barrier to prevent out-diffusion of silicon atoms from the substrate before graphene formation. The quantity of the sp^2 bonded carbon increases as a function of the growth time during carbon deposition at a substrate temperature of 1000 °C. Real space STM images confirm the structural properties of our materials with AB stacking of a typical graphene lattice. However, the high defect density as well as the small size of graphene domain still remain a problem which is probably caused by presence of *a*-C buffer layers.

c. Model 3: C/3*C*-SiC/Si(111)

This part is adapted from ***Trung et al, Journal of Applied Physics 115, 163106 (2014)***.

We tried to remove the a-C buffer layers and deposited directly carbon atoms on 3C-SiC/Si(111) at a substrate temperature of 1000 °C. In this case, SiC buffer layer is expected to form as a direct template for graphene formation. Fig. 4.13 sketches the expected atomic arrangement between graphene and 3C-SiC/Si(111) substrate.

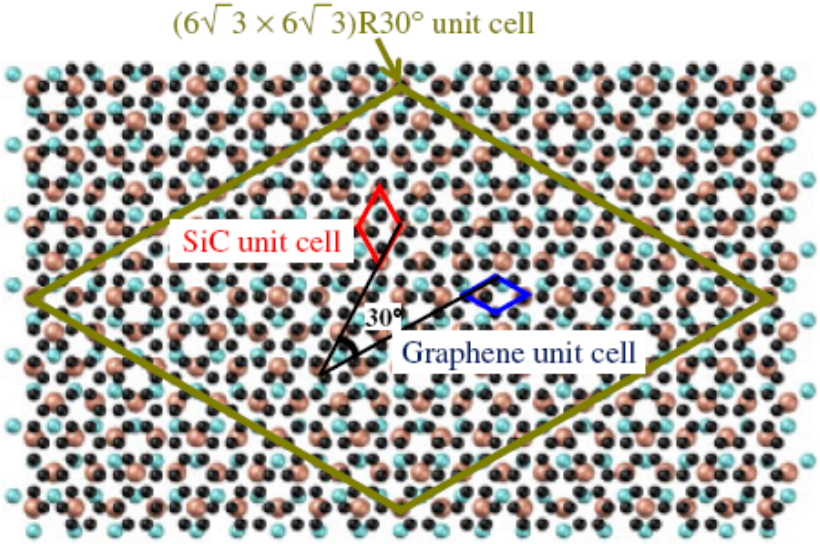

Fig. 4.13: Schematic of atomic arrangements of graphene and $3C$-SiC/Si(111) in real space. Image adapted from Ref. [170].

The quality of our graphene films is found as analysed below.

Fig. 4.14 is a growth process for direct carbon deposition at a substrate temperature of 1000 °C.

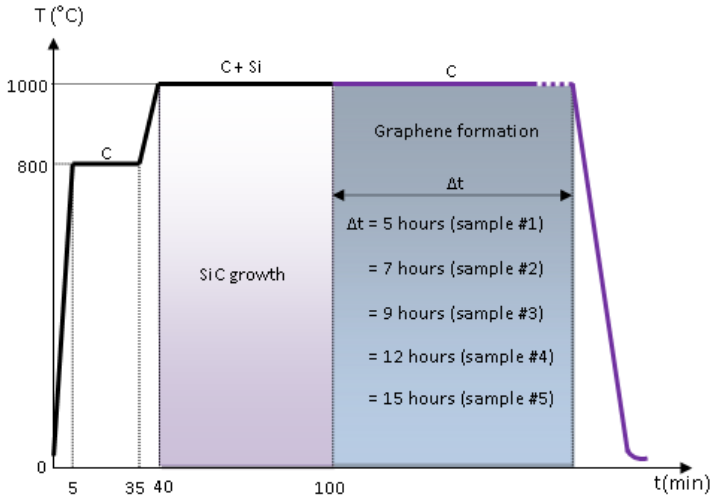

Fig. 4.14: Direct deposition of carbon atoms on $3C$-SiC/Si(111) where Si and C stand for silicon and carbon sources ON, respectively. The Si(111) substrates were cleaned by direct annealing up to $\sim$ 1050 °C as mentioned in section 4.2.

After one hour of SiC formation under carbon and silicon flux, we stop the silicon flux and continue carbon deposition at this substrate temperature with different times (5 hours (sample #1), 7 hours (sample #2), 9 hours (sample #3), 12 hours (sample #4) and 15 hours (sample #5)). The carbon flux is then shut off and the sample is cooled down to 200 °C at 20 °C $\cdot$ min^{-1}, and then free-cooled to room temperature.

Fig. 4.15 shows the RHEED patterns of Si(111)7×7 substrate and after carbon film formation.

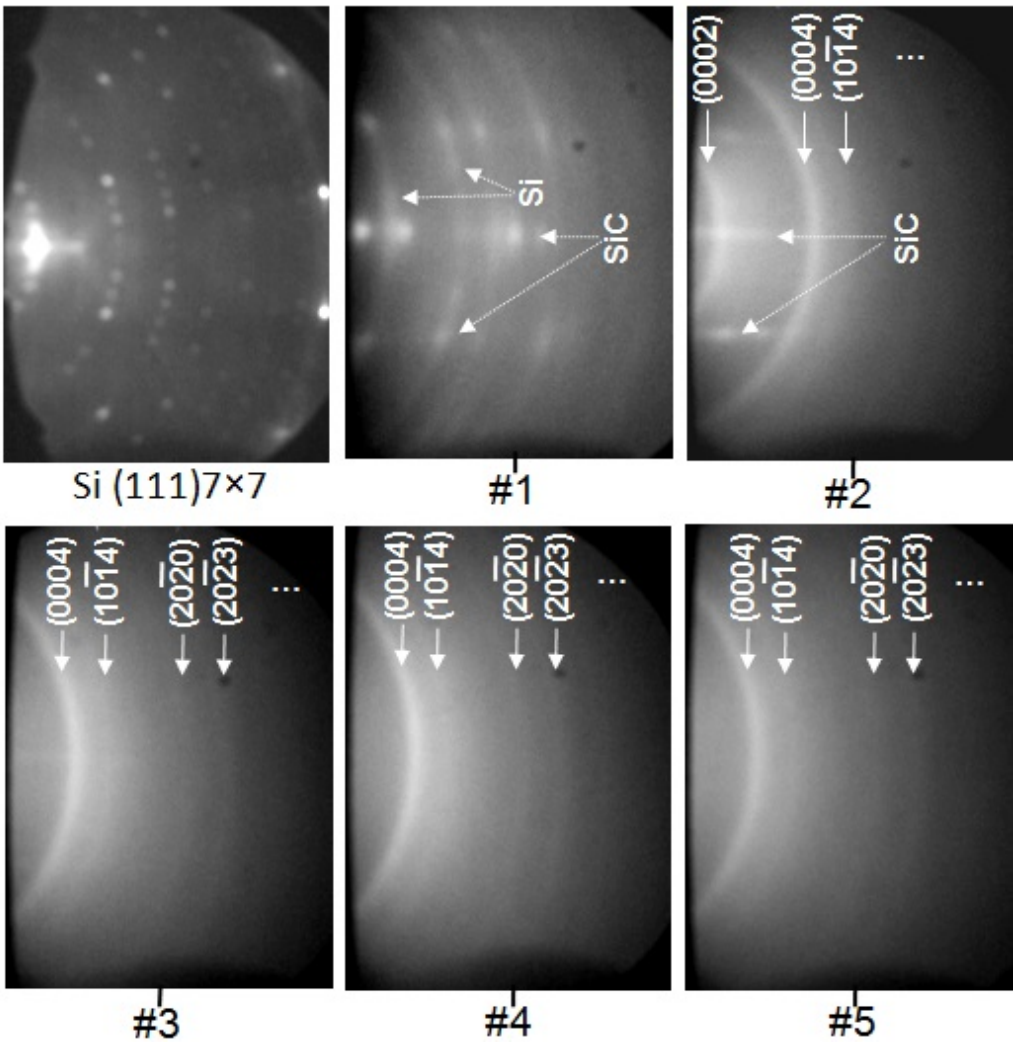

Fig. 4.15: RHEED patterns of the respective samples under various growth times on Si(111).

The diffraction rings are visible in the RHEED patterns of sample #1 after carbon deposition on top of SiC layers although they are still relatively faint. Besides SiC streaks, some faint Si spots could still be observed. This is probably due to diffusion from the substrate. The rings appear more clearly in sample #2 together with very faint SiC streaks, meaning that carbide formation still occurs during this growth time. SiC streaks disappear from RHEED patterns in the samples #3, #4, #5 after more carbon coverage. The sharp concentric rings can be ascribed to the presence of polycrystalline graphitic materials on top of the samples [54, 55]. In other words, the film comprises many small domains with different orientations.

From equation (2.39), the expected radii G_e (theory) can be calculated and compared with the measured radii G_m (experiment) as shown in Table 4.3. From these ring radii, it

(hkil)	G_e(Å^{-1})	G_m(Å^{-1})	percent error (%)
$(000\bar{2})$	1.87	1.85	1.1
$(10\bar{1}2)$	3.49	not observed	–
$(000\bar{4})$	3.75	3.69	1.6
$(10\bar{1}4)$	4.77	4.70	1.5
$(20\bar{2}3)$	6.53	not observed	–

Table 4.3: Expected (G_e) and measured (G_m) ring radii. The expected radii are computed using a lattice constant of 2.46 Å for graphene films.

is possible to determine the lattice constant. By using the rings (0002) and $(10\bar{1}4)$ in the sample #2, the lattice constant is found to be $a \simeq 2.50$ Å (close to the expected value of 2.46 Å for graphene) and $c = 6.78$ Å (corresponding to lattice spacing of 3.39 Å).
The AES spectra and their derivatives around the C_{KLL} transition on our samples were recorded in Figs. 4.16 (a) and (b), respectively. Compared with the spectra of SiC and HOPG, it is clear that the shape of the curve of sample #1 is similar to the one of SiC while samples #2, #3, #4, #5 are similar to the one of HOPG. It appears more clearly on the differentiated spectra (Fig. 4.16 (b)) with the energy difference D ($\sim 22.6\ eV$ for samples #2 $\rightarrow$ #5 as in HOPG and $\sim 11\ eV$ for sample #1 as in SiC) between the maximum and the minimum of the curve which has been analyzed already on such films [171].

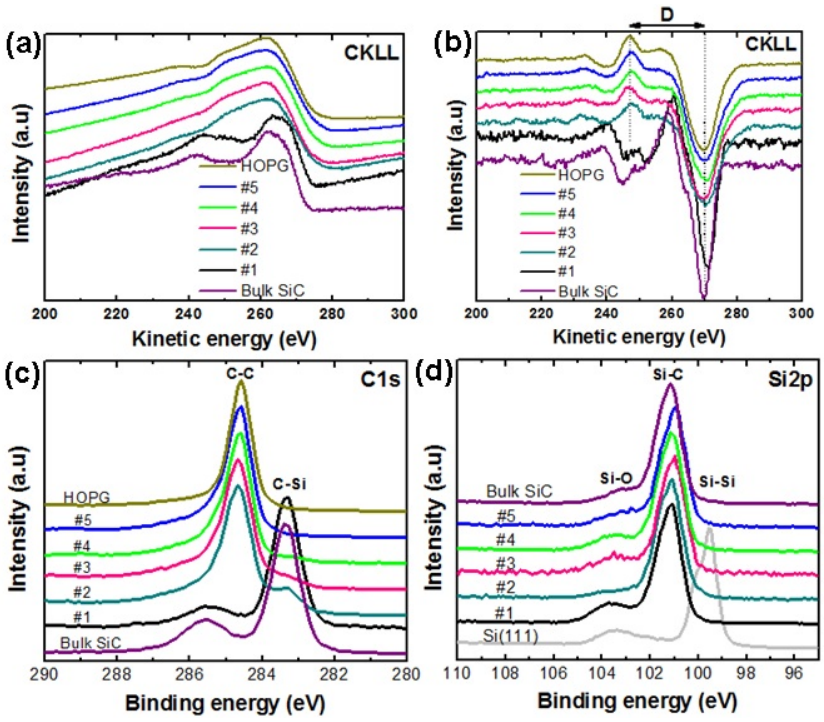

Fig. 4.16: (a) AES spectra around the C_{KLL} transition of the five different samples; (b) AES spectra, differentiated with respect to kinetic energy; (c) C 1s and (d) Si 2p XPS spectra of samples #1 to #5 (pure Si(111), HOPG and SiC as references).

The graphitic properties of the carbon film on four samples #2, #3, #4, #5 and the carbide on sample #1 are further confirmed by XPS data on C 1s core level shown in Fig. 4.16 (c). The spectrum of sample #1 is very similar to the SiC spectrum (except for the weaker component at 285.5 eV for sample #1, which corresponds to the native oxide found on SiC [160]) while the others look similar to the one of HOPG. A transition from Si-C bonds to C-C bonds occurs gradually in those samples when the growth time is longer. The main peak of sample #2 appears at 284.7 eV (corresponding to C-C bonding) which is practically identical to the one of HOPG while a weaker component is still observed at 283.3 eV (corresponding to Si-C formation). It is consistent with the appearance of the faint SiC streaks as confirmed by the RHEED pattern on this sample. In addition, the full width at half maximum (FWHM) of the dominant C 1s peaks in these four samples (0.96 eV (sample #2), 0.88 eV (sample #3), 0.79 eV (sample #4) and 0.75 eV (sample #5)) decreases substantially to approach the value for HOPG (0.64 eV), implying homogeneously bonded carbon films. The Si 2p spectra also reflect the

information on Si-C bonds and Si-Si bonds as seen on Fig. 4.16 (d). Unlike the Si(111) standard, the peak is detected only at 101 eV which corresponds to SiC formation in all samples. The broad peak in the Si(111) at 103.5 eV corresponds to oxidation after exposure to atmosphere.

Raman measurements using a 514 nm laser were performed to investigate the vibrations related to the C-C bonds in the samples. Samples #2, #3, #4 and #5 present the typical sp^2 carbon-related bands (D, G, D' and 2D bands at ~ 1350 cm^{-1}, ~ 1580 cm^{-1}, ~ 1620 cm^{-1} and ~ 2700 cm^{-1}, respectively), in good agreement with our AES and XPS characterization. Fig. 4.17 (a) shows the spectra recorded from our samples as well as the spectra from commercial multi-wall carbon nanotubes (MWCNTs) and CVD single layer graphene (SL), included for comparison.

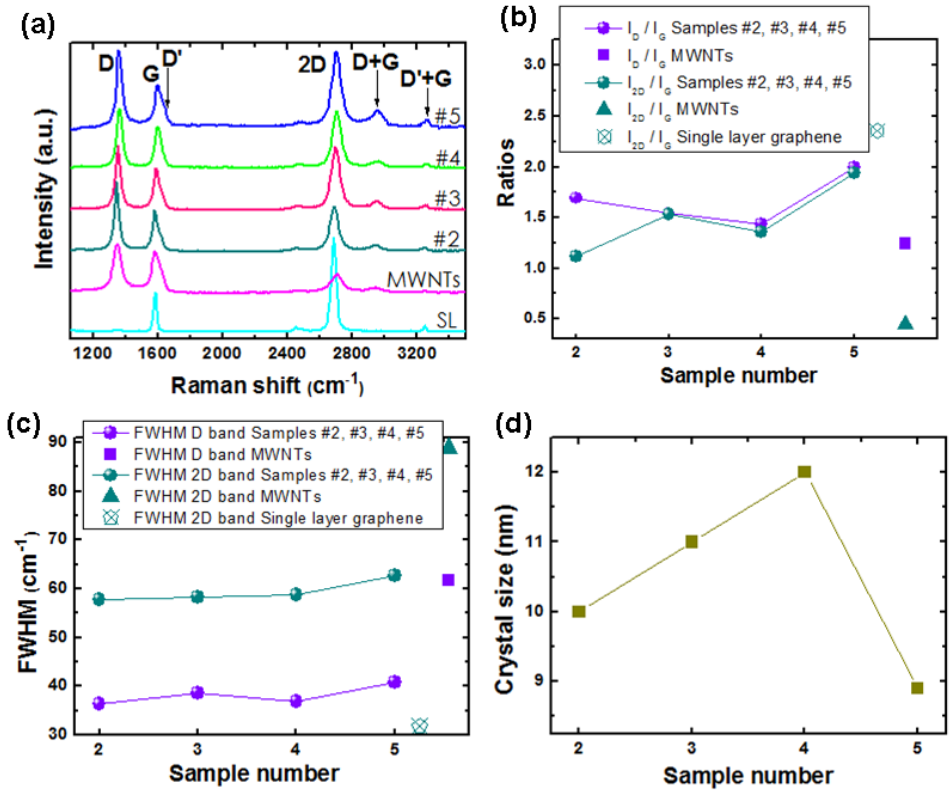

Fig. 4.17: (a) Raman measurements recorded at $\lambda = 514$ nm ($E_{laser} = 2.41$ eV) of samples #2, #3, #4, #5, MWCNTs and CVD-produced single layer graphene; (b) corresponding intensity ratios; (c) FWHM of D and 2D bands and (d) crystal size of the measured samples derived from the I_D/I_G ratios.

These spectra reveal very intense 2D- and defect-related bands (D and D' bands). By means of peak fitting, a quantitative analysis of the main spectral features was carried out and information about the intensities and FWHM of each peak were obtained. Fig. 4.17 (b) summarizes the information about the intensity ratios I_D/I_G and I_{2D}/I_G and isolated points represent similar ratios calculated from MWCNTs and SL graphene data. The values for the I_{2D}/I_G ratios, ranging from 1.1 (sample #2) to 1.9 (sample #5) indicate highly ordered structures, contrary to the low value of 0.44 for MWCNTs (decrease in quality due to strong treatments for purification and functionalization). These high I_{2D}/I_G ratio values suggest that the crystalline areas might be constituted of two or more layers of graphene since the values of the FWHM of the 2D bands for all samples lie around 60 cm^{-1} (see Fig. 4.17 (c)), while the value for SL is $\sim$ 30 cm^{-1}. Although these high intensities of the 2D band indicate the crystallinity of the samples, the values of the I_D/I_G ratios are even larger than the values of the I_{2D}/I_G ratios. Commonly, the presence of intense and broad D bands suggests defects in the honey-comb network, however, in this case the D bands are very sharp ($\sim 35-40$ cm^{-1} in our samples contrary to $\sim$ 60 cm^{-1} for MWCNTs) which could be the indication of particular types of symmetry breaking elements like frontiers among polycrystals rather than vacancies or bare edges. Further characterization is underway to determine the exact nature of these intriguing intense and sharp D bands. For the sake of relating the Raman data to crystal sizes, we have used the formula as defined by the equation (2.51). Results indicate an average crystal size of 9 - 12 nm depending on the growth time as shown on Fig. 4.17 (d).

In order to evaluate the homogeneity of samples at a larger scale, we have performed Raman maps of areas $\sim$ 45×30 μm^2. The resulting intensity maps are depicted in Fig. 4.18, where three columns represent the maps of I_{2D}/I_G ratios, the I_D/I_G ratios and the optical images of the corresponding areas, respectively, from left to right. The maps reveal a correlation between the optical images and the intensity ratios. Colored areas in the optical images correspond to the highest I_D/I_G and lowest I_{2D}/I_G ratios. In general the shapes found in the optical images are reproduced by the intensity ratios, suggesting a correlation between the morphology at the macro scale and the crystalline structure, surely derived during the hours of sample annealing.

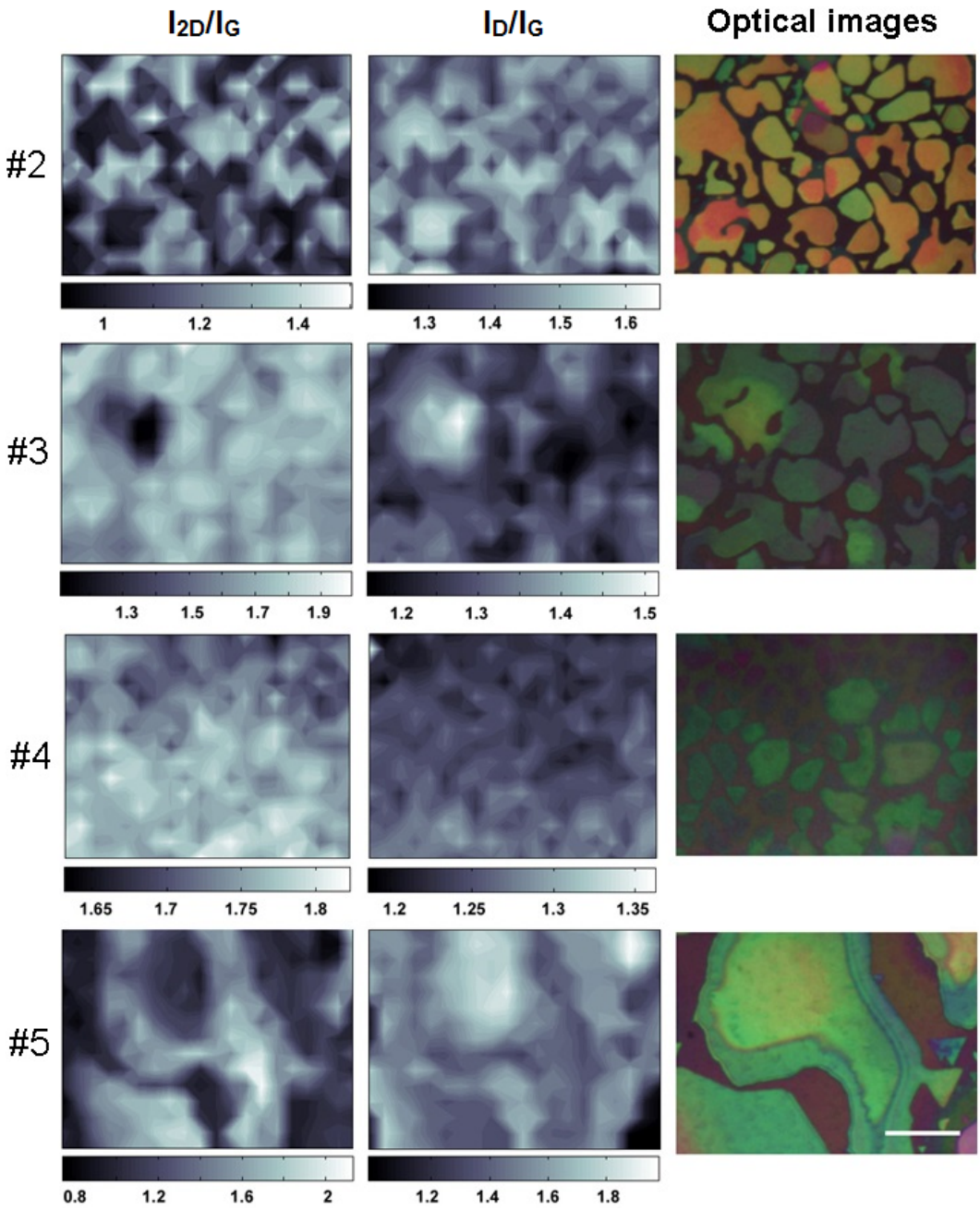

Fig. 4.18: Maps of I_{2D}/I_G (left), I_D/I_G (center) intensity ratios and corresponding optical images (right, scale bar 10 μm).

All graphitic samples are characterized by using HR-SEM and show similar surface morphology with the formation of islands which is probably induced by carbide buffer layers during carbon growth as seen on Fig. 4.19 (a).

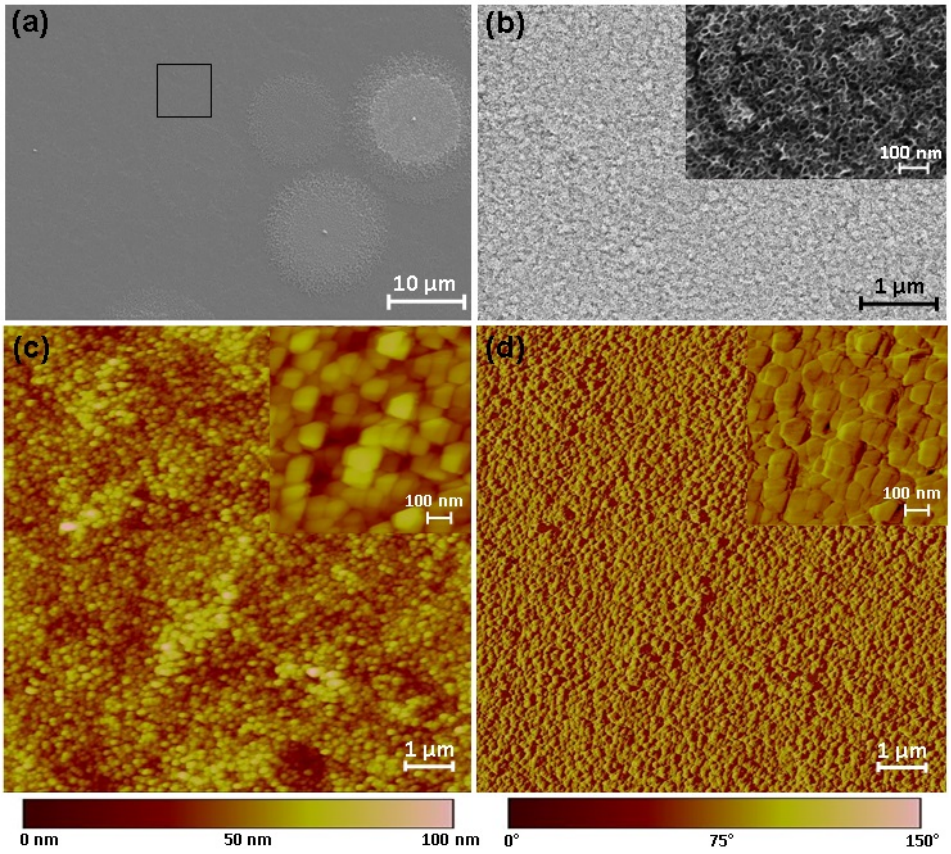

Fig. 4.19: (a) HR-SEM images showing the surface morphology and (b) a zoom-in on the square area of sample #5 observing surface structure like 3D porous network; (c) Surface topographic AFM images of sample #4 and (d) the corresponding phase image.

Here we show only the images of the sample #5 after 15 hours of direct carbon deposition to interpret micro-structural properties on such films. As observed, the surface of our materials seems to be folded and curved irregularly forming many small domains with a size of 10 - 40 nm like a porous graphene network (Fig. 4.19 (b)) as proposed by Zhang et al. [172]. RHEED patterns suggest that these domains are randomly oriented (see above). Furthermore, Fig. 4.19 (c) is an AFM surface topography image of sample #4, which shows a rather rough morphology containing many different grains and the corresponding AFM phase image obtained inside different graphene grains exhibits only weak contrast differences as seen in Fig. 4.19 (d). It represents an indication that the differences in physico-chemical properties among the different grains are not large. This is in accordance with our XPS and Raman analysis on this sample.

STM images strongly support the previous conclusions. We took a large scale STM image on the sample #5 with a RMS roughness of about 4.1 nm on Fig. 4.20 (a).

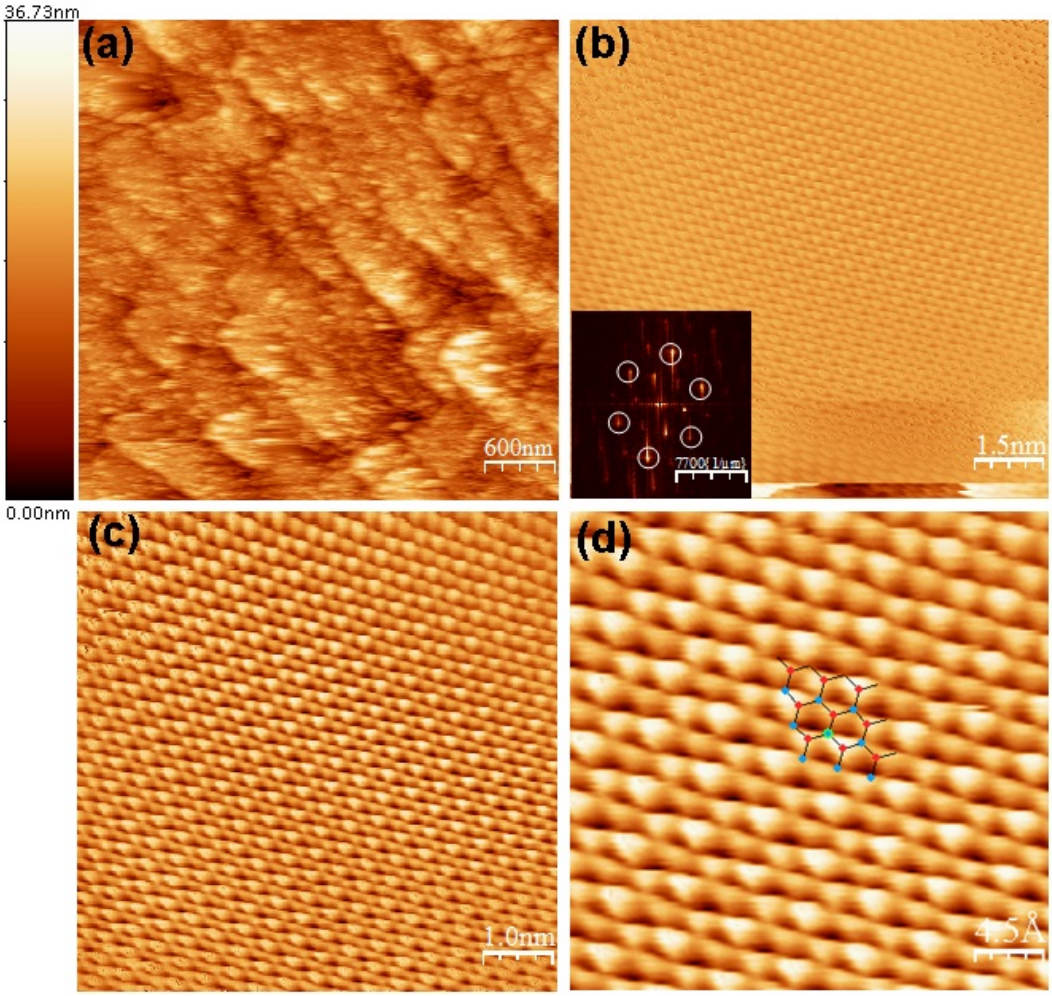

Fig. 4.20: STM images of sample #5 (a) 4×4 μm^2 (V_{Sample} = +5.5 V, I_{Tunnel} = 0.45 nA); (b) 100×100 Å^2 (V_S = −0.12 V, I_T = 10 nA) with a corresponding FFT image in the inset that exhibits diffraction pattern of hexagonal film structure; (c) 70×70 Å^2 (V_S = −0.12 V, I_T = 10 nA); (d) 30×30 Å^2 (V_S = −0.12 V, I_T = 10 nA) showing the honeycomb lattice of a graphene sheet.

Despite this roughness, atomic resolution is still found at smaller scales of 100×100 Å^2 (Fig. 4.20 (b)), 70×70 Å^2 (Fig. 4.20 (c)) and 30×30 Å^2 (Fig. 4.20 (d)) on the same sample with a corresponding FFT image in the inset of Fig. 4.20 (b), which exhibits

the diffraction pattern of hexagonal structure on this sample. These images can be explained by the fact that the AB stacking of the layers breaks the symmetry of the graphene hexagonal lattice, leading to two inequivalent carbon atoms per unit cell [165]. Therefore, they appear as the bright spots in the image in which carbon atoms with a higher electron density lie directly above atoms in the plane below and represent only half the total number of carbon atoms in the plane.

In summary, we have grown graphene directly on Si(111) through the prior formation of several SiC layers which could act as a template for graphene formation. The results confirm a determinant influence of the growth time on the quality of graphene at a substrate temperature of 1000 °C. In particular, we obtained real space STM images that show evidence of typical stacking order of graphene layers.

d. Model 4: C/Si/3*C*-SiC/Si(111)

Because the production of low surface roughness and homogeneous films still remain a challenge, we continue investigating the structural and electronic properties of our materials at various substrate temperatures using SiC buffer layers with different thicknesses. The goal is to reduce the surface roughness before graphene formation. For a test, we grew a SiC buffer four times thicker than the one of model 3. Then, the sample is annealed slowly up to $\sim$ *1200 °C under silicon sublimation (from a silicon source) in order to compensate and flatten the SiC surface. We produced four different samples at various substrate temperatures from 900 °C to 1100 °C for comparison. As a result, it is found that the surface roughness is improved, but graphene film still contains many defects and randomly oriented SiC islands appear on the surface due to out-diffusion of silicon atoms from the substrate. In order to overcome this problem, other samples were produced with different thicknesses of SiC buffer layers at the same substrate temperature of 1100 °C and then, the same conditions were applied for carbon growth. We found that a thicker SiC buffer layer grown before graphene formation improves the structural quality of the graphene layers.*

The procedure used to obtain graphene formation directly on Si(111) is shown in Fig. 4.21.

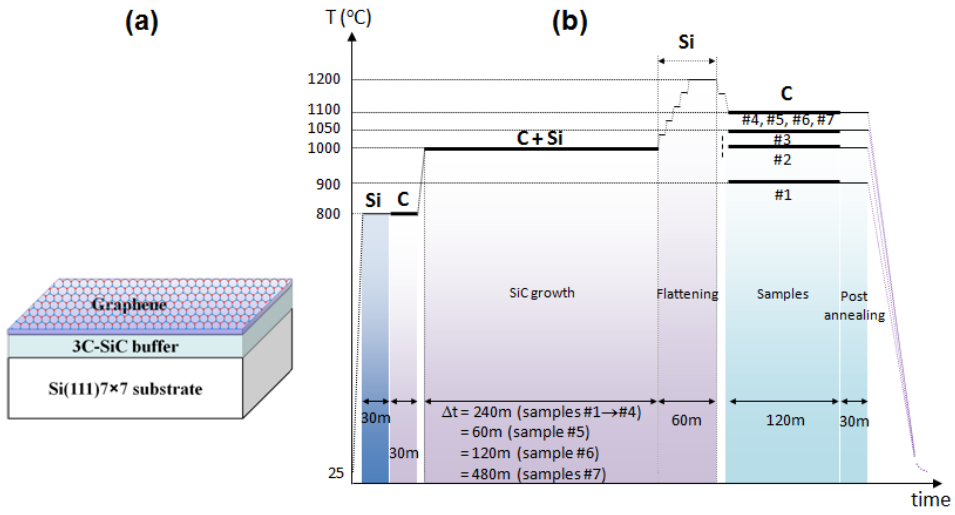

Fig. 4.21: (a) Schematic diagram and (b) growth process for graphene formation on Si(111) 7×7 substrate where Si and C stand for silicon and carbon sources ON, respectively. The Si(111) substrates were cleaned by direct annealing up to ∼ 1050 °C as mentioned in section 4.2.

After four hours of SiC formation under carbon and silicon flux, we stop the carbon flux and gradually increase the substrate temperature in few steps up to ∼ 1200 °C for compensating and flattening the SiC surface [63, 173]. Then, we stop the silicon flux and restart carbon deposition for two hours at various substrate temperatures: 900 °C (sample #1), 1000 °C (sample #2), 1050 °C (sample #3), 1100 °C (samples #4, #5, #6 and #7). Sample #5 has a thinner SiC buffer layer while it is thicker for samples #6 and #7 (1 hour, 2 hours and 8 hours of SiC growth for samples #5, #6 and #7, respectively instead of 4 hours as for the other samples). The corresponding thickness of this SiC buffer is calculated for each sample: ∼ 3 nm (sample #5), ∼ 6 nm (sample #6), ∼ 12 nm (sample #1 → #4), ∼ 24 nm (sample #7). We chose the substrate temperature of 1100 °C as a test for growing different thicknesses of SiC buffer layer in order to evaluate the role of this buffer on the quality of graphene formation. The carbon flux is then shut off and the sample is maintained for another 30 min at the same substrate temperature (post annealing). Finally, it is cooled down to 200 °C at 20 °C · min^{-1} and then free-cooled to room temperature.

Fig. 4.22 (a) shows the Auger spectra around the Si_{LVV}, C_{KLL} transitions of our samples.

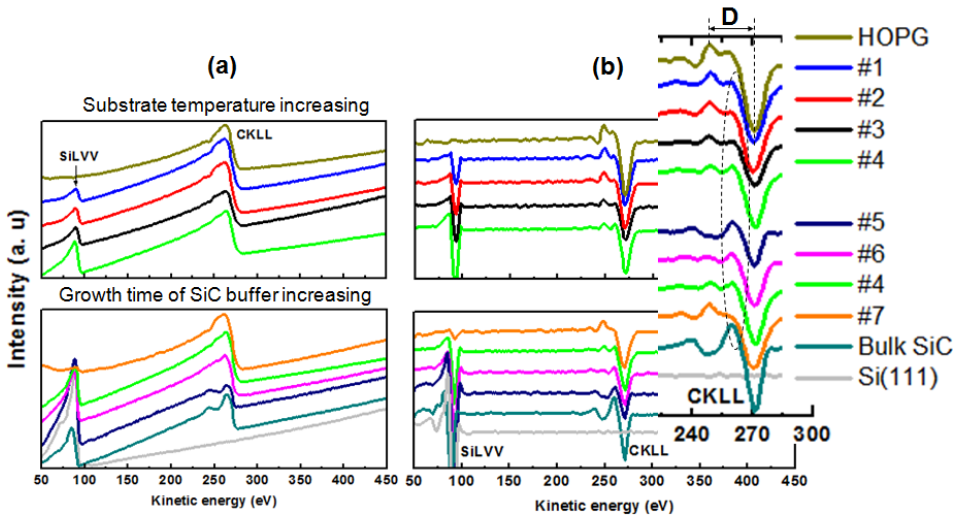

Fig. 4.22: (a) AES spectra around the Si_{LVV} and C_{KLL} transitions of the seven different samples as well as HOPG, bulk SiC and Si(111) as references; (b) The differentiated spectra. The dotted ellipse in the magnified C_{KLL} spectra shows the region where features from SiC are located

The Si_{LVV} intensity gradually increases while the curve shape of the C_{KLL} transition slightly changes from samples #1 to #4. This can be explained by an enhanced diffusion of Si atoms from the substrate through the SiC layer due to the high activity of Si atoms underlying layers with raising the substrate temperature [174]. This is known to increase the SiC buffer thickness as the Si bonds with carbon atoms from the surface [54, 55, 75]. After differentiating the spectra (Fig. 4.22 (b)), the energy difference D was measured $\sim$ 22.6 eV for HOPG and $\sim$ 11 eV for SiC [171, 175]. Compared to HOPG, it is obvious that all samples contain graphitic carbon except for samples #5 and #6. In addition, one can see that a small feature associated with SiC marked by a vertical dashed ellipse is strongest in sample #4 among the first four samples, meaning that the transition from graphitic carbon to carbide occurs more strongly in this sample. Samples #5 and #6 present the C_{KLL} in the same state as carbon from silicon carbide although a very small peak at $\sim$ 248.5 eV can still be observed in sample #6, indicating that a little graphitic carbon could begin forming in this sample. More graphitic carbon was found in sample #4 and the most in sample #7 with rising the thickness of SiC buffer layer. So, the differences between the AES spectra of samples #4, #5, #6 and #7 in this case are mainly caused by the different thicknesses of SiC layer which acts as a barrier to

stabilize the surface and prevent the reaction of Si atoms from the substrate with carbon atoms on top of the SiC layers [55].

The AES analyses are confirmed by XPS measurements of the C 1s core level shown in Fig. 4.23 (a) for all samples together with the bulk SiC and HOPG for comparison.

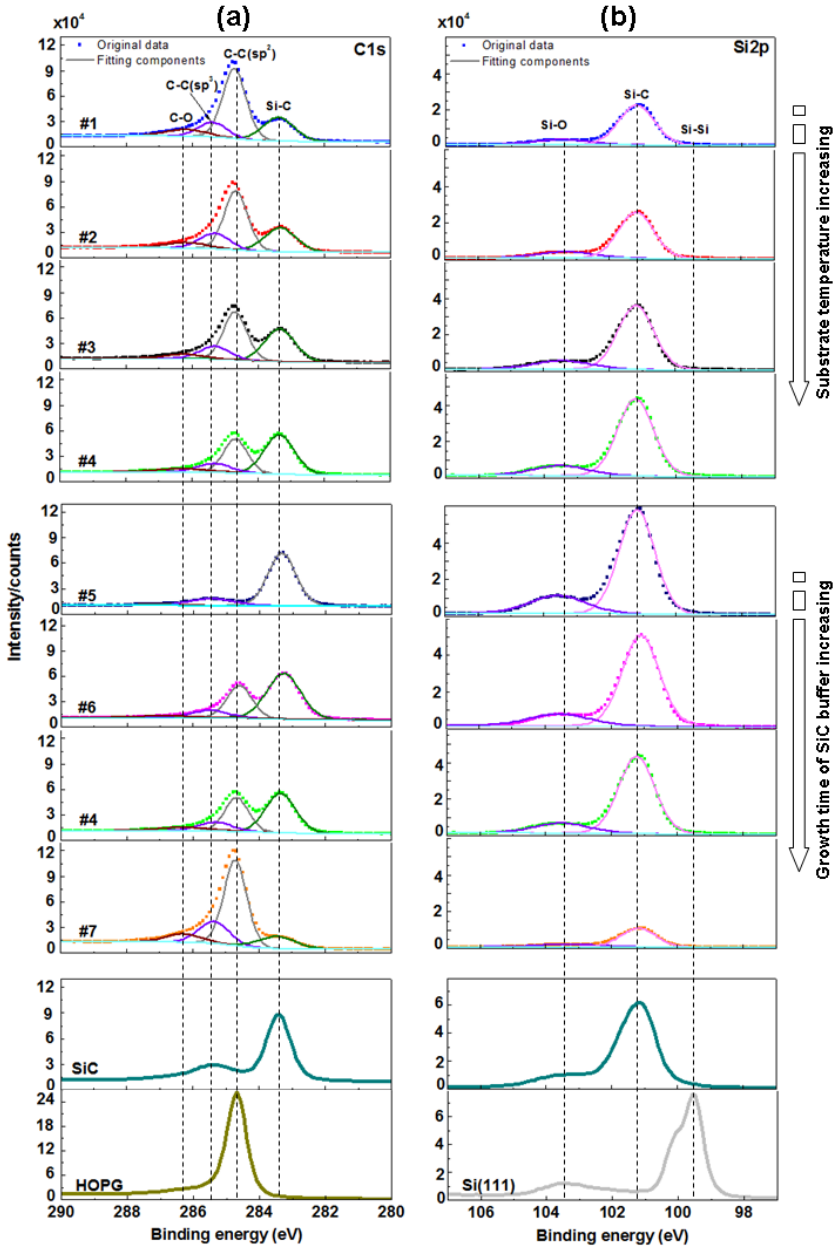

Fig. 4.23: (a) C 1s and (b) Si 2p XPS spectra of samples #1 to #7 (HOPG, Si face of bulk 6H-SiC and Si(111) used as references).

Besides the main peak at 284.7 eV (corresponding to sp^2 C-C bonding), a second component is observed at 283.3 eV (corresponding to Si-C bonding). A third component at 285.4 eV should correspond to C-C sp^3 bonding which is related to the interface layer between $\left(6\sqrt{3}\times 6\sqrt{3}\right)$R30° reconstruction of the $3C$-SiC and the first graphene layer [146, 176, 177]. The fourth component at 286.3 eV corresponds to C-O bonding which comes from exposure to air during their transfer into the XPS spectrometer [177]. For the first four samples, one can see a gradual change from sp^2 C-C bonds to Si-C bonds with rising growth temperature. Indeed, the intensity ratio of the sp^2 peak area (I_C^G) and Si-C peak area (I_C^{SiC}) for those four samples decreases with increasing temperature as shown in Table 4.4. It is clear that the formation of sp^2 bonded carbon evolves as

Ratio	#1	#2	#3	#4	#5	#6	#7
I_C^G/I_C^{SiC}	2.19	1.80	1.42	0.71	0.0	0.52	4.25

Table 4.4: Summary of the ratio I_C^G/I_C^{SiC} for different studied samples.

a function of the growth temperature as well as the thickness of SiC buffer layer. The thicker SiC buffer is, the higher intensity of sp^2 C-C peak is observed. This confirms the important role of SiC buffer layers in preventing more Si-C bonding near or on the surface during carbon deposition for graphene formation at the same substrate temperature. It is consistent with AES analyses on these four samples.

The number n of graphene layers on $3C$-SiC/Si(111) can be estimated from the intensity of the sp^2 and SiC components in the C $1s$ spectra by using equation (2.47). This intensity is attenuated according to the Beer-Lambert law. So, the intensity of the sp^2 carbon peak is

$$I_C^G \propto N_G \frac{1-e^{\frac{-nh}{\lambda_C^G\cos\theta}}}{1-e^{\frac{-h}{\lambda_C^G\cos\theta}}}, \tag{4.1}$$

and the intensity of Si-C peak is expressed by

$$I_C^{SiC} \propto N_{SiC} \frac{e^{\frac{-[(n-1)h+k]}{\lambda_C^G\cos\theta}}}{1-e^{\frac{-l}{\lambda_C^{SiC}\cos\theta}}}, \tag{4.2}$$

where N_G and N_{SiC} are the number of carbon atoms per cm^2 in one atomic plane within the corresponding materials ($N_G = 3.8\times 10^{15}$ cm^{-2}, $N_{SiC} = 1.2\times 10^{15}$ cm^{-2}); λ is the inelastic mean free path (IMFP) of photoelectrons from carbon atoms in graphene (λ_C^G)

or in SiC layers (λ_C^{SiC}) which can be found from NIST Standard Reference Database 71; θ is the emission angle (measured with respect to the surface normal).

From (4.1) and (4.2), the I_C^G/I_C^{SiC} ratio will be given by

$$\frac{I_C^G}{I_C^{SiC}} \propto \frac{N_G}{N_{SiC}} \times \left(\frac{1 - e^{\frac{-nh}{\lambda_C^G \cos\theta}}}{1 - e^{\frac{-h}{\lambda_C^G \cos\theta}}} \right) \times \left(\frac{e^{\frac{-[(n-1)h+k]}{\lambda_C^G \cos\theta}}}{1 - e^{\frac{-l}{\lambda_C^{SiC} \cos\theta}}} \right)^{-1} \tag{4.3}$$

By considering an interlayer spacing of h=3.37 Å for graphene layers, l=2.52 Å for SiC layers and the interfacial distance between graphene and Si face of SiC layers k=1.65 Å (Fig. 4.24) [146, 178, 179], Eq. (4.3) can be solved for the number of graphene layers n. According to our calculation, about 8 graphene layers are formed on the $3C$-SiC surface in the case of sample #7 (average error ±0.5). Here we only calculate the number of layers for sample #7 because it is sufficiently homogeneous and has no SiC islands at the surface (see STM analyses).

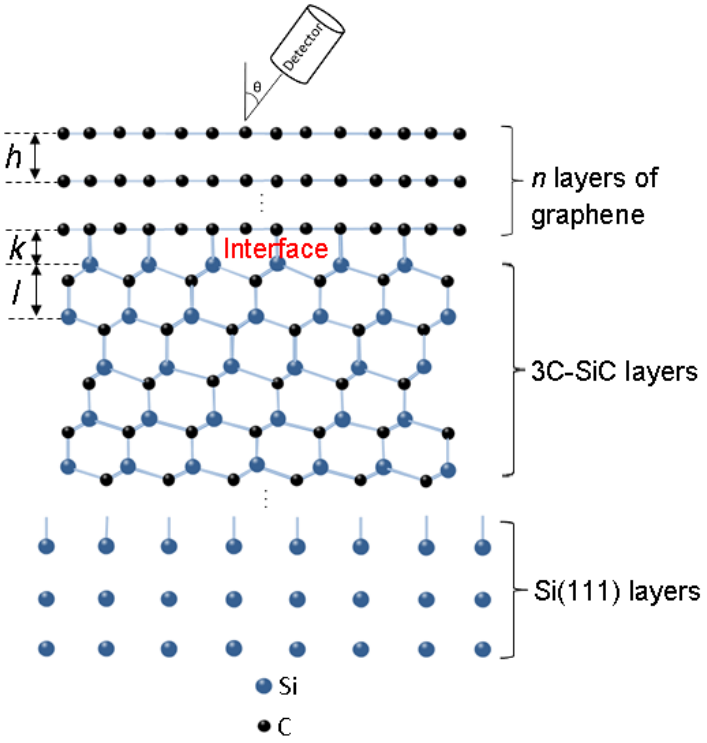

Fig. 4.24: Model used for the calculation of number of graphene layers on $3C$-SiC/Si(111) substrate.

Likewise, information on the Si-C and Si-Si bonds can be derived from the Si $2p$ spectra as shown in Fig. 4.23 (b). Compared to the Si(111) reference, the peak is detected only at 101.2 eV which corresponds to the SiC formation in all samples. Changes in the intensity of Si-C peak depending on the substrate temperature confirm our conlusions. The broad peak at 103.5 eV corresponds to oxidation after exposure to atmosphere.

To investigate the quality and homogeneity of the graphitic layers, Raman spectra were measured using a 514 nm laser. The results are shown in Fig. 4.25, together with the spectra of Si(111), $6H$-SiC and HOPG as references. The presence of G (1587 cm^{-1}), 2D (2696 cm^{-1}) and defect-related D (1350 cm^{-1}) and D' (1620 cm^{-1}) bands confirm the graphitic nature of the grown layers. This agrees with our AES - XPS characterization. As marked by the dashed vertical lines in the figure, the peaks at 794 cm^{-1} and 972.5 cm^{-1} should be TO and LO phonons of $3C$-SiC layers forming on Si(111) [180]. The sharp peak at 520.7 cm^{-1} comes from the crystalline Si substrate.

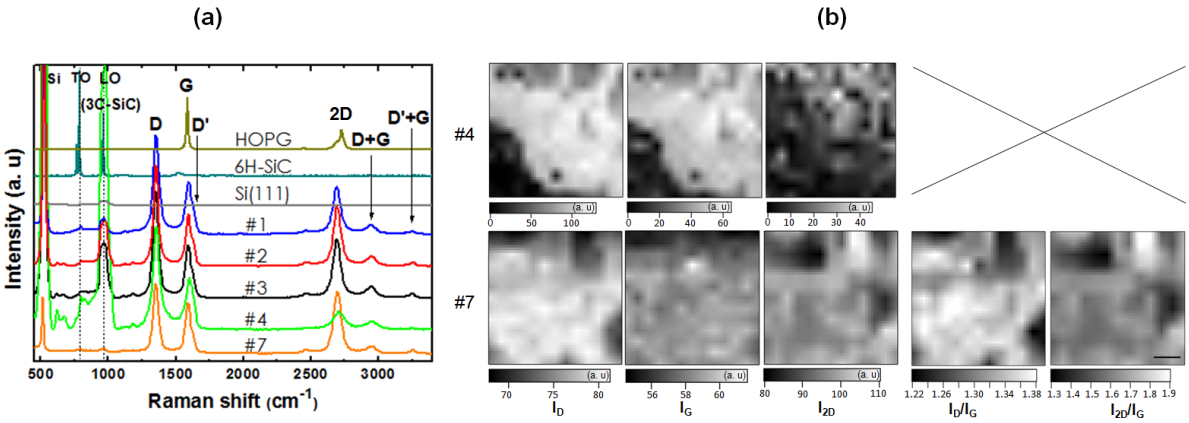

Fig. 4.25: (a) Raman measurements recorded at $\lambda = 514$ nm ($E_{laser} = 2.41$ eV) of samples #1, #2, #3, #4, #7, pure Si(111), $6H$-SiC and HOPG as references; (b) Intensity maps of I_D, I_G, I_{2D}, I_D/I_G, and I_{2D}/I_G on $\sim 30 \times 30$ μm^2 from samples #4 and #7 (scale bar 5 μm).

The ratios of I_D/I_G and I_{2D}/I_G for each sample are summarized in Table 4.5. The different values of I_{2D}/I_G ratio indicate the different degree of stacking order in the samples. Sample #4 displays the lowest degree of ordered structure while the most graphitic film is sample #2. Although the high intensities of the 2D band indicate

the crystallinity of the samples, the values of the I_D/I_G ratios are even larger than the values of the I_{2D}/I_G ratios due to very sharp D bands ($\sim 35-40$ cm^{-1}). As discussed the previous section, it could be the indication of particular types of symmetry breaking elements like frontiers between polycrystals rather than vacancies or bare edges. Likewise, sample #7 presents lower D band and higher 2D band compared to sample #4, confirming that the thicker SiC layers could help to improve the quality of graphene formation at the same substrate temperature. To estimate the size of graphene domains, we use the equation (2.51). A mean crystal size is found as calculated in Table 4.5.

Samples	#1	#2	#3	#4	#7
I_D/I_G	1.93	1.89	1.95	2.44	1.30
I_{2D}/I_G	1.30	1.82	1.80	0.81	1.83
Domain size (nm)	8.7	8.9	8.6	6.9	12.9

Table 4.5: I_D/I_G and I_{2D}/I_G ratios from different samples for comparison and average domain size derived from the I_D/I_G ratio.

Fig. 4.25 (b) shows the Raman maps of D, G, 2D, I_D/I_G and I_{2D}/I_G in areas $\sim 30 \times 30\ \mu m^2$ on samples #4 and #7 for a comparison of the homogeneity of our samples. For sample #7, the map of ratio I_{2D}/I_G shows high intensity ratio even more than the ratio of I_D/I_G. This indicates the high crystalline structure of sample #7 with less defects than in sample #4. The intensity ratio of sample #4 is not calculated because the surface is not completely covered with graphitic carbon.

We took some SEM images at large scale on sample #2 (Fig. 4.26 (a)) and sample #7 (Fig. 4.26 (d)) (the best graphitic quality) showing the sample surface that is quite flat. Similarly, large scale STM images were also recorded on corresponding samples for a confirmation with a root mean square roughness of about 0.42 nm (Fig. 4.26 (b)) and 0.88 nm (Fig. 4.26 (e)) for samples #2 and #5, respectively. Compared to 4.1 nm in the case of samples prepared according to model 3 (C/3C-SiC/Si(111)), the surface roughness is certainly improved. The image of sample #2 contains randomly distributed objects with different contrast on the surface which could be SiC islands induced during annealing. Their size can reach $\sim$ 3 nm in height and $\sim$18 nm in width. Similar observation was made by STM on samples #1 and #3 (not shown here) while sample #7 is free of such islands. This supports our earlier conclusions on the role of SiC buffer layer. It is really a necessary barrier for preventing the appearance of Si atoms

near or on the surface during graphene formation at high temperatures.

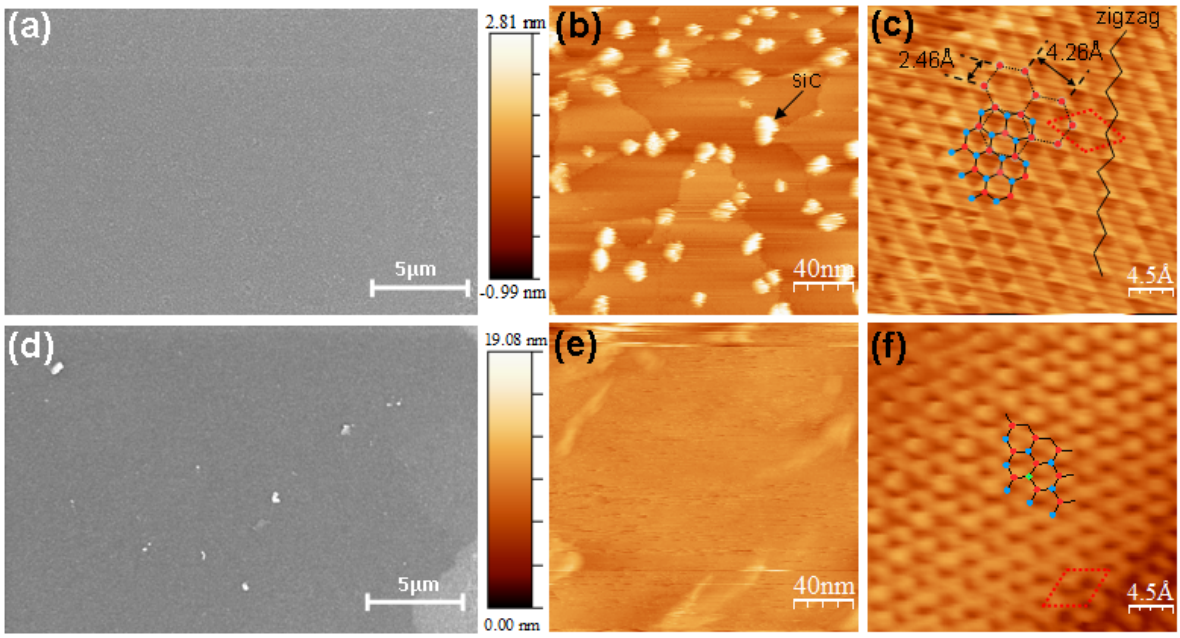

Fig. 4.26: (a) SEM image of sample #2 and its STM images (b) 200×200 nm^2 (V_{Sample} = +3.0 V, I_{Tunnel} = 0.35 nA); (c) 30×30 Å^2 (V_S = −1.4 V, I_T = 30 nA); and (d) SEM image of sample #7 and its corresponding STM images (e) 200×200 nm^2 (V_S = +5.0 V, I_T = 0.35 nA); (f) 30×30 Å^2 (V_S = −0.2 V, I_T = 25 nA) showing the atomic resolution of the AB stacking order of a typical graphene lattice.

Likewise, Figs. 4.26 (c) and (f) display the atomic resolution at smaller scale of 30×30 Å^2 on samples #2 and #7. In general, the images are characteristic of AB (Bernal) stacking order as in a typical graphene hexagonal lattice. However, hexagonal shapes are also observed on the surface from the combination of bright spots in a graphene network (Fig. 4.26 (c)). They appear only on the zigzag direction which originally comes from carbon atoms with higher electron density on corresponding armchair direction of the Bernal stacked graphene lattice as shown. The dotted rhombus in red indicates the unit cell of $\left(\sqrt{3}\times\sqrt{3}\right)$R30° superperiodic patterns [181]. This may be explained by the interference of electron waves in the vicinity of an amchair edge causing the creation of such honeycomb superlattice patterns in the graphene sheet [181, 182].

From the above analyses, it is possible to grow graphene on Si(111) wafer through the prior formation of SiC buffer layers which is considered as a template for graphene

formation. However, very high temperature annealing (∼1200 °C) needed to flatten the surface induces out-diffusion of Si atoms from the substrate. Therefore, a sufficiently thick SiC buffer layer is necessary to prevent out-diffusion of Si.

In summary, the quality of obtained graphene on Si(111) via direct carbon deposition depends not only on the substrate temperature but also on the SiC buffer layer thickness. As demonstrated, the formation of sp^2 bonded carbon is really a strong function of the substrate temperature during graphene growth. In addition, we also observed an improvement of the graphene quality when increasing the thickness of SiC buffer layer and an increase in number of graphene layers as confirmed by XPS at the same substrate temperature of 1100 °C. STM images confirmed the structural property, the surface roughness as well as the size of our graphene domain although a high defect density is still shown by the presence of a D band on Raman spectra of such films.

4.3.3. Summary

From the experimental analyses of four different models, we summarize some main parameters for comparison as shown in Table 4.6. It turns out that model 4 produces the best graphitic films on Si(111) substrate.

Parameters	RMS (nm)	I_D/I_G	I_{2D}/I_G	L_a (nm)
Model 1: C/*a-C*/Si(111)	very poor crystallinity			
Model 2: C/*a-C*/*3C-SiC*/Si(111)	1.35	2.11 - 2.2	1.0 - 1.2	7.9
Model 3: C/*3C-SiC*/Si(111)	4.1	1.65 - 1.8	1.2 - 1.35	11.9
Model 4: C/*Si*/*3C-SiC*/Si(111)	**0.88**	**1.22 - 1.38**	**1.3 - 1.9**	**∼ 13**

Table 4.6: Summary of main parameters among four different studied models.

4.3.4. Discussion

As observed by experiments, diffusion of Si atoms from the substrate really impacts on the quality of graphene during carbon growth on Si(111). In order to support our explanation, in this work the SiC buffer layer is considered as a diffusion barrier for silicon. Therefore, we focus the discussion on the calculation of a diffusion profile for silicon from the substrate through SiC buffer layer. It is found that the concentration of

Si atoms at a specific time depends on the substrate temperature and on the thickness of SiC buffer layer.

a. Basics of diffusion

Diffusion is the oriented movement of substance (an atom, ion or molecule) from one region of high concentration to another region of low concentration. This movement can take place until an equilibrium state is reached. Dynamics of diffusion can be described by two ways: either a phenomenological or statistical methods. In the conext of this study, only the phenomenological method is used; it will be presented in the following sections. More detailed information about this topic can be found in Ref. [183].

b. Phenomenological approach

For the general case, diffusion in a solid can be expressed mathematically by using Fick's first law as

$$\mathbf{J} = -D\nabla C(x, y, z, t), \tag{4.4}$$

In a three-dimensional Cartesian coordinate system (3D), the concentration gradient $\nabla C(x, y, z, t)$ is written as

$$\nabla C(x, y, z, t) = \frac{\partial C(x, y, z, t)}{\partial x}\mathbf{i} + \frac{\partial C(x, y, z, t)}{\partial y}\mathbf{j} + \frac{\partial C(x, y, z, t)}{\partial z}\mathbf{k}$$

where $\mathbf{J}$, D, $C(x, y, z, t)$ are the diffusion flux vector, the diffusion coefficient (diffusivity), and the atomic concentration, respectively; $\mathbf{i}$, $\mathbf{j}$ and $\mathbf{k}$ are standard unit vectors.

For one-dimensional diffusion (1D), Fick's first law reduces to

$$J = -D\frac{\partial C(x, t)}{\partial x} \tag{4.5}$$

where J is the magnitude of diffusion flux (atoms/m^2·s).

One can see from Fick's first law that the flux of atoms is proportional to the concentration

gradient. Diffusion is faster in a region of larger concentration gradient than in another region with smaller concentration gradient. In a finite volume of material, the local concentration of atoms changes in time. Indeed, if the flux $J_1 = J(x)$ is assumed to enter a section of a material and to leave the same section with the flux $J_2 = J(x + dx)$ as depicted in Fig. 4.27,

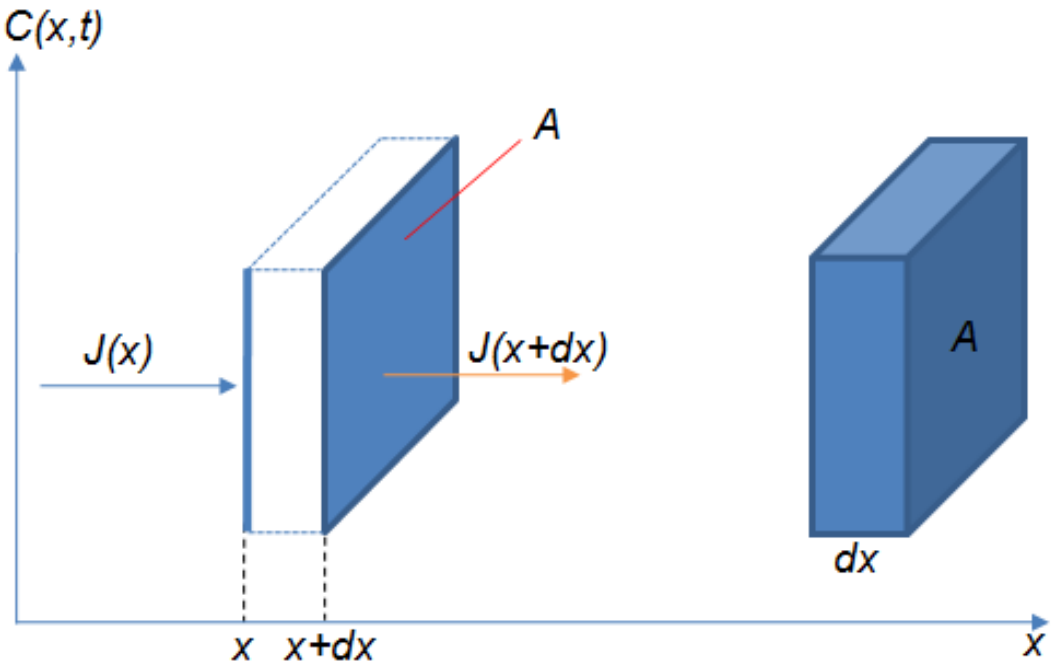

Fig. 4.27: Schematic diagram of the local concentration and diffusion flux through a unit area (A) at position x.

We have

$$dC(x,t) = \frac{(J_1 - J_2)\, dtA}{Adx} = \frac{[J(x) - J(x+dx)]\, dtA}{Adx} \tag{4.6}$$

with $J(x + dx) = J(x) + \frac{\partial J}{\partial x} dx$

Then, we obtain

$$\frac{\partial C(x,t)}{\partial t} = -\frac{\partial J}{\partial x} \tag{4.7}$$

Combining (4.5) and (4.7), we have Fick's second law as follows

$$\frac{\partial C(x,t)}{\partial t} = D\frac{\partial^2 C(x,t)}{\partial x^2} \tag{4.8}$$

Considering the boundary condition given by

$$\begin{cases} C(x=0, t>0) = C_s, \\ C(x=\infty, t>0) = C_0, \end{cases}$$

Then, the solution is obtained as [183]

$$C_x = C_s - (C_s - C_0)\,\mathrm{erf}\left(\frac{x}{2\sqrt{Dt}}\right) \tag{4.9}$$

c. Diffusion coefficient

In physics, diffusion coefficient D is the most important parameter in a diffusive system which is often described as a thermally activated effect as plotted in Fig. 4.28 (a) according to Arrhenius equation by

$$D = D_0 e^{-\frac{E_a}{k_B T}}, \tag{4.10}$$

where

- D is the diffusion coefficient (m^2/s),
- D_0 is a temperature-independent pre-exponential constant (m^2/s) which depends on the following factors [184, 185]
  - The type of diffusion: *whether the diffusion is interstitial or substitutional*;
  - The type of crystal structure: *diffusion in hexagonal crystal structure is slower than the one in BCC/FCC crystal structure*;
  - The type of crystal imperfection: *more grain boundaries will increase diffusion (diffusion is faster in polycrystalline than single crystal materials)*;
- E_a is the activation energy for diffusion (eV/atom),
- k_B is Boltzmann constant (8.62×10^{-5} eV/atom.K),
- T is the absolute temperature (K).

In practice, the above equation is often rewritten as

$$lnD = lnD_0 - \left(\frac{E_a}{k_B}\right)\frac{1}{T} \tag{4.11}$$

Therefore, Arrhenius equation can be illustrated by plotting lnD versus $1/T$ in Fig. 4.28 (b).

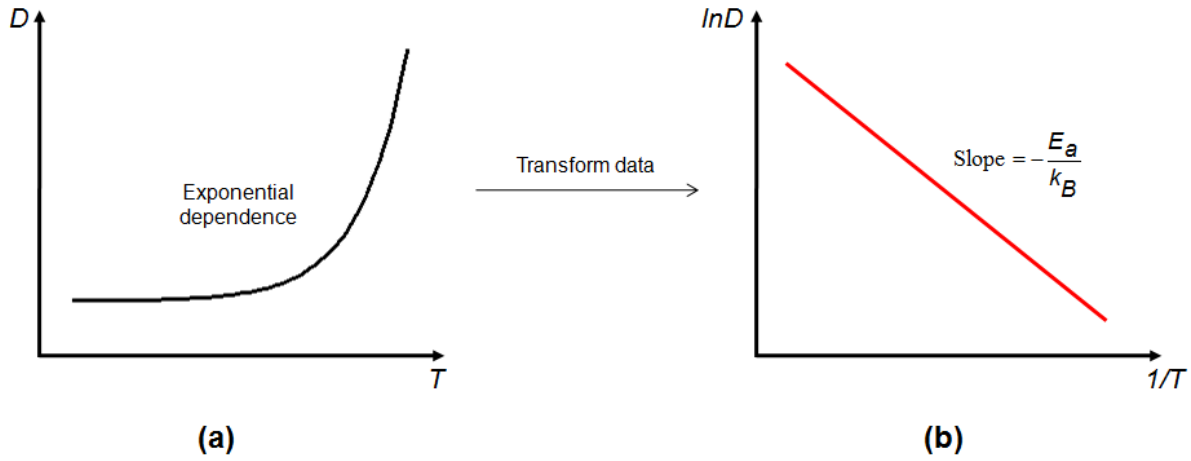

Fig. 4.28: (a) Dependence of the diffusion coefficient D on the growth temperature T from equation (4.10) and (b) data is transformed in lnD vs. $1/T$.

For the case of graphene formation on $3C$-SiC/Si(111) in the range of substrate temperatures from 900 - 1100 °C, the diffusion coefficient of Si is expected to increase at elevated substrate temperatures. Our experimental observation during carbon deposition on top of SiC buffer layers is consistent with earlier studies in this context. Indeed, different groups as Refs. [186, 187] indicated that the Si diffusion across the SiC film exhibits Arrhenius behavior as Fig. 4.28 (b).

d. Silicon diffusion through $3C$-SiC buffer

We will now consider the specific case of Si diffusion through $3C$-SiC grown on Si(111) as illustrated in Fig. 4.29.

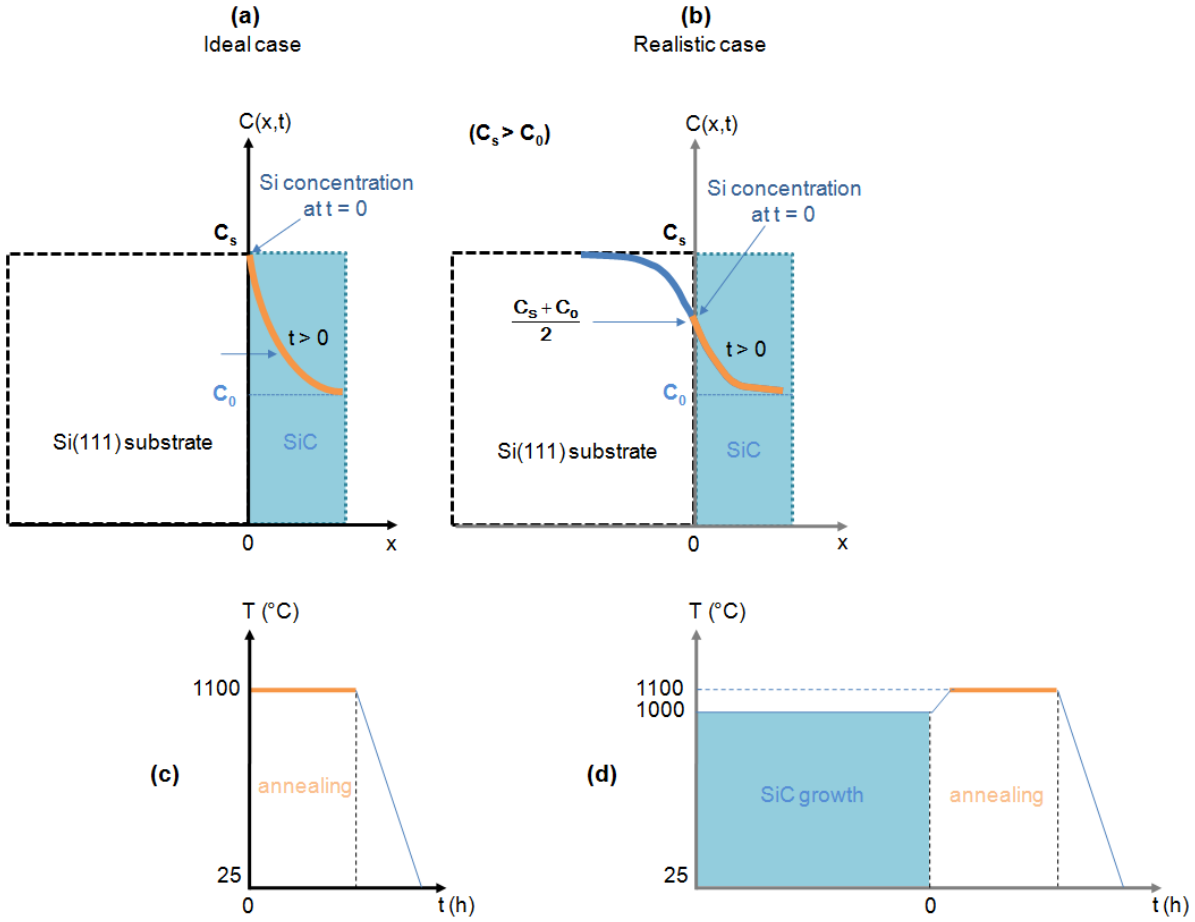

Fig. 4.29: Schematic diagram of interface between Si(111) substrate and $3C$-SiC buffer layer. (a) Assuming that the sample with an abrupt interface (ideal case) is heated immediately at 1100 °C and (c) is described in T vs. t; (b, d) after SiC growth on Si(111) at 1000 °C (realistic case), followed by slow annealing up to 1100 °C for 2 hours as illustrated by orange solid line in T vs. t.

Si atoms also diffuse from Si bulk into SiC layers not only during annealing but also during the $3C$-SiC growth on the Si(111) substrate. Diffusion becomes faster when the annealing temperature is increased. The interface between two materials (SiC and Si) after annealing is not like the ideal case (Fig. 4.29 (a)). It should be considered as Fig. 4.29 (b).

In this case, the boundary condition must be adjusted as

$$\begin{cases} C(x=0, t>0) = \frac{C_s+C_0}{2}, \\ C(x=\infty, t>0) = C_0, \end{cases}$$

Therefore, the solution of Fick's second law will be

$$C_x = \frac{C_s + C_0}{2} - \frac{C_s - C_0}{2}\mathrm{erf}\left(\frac{x}{2\sqrt{Dt}}\right) \tag{4.12}$$

Fig. 4.30 shows LEED patterns of SiC film on Si(111) and after annealing at $\sim$ 1100 °C

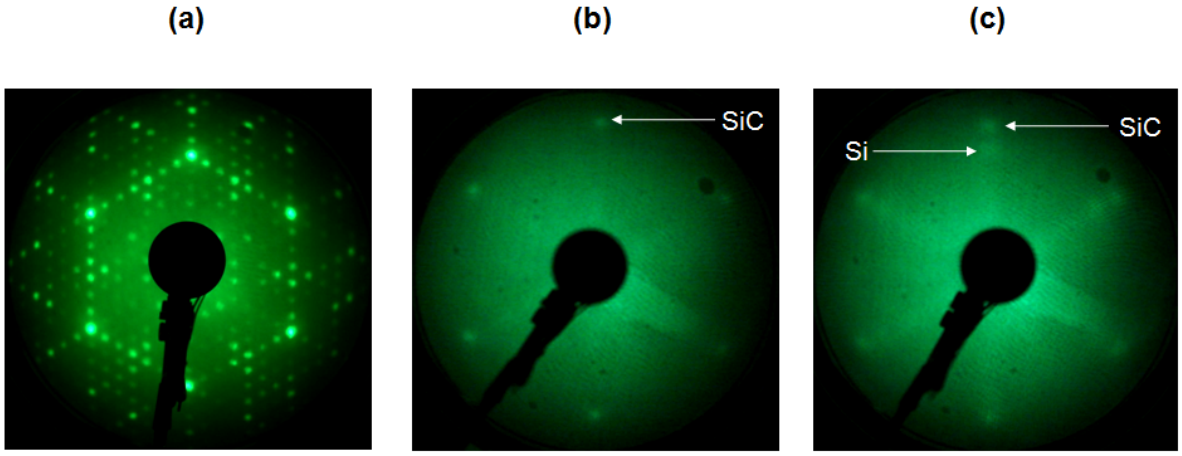

Fig. 4.30: LEED patterns at 57 eV of the Si(111) substrate (a), after $\sim$ 19-nm-thick $3C$-SiC on Si(111) (b) and after 2 hours annealing at 1100 °C (c).

Besides SiC spots, some inner spots could still be observed. Position of these diffraction spots is almost the same as position of (1×1) Si spots from the silicon substrate. It is probably caused by diffusion of Si atoms from the substrate during the annealing.

In order to determine the atomic concentration of Si (C_{Si}), XPS depth profiles were measured on $3C$-SiC/Si(111) by alternating sputtering with Ar^+ ions (the sputter rate $\sim$ 0.02 nm/s at 3 keV) and XPS measurements. First, we measured depth profile on a $\sim$ 19-nm-thick $3C$-SiC/Si(111) sample to determine the initial concentration of Si atoms (C_0) in the SiC buffer. The results are shown in Fig. 4.31 (a). Experimental details

in growing $3C$-SiC on Si(111) are mentioned in section 4.3.1. Next, the sample was annealed at 1100 °C for 2 hours (Fig. 4.31 (b)) and another depth profile was measured on the same sample sufficiently far away from the region where the first profile was measured.

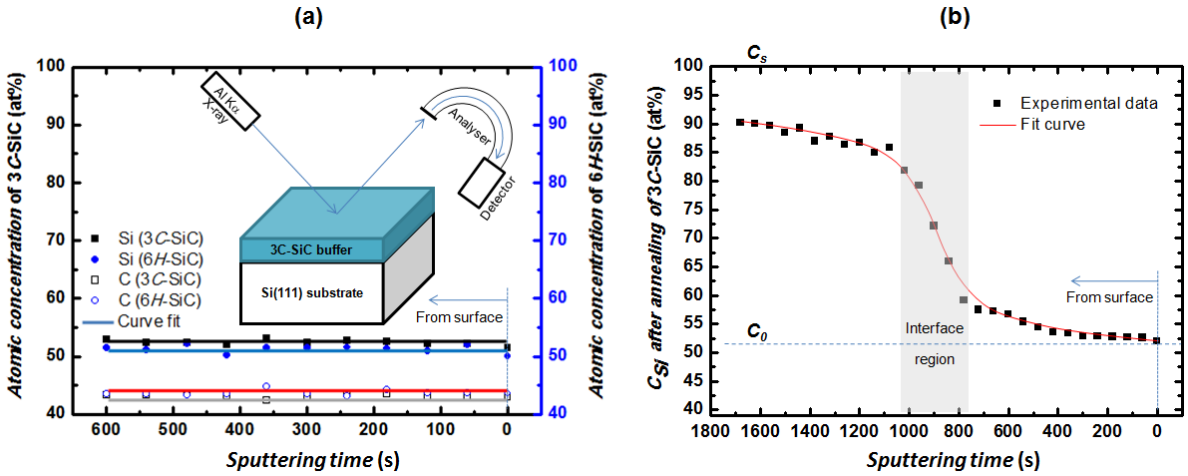

Fig. 4.31: (a) XPS depth profile of concentration of Si atoms C_{Si} in SiC buffer layers vs. sputtering time, measured before annealing ($C_0 \sim 52.0\%$ Si and $\sim 43.0\%$ C); (b) Concentration of Si atoms C_{Si} vs. sputtering time from the sample surface after annealing a $\sim$ 19-nm-thick 3C-SiC on Si(111) at 1100 °C.

The concentration of Si and C atoms in $3C$-SiC is nearly constant at $\sim 52.0\%$ Si and 43.0% C ($\sim$ 5% O + Ar) and values are close to those obtained on pure Si-face $6H$-SiC ($\sim 51.0\%$ Si and 44.0% C). After annealing, the concentration of Si atoms was found to increase slightly (Fig. 4.31 (b)). This is due to Si out-diffusion from the substrate during annealing. Fig. 4.32 shows a comparison between the measured C_{Si} concentration in SiC with the calculation based on equation (4.12) where the diffusion coefficient was adjusted to obtain the best fit.

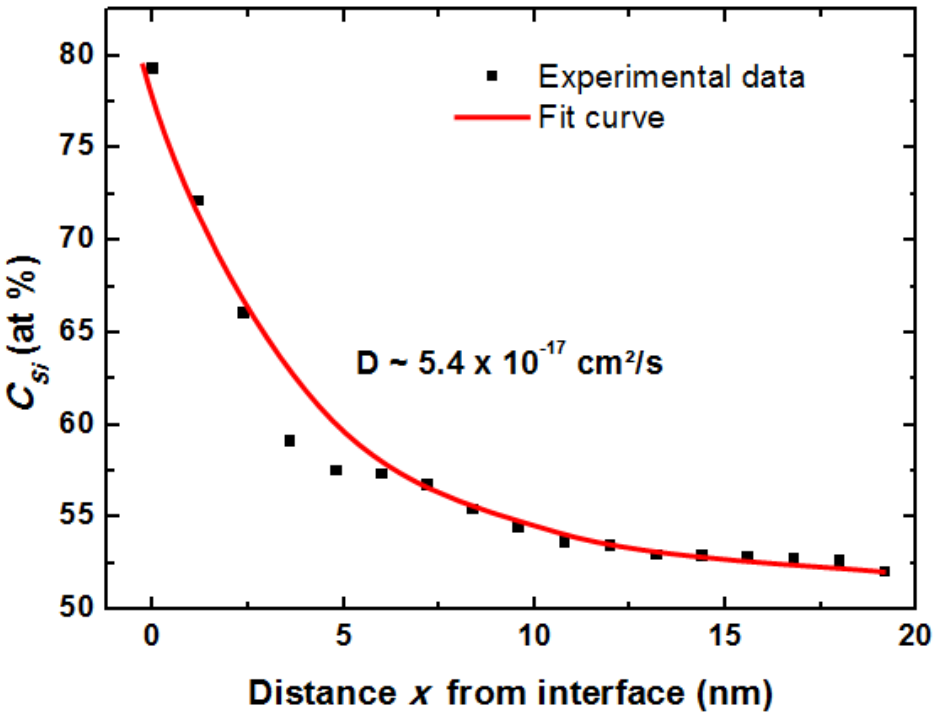

Fig. 4.32: Fit of equation (4.12) to measured Si concentration profile for determining the diffusion coefficient D of Si.

From this fit, the diffusion coefficient of Si atoms through SiC buffer layer at 1100 °C was found to be $\sim 5.4 \times 10^{-17}$ cm^2/s. This value is larger than the one of $\sim 4 \times 10^{-18}$ cm^2/s reported by Ollivier et al. [188] for Si diffusion through $\sim$ 3-nm-thick $3C$-SiC crystalline film on Si(100) for the same substrate temperature. This may be explained by the difference in the crystalline quality of SiC layers on the silicon substrate and would imply that the $3C$-SiC buffer on Si(111) in our work contains more grain boundaries and other defects such as pits and voids [180, 186, 189]. Now, the flux of diffusing Si atoms can be calculated by rewriting Eq. (4.5) as

$$J = D_{Si}\frac{C_s - C_0}{2\sqrt{\pi D_{Si}t}}e^{-\frac{x^2}{4D_{Si}t}}, \tag{4.13}$$

together with atomic percentage of silicon (with respect to a carbon flux of 1.2×10^{13} atoms/cm$^2\cdot$ s.) at different thicknesses of SiC buffer layer. Results are summarized in Table 4.7.

x (nm)	4	7	13	25	30	35
J (atoms/cm$^2\cdot$ s)	4.4×10^{10}	3.6×10^{10}	1.7×10^{10}	8.8×10^{8}	2.0×10^{8}	1.85×10^{7}
at. Si(%)	0.37	0.3	0.14	0.007	0.0013	1.5e-4

Table 4.7: The flux and atomic percentage of diffusing Si across different thicknesses of SiC buffer layer after 2 hours of annealing at 1100 °C using $C_s \sim 5.0 \times 10^{22}$ atoms/cm^3 in the bulk Si(111) and $C_0 \sim 4.8 \times 10^{22}$ atoms/cm^3 in $3C$-SiC. Atomic percentage of Si is calculated with respect to the flux of deposited carbon $\sim 1.2 \times 10^{13}$ atoms/cm$^2\cdot$ s.

It is found that a Si flux is always present during carbon growth due to Si-out diffusion from the substrate through SiC buffer at high temperature. This may induce an increase of the SiC buffer thickness. The atomic percentage of Si atoms in the total flux decreases as the distance x from interface increases.

Now, let's consider sample #7 in model 4 as described in Fig. 4.21 (b). We grew $\sim$ 24 nm thick $3C$-SiC/Si(111), followed by slow heating up to $\sim$ 1200 °C in order to flatten the carbide surface. During annealing at this substrate temperature, diffusion of Si from the bulk to SiC layers could be faster before decreasing to 1100 °C for carbon deposition. As indicated earlier by XPS analyses for this sample, $\sim$ 8 graphene layers ($\sim$ 2.7 nm) were formed on top of the SiC buffer after 2 hours of carbon deposition, followed by 30 min for post annealing. We calculated the carbide thickness below graphene layers to increase about $\sim$ 6 nm [12] by the interaction of extra silicon atoms with the deposited carbon atoms due to out-diffusion of Si from the substrate. Therefore, the thickness of SiC buffer layer was estimated about $\sim$ 30 nm in total, which should be sufficient for blocking Si diffusion at the given growth time (Si:C flux ratio close to 10^{-5}). This explains why the quality of graphene on sample #7 is better than that on sample #4.

4.4. Summary

For growing graphene on Si(111) by direct deposition of solid-state carbon atoms, the

[12] 2h $\rightarrow \sim$ 24 ML carbon
XPS $\rightarrow \sim$ 8 ML graphene
$\Rightarrow$ 16 ML react with Si $\rightarrow$ SiC
16 ML = $16 \times 1.9 \times 10^{15}$ atoms/cm^2; 1 ML SiC = 1.2×10^{15} atoms/cm^2
$\Rightarrow$ 25 ML SiC = $\sim$ 6.4 nm

substrate temperature and the thickness of the buffer layer always play an important role. High substrate temperature can help to reduce the film surface roughness, but is harmful to the quality of graphene due to Si out-diffusion from the substrate and intermixing with deposited carbon at the surface. Therefore, a sufficiently thick buffer layer is necessary to prevent out-diffusion of Si during growth. The minimum SiC thickness depends on substrate temperature during C growth; in our case (C growth at 1100 °C), $\sim$ 30 nm seems to be adequate value.

Chapter 5
CONCLUSION

5.1. Summary of the results

Direct growth of graphene on Si(111) 7×7 surfaces was demonstrated using electron beam evaporation. By preforming a buffer on Si(111), various structural models were proposed to explain the different crystalline qualities of graphene. The growth time, substrate temperature and thickness of a buffer layer are considered as the main factors affecting the structural and electronic properties of our materials. In this thesis, we studied aspects as summarized in the following points,

First, we investigate the influence of *a*-C buffer thickness on the formation of graphitic carbon films on Si(111).

We succeeded in growing graphitic layers directly on Si(111) through the deposition of an *a*-C buffer layer at room temperature. The important role of the *a*-C buffer layer was indicated in the growth of graphitic carbon. Therefore, different samples with various thicknesses of the *a*-C buffer (1 ML, 1.5 ML, 3 ML and 4 ML) were produced. The properties of carbon films were found similar to silicon carbide if the buffer thickness is less than 1.5 ML and vice versus, graphitic carbon similar to HOPG was formed in the case of thicker buffers. This *a*-C layer acts as a barrier to avert the formation of SiC precipitates as long as temperature is sufficiently low. The *a*-C layer effectively stabilizes the Si surface affording an increase in the substrate temperature up to 820 °C without allowing Si to intermix with the deposited carbon at the surface. Experimental evidence shows that a transformation from *a*-C to SiC occurs during annealing. XPS measurement marked a transition from Si-C bonds to sp^2-bonded carbons with increasing *a*-C buffer thickness and Raman data confirmed the existence of the stacking order in graphitic layers. The 1.5 ML sample is considered as the transition between SiC and graphitic carbon. Therefore, in order to grow graphitic carbon on Si(111), the minimum thickness

of the a-C buffer layer should be around 3 ML.

Second, we studied influence of deposition time on the quality of graphene formation using a coverage of a few a-C buffer layers deposited at room temperature on $3C$-SiC layers on Si(111).

Graphitic carbon films on Si(111) were improved by first growing a few layers of SiC on Si(111) instead of growing the a-C directly. Such a SiC buffer layer can be helpful to stabilize the surface of Si substrate. In order to evaluate the role of the a-C layer, the samples were exposed at room temperature for a few minutes to a flux of carbon atoms ($\sim$ 4 ML) before slow heating to the substrate temperature of 1000 °C. Graphene was found with different qualities depending on the time of carbon deposition. Despite a high surface roughness and very large number of defects, atomic resolution STM images showed evidence of Bernal stacking order of a typical graphene lattice with a small domain size ($\leq$ 80 Å).

Third, we checked influence of the growth time on the quality of graphene on Si(111) by direct deposition of carbon atoms at 1000 °C.

Carbon atoms were directly deposited on $3C$-SiC/Si(111) at a substrate temperature of 1000 °C. Without the a-C layer (model 2) that can prevent diffusion of Si atoms from the substrate, model 3 requires longer deposition of carbon atoms for obtaining graphene at the same substrate temperature. Indeed, graphene could be formed after $\sim$ 5 hours of carbon deposition on top of a-C layer while it needs $\sim$ 7 hours for a carbon coverage on top of $3C$-SiC. For this case, the SiC buffer layer could act as a template for graphene formation. The results confirm the influence of growth time on the quality of graphene. Although the crystallite size of graphene is improved with a domain size of 9 - 12 nm, the film is quite rough with the formation of islands on the surface.

Fourth, we investigated the effect of the substrate temperature and of the SiC buffer thickness on the graphene formation on Si(111).

To be compatible with conventional Si-based industry, reduction of the growth temperature is still preferable. So, the effects of substrate temperature were only investigated in the range of 900 - 1100 °C and the influence of different thicknesses of SiC buffer layer on the structural quality and electronic properties of our graphene was studied at the optimal temperature. Due to the need for very high temperature annealing ($\sim$ 1200 °C) in order to flatten the surface, thicker SiC buffer layer (template for graphene

formation) was produced compared to that of model 3 to prevent the out-diffusion of Si at high temperature. Although the surface roughness is significantly improved, graphene films still contain many defects together with some random SiC islands on the surface due to out-diffusion of silicon atoms from the substrate. It shows that the formation of sp^2 bonded carbon evolves as a function of the growth temperature. Higher substrate temperature causes transformation of graphitic carbon to carbide. Therefore, a sufficiently thick SiC buffer layer is necessary to prevent additional Si-C bonding near or on the surface during carbon deposition. Indeed, we observed an improvement of the structural quality of the graphene layer when increasing the thickness of SiC buffer layer and an increase in number of graphene layers as confirmed by XPS at the same substrate temperature of 1100 °C. STM images confirm the improvement of structural quality, surface roughness as well as the size of our graphene domain although a high defect density is still shown by the presence of a D band on Raman spectra of such films.

In order to support our conclusions about the influence of the substrate temperature and SiC buffer thickness, a calculation of the silicon diffusion profile through the SiC buffer layer during carbon growth was presented. Experimental results confirmed that graphene ($\sim$ 8 layers) was grown after 2 hours of carbon deposition on top of $\sim$ 24-nm-thick SiC buffer at 1100 °C, followed by 30 min of post annealing. We estimate that an additional $\sim$ 6 nm of SiC was formed during carbon deposition before blocking Si out-diffusion from the substrate with the total SiC thickness $\sim$ 30 nm. According to our calculation of Si diffusion in SiC, this should be enough to avoid degradation of the quality of graphene films on Si(111) at 1100 °C. Experimentally, we observed indeed that sample with thinner SiC buffer layer exhibits inferior quality of graphene layer. From this work, we understand the reason why the growth of high-quality graphene on Si wafer remains challenging.

5.2. Perspectives

Although graphene on Si(111) wafer was achieved by electron beam evaporation, some improvements are still needed.

First, the high defect density and small size of graphene domains is related to out-diffusion of Si atoms at high temperature. Therefore, a thicker SiC buffer layer should

be tested with higher deposition rate of both carbon and silicon atoms. It may help to block Si atoms from the substrate during carbon and silicon deposition.

Second, the diffusion coefficient of Si through SiC buffer layers was found to be larger compared with some values reported in literature; this probably leads to higher defect densities in the graphene layers. Therefore, the crystalline quality of $3C$-SiC epitaxial films on Si(111) needs to be improved before graphene formation.

Bibliography

[1] A. Timoshevskii, S. Kotrechko, and Yu. Matviychuk. Atomic structure and mechanical properties of carbyne. *Phys. Rev. B*, 91:245434, Jun 2015. doi: 10.1103/PhysRevB.91.245434. URL http://link.aps.org/doi/10.1103/PhysRevB.91.245434. 1

[2] A. K. Nair, S. W. Cranford, and M. J. Buehler. The minimal nanowire: Mechanical properties of carbyne. *EPL (Europhysics Letters)*, 95(1):16002, 2011. URL http://stacks.iop.org/0295-5075/95/i=1/a=16002. 1

[3] H.W Kroto, J. R Heath, S. C. Obrien, R. F Curl, and R. E Smalley. C60 buckminsterfullerene. *Nature*, 318:162–163, 1985. 1

[4] SUMIO Iijima. Helical microtubules of graphitic carbon. *Nature*, 354:56–58, 1991. 1

[5] A. K. Geim and K. S. Novoselov. The rise of graphene. *Nature Materials*, 6: 183–191, March 2007. doi: 10.1038/nmat1849. xii, 1, 2

[6] Randall Feenstra. Semiconductor surfaces and interfaces: Epitaxial graphene on sic. http://www.andrew.cmu.edu/user/feenstra/graphene/, Access: 2015. xii, 1

[7] K.S. Novoselov, A. K. Geim, S.V. Morozov, D. Jiang, Y. Zhang, S. V. Dubonos, I. V. Grigorieva, and Firsov A. A. Electric field effect in atomically thin carbon films. *Science*, 306:666, 666-669 2004. 2, 3, 55, 62

[8] Electrical properties of silicon. http://www.keysight.com/upload/cmc_upload/All/EE_REF_PROPERTIES_Si_Ga.pdf?&cc=BE&lc=dut, 2015. 2

[9] He Peimo, Xu Yabo, Zhang Xuejia, Zhen Xinbin, and Li Wenzhou. Electrical conductivity studies of a pure c 60 single crystal. *Journal of Physics: Condensed Matter*, 5(37):7013, 1993. URL http://stacks.iop.org/0953-8984/5/i=37/a=019. 2

[10] L. McEuen Paul, S. Fuhrer Michael, and Park Hongkun. Single-walled carbon nanotube electronics. *IEEE Transactions on Nanotechnology*, 1:78–85, 2002. 2

[11] A. Bachtold, M. Henny, C. Terrier, C. Strunk, C. Schönenberger, J.-P. Salvetat, J.-M. Bonard, and L. Forró. Contacting carbon nanotubes selectively with low-ohmic contacts for four-probe electric measurements. *Applied Physics Letters*, 73(2): 274–276, 1998. doi: http://dx.doi.org/10.1063/1.121778. URL http://scitation.aip.org/content/aip/journal/apl/73/2/10.1063/1.121778. 2

[12] Zhiming Wang, Feng Xu, Chao Lu, He Zhang, Qingyu Xu, and Jinan Zhu. Electronic conductivity upturn of hopg contrast to transport properties of polycrystal graphite. *arXiv:0801.3298v1*, page 11, 2008. 2

[13] L. Pietronero, S. Strässler, H. R. Zeller, and M. J. Rice. Electrical conductivity of a graphite layer. *Phys. Rev. B*, 22:904–910, Jul 1980. doi: 10.1103/PhysRevB.22.904. URL http://link.aps.org/doi/10.1103/PhysRevB.22.904. 2

[14] C. J. Glassbrenner and Glen A. Slack. Thermal conductivity of silicon and germanium from 3°k to the melting point. *Phys. Rev.*, 134:A1058–A1069, May 1964. doi: 10.1103/PhysRev.134.A1058. URL http://link.aps.org/doi/10.1103/PhysRev.134.A1058. 2

[15] R. C. Yu, N. Tea, M. B. Salamon, D. Lorents, and R. Malhotra. Thermal conductivity of single crystal c_{60}. *Phys. Rev. Lett.*, 68:2050–2053, Mar 1992. doi: 10.1103/PhysRevLett.68.2050. URL http://link.aps.org/doi/10.1103/PhysRevLett.68.2050. 2

[16] Sinha Saion, Barjami Saimir, Iannacchione Germano, Schwab Alexander, and Muench George. Off-axis thermal properties of carbon nanotube films. *Journal of Nanoparticle Research*, 7:651–657, 2005. 2

[17] P. Kim, L. Shi, A. Majumdar, and P. L. McEuen. Thermal transport measurements of individual multiwalled nanotubes. *Phys. Rev. Lett.*, 87:215502, Oct 2001. doi: 10.1103/PhysRevLett.87.215502. URL http://link.aps.org/doi/10.1103/PhysRevLett.87.215502. 2

[18] H. Fukushima, L. T. Drzal, B. P. Rook, and D. J. Rich. Thermal conductivity of exfoliated graphite nanocomposites. *Journal of Thermal Analysis and Calorimetry*, 85:235–238, 2006. 2

[19] D. T. Morelli and C. Uher. Thermal conductivity and thermopower of graphite at very low temperatures. *Phys. Rev. B*, 31:6721–6725, May 1985. doi: 10.1103/PhysRevB.31.6721. URL http://link.aps.org/doi/10.1103/PhysRevB.31.6721. 2

[20] Alexander A. Balandin, Suchismita Ghosh, Wenzhong Bao, Irene Calizo, Desalegne Teweldebrhan, Feng Miao, and Chun Ning Lau. Superior thermal conductivity of single-layer graphene. *Nano Letters*, 8(3):902–907, Feb 2008. 2

[21] R. R Nair, P. Blake, A. N. Grigorenko, K.S. Novoselov, T. J. Booth, T. Stauber, N. M. R. Peres, and A. K. Geim. Fine structure constant defines visual transparency of graphene. *Science*, 320:1308, 2008. 2

[22] Ioffe Institute. Si-silicon. http://www.ioffe.rssi.ru/SVA/NSM/Semicond/Si/electric.html, 2015. 2

[23] S. Kobayashi, T. Takenobu, S. Mori, A. Fujiwara, and Y. Iwasa. Fabrication and characterization of c60 thin-film transistors with high field-effect mobility. *Applied Physics Letters*, 82(25):4581–4583, 2003. doi: http://dx.doi.org/10.1063/1.1577383. URL http://scitation.aip.org/content/aip/journal/apl/82/25/10.1063/1.1577383. 2

[24] T. Durkop, S. A. Getty, Enrique Cobas, and M. S. Fuhrer. Extraordinary mobility in semiconducting carbon nanotubes. *Nano Letters*, 4(1):35–39, 2004. doi: 10.1021/nl034841q. URL http://dx.doi.org/10.1021/nl034841q. 2

[25] N Garcia, P. Esquinazi, J. Barzola-Quiquia, B. Ming, and D. Spoddig. Transition from ohmic to ballistic transport in oriented graphite: Measurements and numerical simulations. *Phys. Rev. B*, 78:035413, Jul 2008. doi: 10.1103/PhysRevB.78.035413. URL http://link.aps.org/doi/10.1103/PhysRevB.78.035413. 2

[26] K.S. Novoselov, A. K. Geim, S.V. Morozov, D. Jiang, I. V. Katsnelson, I. V. Grigorieva, S. V. Dubonos, and Firsov A. A. Two-dimensional gas of massless dirac fermions in graphene. *Nature*, 438:197–200, 2005. 2

[27] E. Pallecchi, F. Lafont, V. Cavaliere, F. Schopfer, D. Mailly, W. Poirier, and A. Ouerghi. High electron mobility in epitaxial graphene on 4h-sic(0001) via post growth annealing under hydrogen. *Scientific Reports*, 4(4558), 2014. 2

[28] K.I. Bolotin, K.J. Sikes, Z. Jiang, M. Klima, G. Fudenberg, J. Hone, P. Kim, and H.L. Stormer. Ultrahigh electron mobility in suspended graphene. *Solid*

State Communications, 146:351 – 355, 2008. ISSN 0038-1098. doi: http://dx.doi.org/10.1016/j.ssc.2008.02.024. URL http://www.sciencedirect.com/science/article/pii/S0038109808001178. 2

[29] Changgu Lee, Xiaoding Wei, Jeffrey W. Kysar, and James Hone. Measurement of elastic properties and intrinsic strength of monolayer graphene. *Science*, 321: 385–388, 2008. 2

[30] K. I. Bolotin, K. J. Sikes, J. Hone, H. L. Stormer, and P. Kim. Temperature-dependent transport in suspended graphene. *Phys. Rev. Lett.*, 101:096802, Aug 2008. doi: 10.1103/PhysRevLett.101.096802. URL http://link.aps.org/doi/10.1103/PhysRevLett.101.096802. 2

[31] FRANK Schwierz. Graphene transistors. *Nanotechnology*, 5:487–496, 2010. 2

[32] Xuan Wang, Linjie Zhi, and Klaus Mullen. Transparent, conductive graphene electrodes for dye-sensitized solar cells. *Nano Letters*, 8(1):323–327, 2008. PMID: 18069877. 2

[33] Junbo Wu, Mukul Agrawal, Hector A. Becerril, Zhenan Bao, Zunfeng Liu, Yongsheng Chen, and Peter Peumans. Organic light-emitting diodes on solution-processed graphene transparent electrodes. *ACS Nano*, 4(1):43–48, 2010. doi: 10.1021/nn900728d. URL http://dx.doi.org/10.1021/nn900728d. PMID: 19902961. 2

[34] F. Bonaccorso, Z. Sun, T. Hasan, and A. C. Ferrari. Graphene photonics and optoelectronics. *Nature Photonics*, 4:611–622, 2010. 2

[35] F. Schedin, A. K. Geim, S. V. Morozov, E. W. Hill, P. Blake, M. I. Katsnelson, and K. S. Novoselov. Detection of individual gas molecules adsorbed on graphene. *Nature Materials*, 6:652–655, 2007. 2

[36] Andre Geim and Konstantin Novoselov. The nobel prize in physics 2010. *Nobel prizes and Laureates*, 2010. 3

[37] Yihong Wu, Zexiang Shen, and Ting Yu, editors. *Two-Dimensional Carbon: Fundamental Properties, Synthesis, Characterization and applications*. CRC Press, 2014. 3

[38] Ayrat M. Dimiev and James M. Tour. Mechanism of graphene oxide formation. *ACS Nano*, 8(3):3060–3068, 2014. doi: 10.1021/nn500606a. URL http://dx.doi.org/10.1021/nn500606a. PMID: 24568241. 3

[39] Dmitriy A. Dikin, Sasha Stankovich, Eric J. Zimney, Richard D. Piner, Geoffrey H. B. Dommett, Guennadi Evmenenko, SonBinh T. Nguyen, and Rodney S. Ruoff. Preparation and characterization of graphene oxide paper. *Nature*, 448:457–460, 2007. 3

[40] William S. Hummers and Richard E. Offeman. Preparation of graphitic oxide. *Journal of the American Chemical Society*, 80(6):1339–1339, 1958. doi: 10.1021/ja01539a017. URL http://dx.doi.org/10.1021/ja01539a017. 3

[41] Jianxin Geng, Byung-Seon Kong, Seung Bo Yang, and Hee-Tae Jung. Preparation of graphene relying on porphyrin exfoliation of graphite. *Chem. Commun.*, 46: 5091–5093, 2010. URL http://dx.doi.org/10.1039/C001609H. 4

[42] Wang Hailiang, Wang Xinran, Li Xiaolin, and Dai Hongjie. Chemical self assembly of graphene sheets. *cond-mat.mtrl-sci*, arXiv:0902.3703:1 – 15, 2009. 4

[43] Ching-Yuan Su, Ang-Yu Lu, Yanping Xu, Fu-Rong Chen, Andrei N. Khlobystov, and Lain-Jong Li. High-quality thin graphene films from fast electrochemical exfoliation. *ACS Nano*, 5(3):2332–2339, 2011. doi: 10.1021/nn200025p. URL http://dx.doi.org/10.1021/nn200025p. PMID: 21309565. 4

[44] Ayrat M. Dimiev, Gabriel Ceriotti, Natnael Behabtu, Dante Zakhidov, Matteo Pasquali, Riichiro Saito, and James M. Tour. Direct real-time monitoring of stage transitions in graphite intercalation compounds. *ACS Nano*, 7(3):2773–2780, 2013. doi: 10.1021/nn400207e. URL http://dx.doi.org/10.1021/nn400207e. PMID: 23438444. 4

[45] K.S. Novoselov, V. I. Fal'ko, L. Colombo, P. R. Gellert, M. G. Schwab, and K. Kim. A roadmap for graphene. *Nature*, 490:192–200, 2012. xii, 4

[46] Songfeng Pei and Hui-Ming Cheng. The reduction of graphene oxide. *Carbon*, 50(9):3210 – 3228, 2012. ISSN 0008-6223. doi: http://dx.doi.org/10.1016/j.carbon.2011.11.010. URL http://www.sciencedirect.com/science/article/pii/S0008622311008967. Festschrift dedicated to Peter A. Thrower, Editor-in-Chief, 1972 - 2012. 5

[47] Florian Banhart, Jani Kotakoski, and Arkady V. Krasheninnikov. Structural defects in graphene. *ACS Nano*, 5(1):26–41, 2011. doi: 10.1021/nn102598m. URL http://dx.doi.org/10.1021/nn102598m. PMID: 21090760. 5

[48] J. Wintterlin and M.-L. Bocquet. Graphene on metal surfaces. *Surface Science*, 603:1841 – 1852, 2009. ISSN 0039-6028. doi: http://dx.doi.org/10.1016/j.susc.2008.08.037. URL http://www.sciencedirect.com/science/article/pii/S003960280900079X. Special Issue of Surface Science dedicated to Prof. Dr. Dr. h.c. mult. Gerhard Ertl, Nobel-Laureate in Chemistry 2007. 5

[49] Wei Liu, Choong-Heui Chung, Cong-Qin Miao, Yan-Jie Wang, Bi-Yun Li, Ling-Yan Ruan, Ketan Patel, Young-Ju Park, Jason Woo, and Ya-Hong Xie. Chemical vapor deposition of large area few layer graphene on si catalyzed with nickel films. *Thin Solid Films*, 518(6, Supplement 1):S128 – S132, 2010. ISSN 0040-6090. doi: http://dx.doi.org/10.1016/j.tsf.2009.10.070. URL http://www.sciencedirect.com/science/article/pii/S0040609009017131. Sixth International Conference on Silicon Epitaxy and Heterostructures. 5, 9

[50] Hye Jin Park, Jannik Meyer, Siegmar Roth, and Viera Skakalova. Growth and properties of few-layer graphene prepared by chemical vapor deposition. *Carbon*, 48(4):1088 – 1094, 2010. ISSN 0008-6223. doi: http://dx.doi.org/10.1016/j.carbon.2009.11.030. URL http://www.sciencedirect.com/science/article/pii/S0008622309007659. xv, 5, 9, 61

[51] Xuesong Li, Weiwei Cai, Jinho An, Seyoung Kim, Junghyo Nah, Dongxing Yang, Richard Piner, Aruna Velamakanni, Inhwa Jung, Emanuel Tutuc, Sanjay K. Banerjee, Luigi Colombo, and Rodney S. Ruoff. Large-area synthesis of high-quality and uniform graphene films on copper foils. *Science*, 324(5932):1312–1314, 2009. doi: 10.1126/science.1171245. 5

[52] Walt A. de Heer, Claire Berger, Xiaosong Wu, Phillip N. First, Edward H. Conrad, Xuebin Li, Tianbo Li, Michael Sprinkle, Joanna Hass, Marcin L. Sadowski, Marek Potemski, and Garard Martinez. Epitaxial graphene. *Solid State Communications*, 143:92 – 100, 2007. ISSN 0038-1098. doi: http://dx.doi.org/10.1016/j.ssc.2007.04.023. URL http://www.sciencedirect.com/science/article/pii/S0038109807002980. Exploring graphene Recent research advances. 5, 55

[53] J Hass, W A de Heer, and E H Conrad. The growth and morphology of epitaxial multilayer graphene. *Journal of Physics: Condensed Matter*, 20(32):323202, 2008. URL http://stacks.iop.org/0953-8984/20/i=32/a=323202. 5, 53, 73, 79

[54] J. Hackley, D. Ali, J. DiPasquale, J. D. Demaree, and C. J. K. Richardson.

Graphitic carbon growth on si(111) using solid source molecular beam epitaxy. *Appl. Phys. Lett.*, 95:133114, 2009. xv, 5, 8, 50, 51, 75, 76, 83, 92

[55] J. Tang, C. Y. Kang, L. M. Li, W. S. Yan, S. Q. Wai, and P. S. Xu. Graphene films grown on si substrate via direct deposition of solid-state carbon atoms. *Physica E*, 43:1415, 2011. xv, 5, 8, 51, 52, 76, 83, 92, 93

[56] Dmitry V. Kosynkin, Amanda L. Higginbotham, Alexander Sinitskiiand Jay R. Lomeda, Ayrat Dimiev, B. Katherine Price, and James M. Tour. Longitudinal unzipping of carbon nanotubes to form graphene nanoribbons. *Nature*, 458:872–876, 2009. 5

[57] Wikipedia.org Moore's law. Moore's law. http://en.wikipedia.org/wiki/Moore%27s_law, 2015. 5

[58] E. L. Wolf, editor. *Graphene: A new paradigm in condensed matter and device physics*. Oxford University press, 2014. 5

[59] Kinam Kim, Jae-Young Choi, Taek Kim, Seong-Ho Cho, and Hyun-Jong Chung. A role for graphene in silicon-based semiconductor devices. *Nature*, 479:338–344, 2011. 5

[60] Bavaghar Chahardeh Javad. A review on graphene transistors. *International Journal of Advanced research in Computer and Communication engineering*, 1: 193–197, 2012. 5

[61] Dapeng Wei and Xianfan Xu. Laser direct growth of graphene on silicon substrate. *Applied Physics Letters*, 100(2):023110, 2012. xvi, 5, 8, 61, 62

[62] M. Suemitsu and H. Fukidome. Epitaxial graphene on silicon substrates. *J. Phys. D: Appl. Phys.*, 43:374012, Sept 2010. doi: doi:10.1088/0022-3727/43/37/374012. URL http://iopscience.iop.org/0022-3727/43/37/374012. xv, 7, 53, 54, 55, 71

[63] B. Gupta, M. Notarianni, N. Mishra, M. Shafiei, F. Iacopi, and N. Motta. Evolution of epitaxial graphene layers on 3c sic/si (111) as a function of annealing temperature in uhv. *Carbon*, 68(0):563 – 572, 2014. ISSN 0008-6223. doi: http://dx.doi.org/10.1016/j.carbon.2013.11.035. URL http://www.sciencedirect.com/science/article/pii/S0008622313010956. xv, 56, 57, 58, 91

[64] O. Ochedowski, G. Begall, N. Scheuschner, M. El Kharrazi, J. Maultzsch, and M. Schleberger. Graphene on si(111) 7x7. 2012. doi: doi:10.1088/0022-3727/43/37/374012. arXiv: 1206.0655v1. xvi, 5, 8, 62, 63

[65] Jae-Hyun Lee, Eun Kyung Lee, Won-Jae Joo, Yamujin Jang, Byung-Sung Kim, Jae Young Lim, Soon-Hyung Choi, Sung Joon Ahn, Joung Real Ahn, Min-Ho Park, Cheol-Woong Yang, Byoung Lyong Choi, Sung-Woo Hwang, and Dongmok Whang. Wafer-scale growth of single-crystal monolayer graphene on reusable hydrogen-terminated germanium. 344(6181):286–289, 2014. doi: 10.1126/science.1252268. xv, 5, 60, 61

[66] Casey A Howsare, Xiaojun Weng, Vince Bojan, David Snyder, and Joshua A Robinson. Substrate considerations for graphene synthesis on thin copper films. *Nanotechnology*, 23(13):135601, 2012. URL http://stacks.iop.org/0957-4484/23/i=13/a=135601. xv, 5, 9, 61

[67] Hirokazu Fukidome. Graphene on si. http://www.spring8.or.jp/en/news_publications/press_release/2011/111108/, 2015. xii, 6

[68] Hiromi Karasawa, Tsuneyoshi Komori, Takayuki Watanabe, Akira Satou, Hirokazu Fukidome, Maki Suemitsu, Victor Ryzhii, and Taiichi Otsuji. Observation of amplified stimulated terahertz emission from optically pumped heteroepitaxial graphene-on-silicon materials. *Journal of Infrared, Millimeter, and Terahertz Waves*, 32(5):655–665, 2011. ISSN 1866-6892. doi: 10.1007/s10762-010-9677-1. URL http://dx.doi.org/10.1007/s10762-010-9677-1. xii, 6

[69] Sergey Mikhailov, editor. *Physics and Applications of Graphene - Experiments*. In-Tech, 2011. xii, 6

[70] Guo-Xin Qian and D. J. Chadi. Si(111)7x7 surface: Energy minimization calculation for the dimer stacking fault model. *Phys. Rev. B*, 35:1288–1293, Jan 1987. doi: 10.1103/PhysRevB.35.1288. 6, 8

[71] D. J. Eaglesham, A. E. White, L. C. Feldman, N. Moriya, and D. C. Jacobson. Equilibrium shape of si. *Phys. Rev. Lett.*, 70:1643–1646, Mar 1993. doi: 10.1103/PhysRevLett.70.1643. URL http://link.aps.org/doi/10.1103/PhysRevLett.70.1643. 6

[72] Guang-Hong Lu, Minghuang Huang, Martin Cuma, and Feng Liu. Relative stability of si surfaces: A first-principles study. *Surface Science*, 588(1–3):61 – 70,

2005. ISSN 0039-6028. doi: http://dx.doi.org/10.1016/j.susc.2005.05.028. URL http://www.sciencedirect.com/science/article/pii/S0039602805005455.

[73] Santiago D. Solares, Siddharth Dasgupta, Peter A. Schultz, Yong-Hoon Kim, Charles B. Musgrave, and William A. Goddard. Density functional theory study of the geometry, energetics, and reconstruction process of si(111) surfaces. *Langmuir*, 21(26):12404–12414, 2005. doi: 10.1021/la052029s. URL http://dx.doi.org/10.1021/la052029s. PMID: 16343021. 6

[74] Hyun-Chul Kang, Hiromi Karasawa, Yu Miyamoto, Hiroyuki Handa, Hirokazu Fukidome, Tetsuya Suemitsu, Maki Suemitsu, and Taiichi Otsuji. Epitaxial graphene top-gate {FETs} on silicon substrates. *Solid-State Electronics*, 54 (10):1071 – 1075, 2010. ISSN 0038-1101. doi: http://dx.doi.org/10.1016/j.sse.2010.05.030. URL http://www.sciencedirect.com/science/article/pii/S0038110110002054. Selected Papers from {ISDRS} 2009. 6

[75] Maki Suemitsu, Sai Jiao, Hirokazu Fukidome, Yasunori Tateno, Isao Makabe, and Takashi Nakabayashi. Epitaxial graphene formation on 3c-sic/si thin films. *Journal of Physics D: Applied Physics*, 47(9):094016, 2014. xv, 7, 54, 55, 92

[76] Hirokazu Fukidome, Takayuki Ide, Yusuke Kawai, Toshihiro Shinohara, Naoka Nagamura, Koji Horiba, Masato Kotsugi, Takuo Ohkochi, Toyohiko Kinoshita, Hiroshi Kumighashira, Masaharu Oshima, and Maki Suemitsu. Microscopically-tuned band structure of epitaxial graphene through interface and stacking variations using si substrate microfabrication. *Scientific Reports*, 4:5173, 2014. 7, 55

[77] H. Hibino, T. Fukuda, M. Suzuki, Y. Homma, T. Sato, M. Iwatsuki, K. Miki, and H. Tokumoto. High temperature scanning tunneling microscopy observation of phase transitions and reconstruction on a vicinal si(111) surface. *Phys. Rev. B*, 47:13027–13030, May 1993. doi: 10.1103/PhysRevB.47.13027. URL http://link.aps.org/doi/10.1103/PhysRevB.47.13027. 8

[78] DavidB. Williams and C.Barry Carter. Thinking in reciprocal space. In *Transmission Electron Microscopy*, pages 211–219. Springer US, 2009. ISBN 978-0-387-76500-6. doi: 10.1007/978-0-387-76501-3_12. URL http://dx.doi.org/10.1007/978-0-387-76501-3_12. 10

[79] Vildana Hodzic. Surface states of si(111) surface. *ENEE 697 project*, 1999. 12

[80] R. J. Jaccodine. Surface energy of germanium and silicon. *J. Electrochem. Soc.*, 110(6):524–527, 1963. 12

[81] J. Gilman John. Direct measurements of the surface energies of crystals. *Journal of Applied Physics*, 31(2208), 1960. 12

[82] Vimeo. Si(111) 7x7 surface reconstruction. https://vimeo.com/1086112, 2015. xiii, 12

[83] K. Takayanagi, Y. Tanishiro, M. Takahashi, and S. Takahashi. Structural analysis of si(111)7x7 by uhv transmission electron diffraction and microscopy. *Journal of Vacuum Science and Technology A*, 3(3):1502–1506, 1985. xiii, 12, 13

[84] I.-S. Hwang, M.-S. Ho, and T.-T. Tsong. Scanning tunneling microscope study of dynamic phenomena on clean si(111) surfaces: Si magic clusters and their role. *Journal of Physics and Chemistry of Solids*, 62:1655 – 1671, 2001. ISSN 0022-3697. doi: http://dx.doi.org/10.1016/S0022-3697(01)00103-2. URL http://www.sciencedirect.com/science/article/pii/S0022369701001032. xiii, 13

[85] Houyem Abderrazak and Emna Selman Bel Hadj Hmida. *Chapter 16: Silicon carbide: Synthesis and Properties, Properties and applications of silicon carbide.* 2011. xx, 14, 15

[86] Angel L. Ortiz, Florentino Sanchez-Bajo, Francisco L. Cumbrera, and Fernando Guiberteau. The prolific polytypism of silicon carbide. *Journal of Applied Crystallography*, 46(1):242–247, Feb 2013. doi: 10.1107/S0021889812049151. URL http://dx.doi.org/10.1107/S0021889812049151. 14, 15

[87] Remigijus Vasiliauskas. *Sublimation growth and performance of cubic silicon carbide.* PhD thesis, 2012. 15

[88] W. J. Choyke, H. Matsunami, and G. Pensl. *Silicon carbide: Recent major advances.* 2004. 15

[89] B. Mednikarov, G. Spasov, Tz. Babeva, J. Pirov, M. Sahatchieva, C. Popova, and W. Kulischa. Optical properties of diamond-like carbon and nanocrystalline diamond films. *Journal of Optoelectronics and Advanced Materials*, 7:1407–1413, 2005. 16, 70

[90] S. T. Jackson and R. G. Nuzzo. Determining hybridization differences for amorphous carbon from the xps c 1s envelope. *Applied Surface Science*, 90(2):195

– 203, 1995. ISSN 0169-4332. doi: 10.1016/0169-4332(95)00079-8. URL http://www.sciencedirect.com/science/article/pii/0169433295000798. 16, 70

[91] J. Robertson and E. P. OReilly. Electronic and atomic structure of amorphous carbon. *Phys. Rev. B*, 35:2946–2957, Feb 1987. doi: 10.1103/PhysRevB.35.2946. URL http://link.aps.org/doi/10.1103/PhysRevB.35.2946. 16

[92] N. A. Marks, D. R. McKenzie, B. A. Pailthorpe, M. Bernasconi, and M. Parrinello. Microscopic structure of tetrahedral amorphous carbon. *Phys. Rev. Lett.*, 76: 768–771, Jan 1996. doi: 10.1103/PhysRevLett.76.768. URL http://link.aps.org/doi/10.1103/PhysRevLett.76.768. xiii, 16

[93] B. Kwiecinska and H. I. Petersen. Graphite, semi-graphite, natural coke, and natural char classification-iccp system. *International Journal of Coal Geology*, 57(2):99 – 116, 2004. ISSN 0166-5162. doi: http://dx.doi.org/10.1016/j.coal.2003.09.003. URL http://www.sciencedirect.com/science/article/pii/S0166516203001666. xiii, 16, 17, 19

[94] M.C. Lemme. Current status of graphene transistors. *Solid state Phenomena*, 156-158:499 – 509, 2010. xiii, 18

[95] Li Xuebin. *Epitaxial graphene films on SiC: Growth, characterization and devices*. PhD thesis, 2008. xiii, 18

[96] Edward McCann and Mikito Koshino. The electronic properties of bilayer graphene. *Reports on Progress in Physics*, 76(5):056503, 2013. URL http://stacks.iop.org/0034-4885/76/i=5/a=056503. 18

[97] H. Warner Jamie, editor. *Graphene: Fundamentals and emergent applications*. Elsevier, 2013. 18

[98] C. J. Tabert and E. J. Nicol. Dynamical conductivity of aa-stacked bilayer graphene. *Phys. Rev. B*, 86:075439, Aug 2012. doi: 10.1103/PhysRevB.86.075439. URL http://link.aps.org/doi/10.1103/PhysRevB.86.075439. 19

[99] Xingting Gong and E. J. Mele. Stacking textures and singularities in bilayer graphene. *Phys. Rev. B*, 89:121415, Mar 2014. doi: 10.1103/PhysRevB.89.121415. URL http://link.aps.org/doi/10.1103/PhysRevB.89.121415. 19

[100] Masato Aoki and Hiroshi Amawashi. Dependence of band structures on stacking and field in layered graphene. *Solid State Communications*, 142(3):123 – 127, 2007.

ISSN 0038-1098. doi: http://dx.doi.org/10.1016/j.ssc.2007.02.013. URL http://www.sciencedirect.com/science/article/pii/S0038109807001184. 19

[101] C. L. Lu, C. P. Chang, Y. C. Huang, R. B. Chen, and M. L. Lin. Influence of an electric field on the optical properties of few-layer graphene with ab stacking. *Phys. Rev. B*, 73:144427, Apr 2006. doi: 10.1103/PhysRevB.73.144427. URL http://link.aps.org/doi/10.1103/PhysRevB.73.144427. 19

[102] F. Guinea, A. H. Castro Neto, and N. M. R. Peres. Electronic states and landau levels in graphene stacks. *Phys. Rev. B*, 73:245426, Jun 2006. doi: 10.1103/PhysRevB.73.245426. URL http://link.aps.org/doi/10.1103/PhysRevB.73.245426. 19

[103] S. H. Jhang, M. F. Craciun, S. Schmidmeier, S. Tokumitsu, S. Russo, M. Yamamoto, Y. Skourski, J. Wosnitza, S. Tarucha, J. Eroms, and C. Strunk. Stacking-order dependent transport properties of trilayer graphene. *Phys. Rev. B*, 84:161408, Oct 2011. doi: 10.1103/PhysRevB.84.161408. URL http://link.aps.org/doi/10.1103/PhysRevB.84.161408. 19

[104] Mikito Koshino and Edward McCann. Multilayer graphenes with mixed stacking structure: Interplay of bernal and rhombohedral stacking. *Phys. Rev. B*, 87:045420, Jan 2013. doi: 10.1103/PhysRevB.87.045420. URL http://link.aps.org/doi/10.1103/PhysRevB.87.045420. 19

[105] Hongki Min and A. H. MacDonald. Origin of universal optical conductivity and optical stacking sequence identification in multilayer graphene. *Phys. Rev. Lett.*, 103:067402, Aug 2009. doi: 10.1103/PhysRevLett.103.067402. URL http://link.aps.org/doi/10.1103/PhysRevLett.103.067402. 19

[106] S. Shallcross, S. Sharma, E. Kandelaki, and O. A. Pankratov. Electronic structure of turbostratic graphene. *Phys. Rev. B*, 81:165105, Apr 2010. doi: 10.1103/PhysRevB.81.165105. URL http://link.aps.org/doi/10.1103/PhysRevB.81.165105. 19

[107] Daniel R. Lenski and Michael S. Fuhrer. Raman and optical characterization of multilayer turbostratic graphene grown via chemical vapor deposition. *Journal of Applied Physics*, 110(1):013720, 2011. doi: http://dx.doi.org/10.1063/1.3605545. URL http://scitation.aip.org/content/aip/journal/jap/110/1/10.1063/1.3605545. 19

[108] N Garcia, P Esquinazi, J Barzola-Quiquia, and S Dusari. Evidence for semiconducting behavior with a narrow band gap of bernal graphite. *New Journal of Physics*, 14 (5):053015, 2012. URL http://stacks.iop.org/1367-2630/14/i=5/a=053015. 19

[109] J. Kraublish, A. Bauer, B Wunderlich, and K. Goetz. Lattice parameter measurements of 3c-sic thin films grown on 6h-sic(0001) substrate crystals. *Silicon carbide and related materials*, 2001. 19

[110] *Crystalline SiC on Si technology: Applications and perspectives*, 2012. 19

[111] Charles Whitmore Lawrence. *Microscopy of Nanomachined Silicon*. PhD thesis, 2008. 19

[112] Wikipedia.org. Physical vapor deposition. http://en.wikipedia.org/wiki/Physical_vapor_deposition, 2015. 19

[113] Milton Ohring, editor. *Materials science of thin films*. Academic Press, 2002. 20, 22

[114] Tectra GmbH. e-flux electron beam evaporator. Technical report. 22

[115] http://www.tectra.de/e-flux.htm. xiii, 23, 24, 26

[116] Mac M.C. *Structural and electronic properties of (Zn, M)O fabricated by thermal diffusion of a M thin film grown by evaporation on polar surfaces of ZnO (M = Co or Mn)*. PhD thesis, 2011. 23

[117] Umrath Walter. *Fundamentals of Vacuum technology*. Leybold vacuum products, 1998. 28

[118] In B.K. VAINSHTEIN, editor, *Structure Analysis by Electron Diffraction*. Pergamon, 1964. ISBN 978-0-08-010241-2. 29

[119] B. D. Cullity and R. S. Stock. *Elements of X-ray diffraction*. Prenrice-Hall, 2001. 29, 34, 35

[120] Seldum Thomas. *Selective growth of CdTe by MBE on CdTe(211)B microseeds and Si(100) nanoseeds patterned on SiO2*. PhD thesis, 2009. 30

[121] Department of Surface and Nanostructures Physics Institute of Physics UMCS. Leed and rheed geometry. Technical report. xiv, 31

[122] F Tang, T Parker, G-C Wang, and T-M Lu. Surface texture evolution of polycrystalline and nanostructured films: Rheed surface pole figure analysis. *Journal of Physics D: Applied Physics*, 40(23):R427, 2007. 32, 34

[123] James Douglas Aldous. *Growth, characterization and surface structures of MnSb and NiSb thin films*. PhD thesis, 2011. 33, 35

[124] J. Garrett Simon. Special topics in analytical chemistry, 2001. xiv, 37

[125] Ravi Shankar Sundaram. *Electrical Properties of Chemically Derived Graphene*. PhD thesis, 2011. xiv, 42

[126] Wikipedia.org. Raman spectroscopy. http://en.wikipedia.org/wiki/Raman_spectroscopy, 2015. 42

[127] A. C. Ferrari and J. Robertson. Interpretation of raman spectra of disordered and amorphous carbon. *Phys. Rev. B*, 61:14095–14107, May 2000. doi: 10.1103/PhysRevB.61.14095. URL http://link.aps.org/doi/10.1103/PhysRevB.61.14095. 43, 44

[128] A. C. Ferrari, J. C. Meyer, V. Scardaci, C. Casiraghi, M. Lazzeri, F. Mauri, S. Piscanec, D. Jiang, K. S. Novoselov, S. Roth, and A. K. Geim. Raman spectrum of graphene and graphene layers. *Phys. Rev. Lett.*, 97:187401, Oct 2006. doi: 10.1103/PhysRevLett.97.187401. URL http://link.aps.org/doi/10.1103/PhysRevLett.97.187401. 43, 44, 57, 79

[129] M.A. Pimenta, G. Dresselhaus, M. S. Dresselhaus, L. G. Cancado, A. Jorio, and R. Saito. Studying disorder in graphite-based systems by raman spectroscopy. *Phys. Chem. Chem. Phys.*, 9:1276–1291, 2007. 43

[130] F. Libisch, S. Rotter, and J. Burgdorfer. Disorder scattering in graphene nanoribbons. *Physica Status Solid B*, 248(11):2598–2603, 2011. ISSN 1521-3951. 43

[131] L.M. Malard, M.A. Pimenta, G. Dresselhaus, and M. S. Dresselhaus. Raman spectroscopy in graphene. *Physics Reports*, 473:51 – 87, 2009. ISSN 0370-1573. 43

[132] F. Tuinstra and J. L. Koenig. Raman spectrum of graphite. *The Journal of Chemical Physics*, 53(3):1126–1130, 1970. doi: http://dx.doi.org/10.1063/1.1674108. URL http://scitation.aip.org/content/aip/journal/jcp/53/3/10.1063/1.1674108. 44

[133] L. G. Cancado, K. Takai, T. Enoki, M. Endo, Y. A. Kim, H. Mizusaki, A. Jorio, L. N. Coelho, R. . Magalhaes-Paniago, and M. A. Pimenta. General equation for the determination of the crystallite size la of nanographite by raman spectroscopy. *Applied Physics Letters*, 88(16):163106, 2006. doi: http://dx.doi.org/10.1063/1.2196057. URL http://scitation.aip.org/content/aip/journal/apl/88/16/10.1063/1.2196057. 44, 57

[134] Bart Van Zeghbroeck. *Principles of semiconductor devices*. 2011. 45

[135] Franz J. Giessibl. Advances in atomic force microscopy. *Rev. Mod. Phys.*, 75: 949–983, Jul 2003. doi: 10.1103/RevModPhys.75.949. URL http://link.aps.org/doi/10.1103/RevModPhys.75.949. xiv, 46

[136] Seokmin Jeon. *Structure, chemistry and energetics of organic and inorganic adsorbates on Ga-rich GaAs and GaP(001) surfaces*. PhD thesis, 2014. xiv, 46

[137] J. Tersoff and D. R. Hamann. Theory of the scanning tunneling microscope. *Phys. Rev. B*, 31:805–813, Jan 1985. doi: 10.1103/PhysRevB.31.805. URL http://link.aps.org/doi/10.1103/PhysRevB.31.805. 46

[138] Z.Q. Yu, C.M. Wang, Y. Du, S. Thevuthasan, and I. Lyubinetsky. Reproducible tip fabrication and cleaning for uhv/stm. *Ultramicroscopy*, 108(9):873 – 877, 2008. ISSN 0304-3991. doi: http://dx.doi.org/10.1016/j.ultramic.2008.02.010. URL http://www.sciencedirect.com/science/article/pii/S0304399108000363. 47

[139] http://www.doitpoms.ac.uk/tlplib/afm/tip_surface_interaction.php. xiv, 48

[140] Wikipedia.org Atomic force microscopy. Afm. http://en.wikipedia.org/wiki/Atomic_force_microscopy, 2015. xiv, 48

[141] JPK instruments AG. A practical guide to afm force spectroscopy and data analysis. Technical report. 47

[142] B. Cappella and G. Dietler. Force-distance curves by atomic force microscopy. *Surface Science Reports*, 34:1 – 104, 1999. ISSN 0167-5729. doi: http://dx.doi.org/10.1016/S0167-5729(99)00003-5. URL http://www.sciencedirect.com/science/article/pii/S0167572999000035. 47

[143] Robert A. Wilson and Heather A. Bullen. Basic theory: atomic force microscopy. http://asdlib.org/onlineArticles/ecourseware/Bullen/SPMModule_BasicTheoryAFM.pdf, 2015. 48

[144] Walt A. de Heer, Claire Berger, Ming Ruan, Mike Sprinkle, Xuebin Li, Yike Hu, Baiqian Zhang, John Hankinson, and Edward Conrad. Large area and structured epitaxial graphene produced by confinement controlled sublimation of silicon carbide. *Proceedings of the National Academy of Sciences*, 108(41):16900–16905, 2011. 52, 79

[145] Michael Bolen, Sara Harrison, Laura Biedermann, and Michael Capano. Graphene formation mechanisms on 4h-sic(0001). *Phys. Rev. B*, 80:115433, Sep 2009. 53

[146] A. Ouerghi, A. Kahouli, D. Lucot, M. Portail, L. Travers, J. Gierak, J. Penuelas, P. Jegou, A. Shukla, T. Chassagne, and M. Zielinski. Epitaxial graphene on cubic sic(111)/si(111) substrate. *Applied Physics Letters*, 96(19):191910, 2010. doi: http://dx.doi.org/10.1063/1.3427406. URL http://scitation.aip.org/content/aip/journal/apl/96/19/10.1063/1.3427406. 53, 59, 71, 79, 94, 95

[147] H. Fukidome, R. Takahashi, S. Abe, K. Imaizumi, H. Handa, H.-C. Kang, H. Karasawa, T. Suemitsu, T. Otsuji, Y. Enta, A. Yoshigoe, Y. Teraoka, M. Kotsugi, T. Ohkouchi, T. Kinoshita, and M. Suemitsu. Control of epitaxy of graphene by crystallographic orientation of a si substrate toward device applications. *J. Mater. Chem.*, 21:17242–17248, 2011. doi: 10.1039/C1JM12921J. URL http://dx.doi.org/10.1039/C1JM12921J. 55

[148] Hirokazu Fukidome, Yu Miyamoto, Hiroyuki Handa, Eiji Saito, and Maki Suemitsu. Epitaxial growth processes of graphene on silicon substrates. *Japanese Journal of Applied Physics*, 49(1S):01AH03, 2010. xv, 55, 56

[149] Z. H. Ni, W. Chen, X. F. Fan, J. L. Kuo, T. Yu, A. T. S. Wee, and Z. X. Shen. Raman spectroscopy of epitaxial graphene on a sic substrate. *Phys. Rev. B*, 77:115416, Mar 2008. doi: 10.1103/PhysRevB.77.115416. URL http://link.aps.org/doi/10.1103/PhysRevB.77.115416. 57

[150] Seong-Yong Cho, Hyun-Mi Kim, Min-Hyun Lee, Do-Joong Lee, and Ki-Bum Kim. Direct formation of graphene layers on top of sic during the carburization of si substrate. *Current Applied Physics*, 12(4):1088 – 1091, 2012. ISSN 1567-1739. doi: http://dx.doi.org/10.1016/j.cap.2012.01.013. URL http://www.sciencedirect.com/science/article/pii/S1567173912000144. xv, 58, 59

[151] N. Gogneau, A. Balan, M. Ridene, A. Shukla, and A. Ouerghi. Control of the degree of surface graphitization on 3c-sic(100)/si(100). *Surface Science*, 606(3–4): 217 – 220, 2012. ISSN 0039-6028. 59

[152] M. Portail, A. Michon, S. Vezian, D. Lefebvre, S. Chenot, E. Roudon, M. Zielinski, T. Chassagne, A. Tiberj, J. Camassel, and Y. Cordier. Growth mode and electric properties of graphene and graphitic phase grown by argon propane assisted cvd on 3c-sic/si and 6h-sic. *Journal of Crystal Growth*, 349(1):27 – 35, 2012. ISSN 0022-0248. 59

[153] A. Michon, A. Tiberj, S. Vezian, E. Roudon, D. Lefebvre, M. Portail, M. Zielinski, T. Chassagne, J. Camassel, and Y. Cordier. Graphene growth on aln templates on silicon using propane-hydrogen chemical vapor deposition. *Applied Physics Letters*, 104(7):071912, 2014. doi: http://dx.doi.org/10.1063/1.4866285. URL http://scitation.aip.org/content/aip/journal/apl/104/7/10.1063/1.4866285. xv, 60

[154] Gang Wang, Miao Zhang, Yun Zhu, Guqiao Ding, Da Jiang, Qinglei Guo, Su Liu, Xiaoming Xie, Paul K. Chu, Zengfeng Di, and Xi Wang. Direct growth of graphene film on germanium substrate. *Scientific Reports*, 3:2465, 2013. 60

[155] Wei Liu, Choong-Heui Chung, Cong-Qin Miao, Yan-Jie Wang, Bi-Yun Li, Ling-Yan Ruan, Ketan Patel, Young-Ju Park, Jason Woo, and Ya-Hong Xie. Chemical vapor deposition of large area few layer graphene on si catalyzed with nickel films. *Thin Solid Films*, 518(6, Supplement 1):S128 – S132, 2010. ISSN 0040-6090. doi: http://dx.doi.org/10.1016/j.tsf.2009.10.070. URL http://www.sciencedirect.com/science/article/pii/S0040609009017131. Sixth International Conference on Silicon Epitaxy and Heterostructures. xv, 61

[156] Xuesong Li, Weiwei Cai, Jinho An, Seyoung Kim, Junghyo Nah, Dongxing Yang, Richard Piner, Aruna Velamakanni, Inhwa Jung, Emanuel Tutuc, Sanjay K. Banerjee, Luigi Colombo, and Rodney S. Ruoff. Large-area synthesis of high-quality and uniform graphene films on copper foils. *Science*, 324(5932):1312–1314, 2009. doi: 10.1126/science.1171245. 62, 63

[157] Xiaobo Li and Ronggui Yang. Effect of lattice mismatch on phonon transmission and interface thermal conductance across dissimilar material interfaces. *Phys. Rev. B*, 86:054305, Aug 2012. doi: 10.1103/PhysRevB.86.054305. URL http://link.aps.org/doi/10.1103/PhysRevB.86.054305. 63

[158] V. V. Brus, M. A. Gluba, X. Zhang, K. Hinrichs, J. Rappich, and N. H. Nickel. Stability of graphene - silicon heterostructure solar cells. *physica status solidi*

(a), 211(4):843–847, 2014. ISSN 1862-6319. doi: 10.1002/pssa.201470223. URL http://dx.doi.org/10.1002/pssa.201470223. xvi, 63

[159] Zhongliang Liu, Jinfeng Liu, Peng Ren, Yuyu Wu, and Pengshou Xu. Effects of carbonization and substrate temperature on the growth of 3c-sic on si by ssmbe. *Applied Surface Science*, 254(10):3207 – 3210, 2008. ISSN 0169-4332. doi: http://dx.doi.org/10.1016/j.apsusc.2007.10.085. URL http://www.sciencedirect.com/science/article/pii/S0169433207015693. 68

[160] L.I Johansson, P.-A Glans, and N Hellgren. A core level and valence band photoemission study of 6h-sic(000-1). *Surface Science*, 405:288 – 297, 1998. ISSN 0039-6028. doi: 10.1016/S0039-6028(98)00086-7. URL http://www.sciencedirect.com/science/article/pii/S0039602898000867. 69, 71, 84

[161] H. Matsunami and T. Kimoto. Step-controlled epitaxial growth of sic- high quality homoepitaxy. *Materials Science and Engineering*, 20(3):125 – 166, 1997. ISSN 0927-796X. URL http://www.sciencedirect.com/science/article/pii/S0927796X97000053. 71

[162] Y. Inoue, S. Nakashima, A. Mitsuishi, S. Tabata, and S. Tsuboi. Raman spectra of amorphous sic. *Solid State Communications*, 48(12):1071 – 1075, 1983. ISSN 0038-1098. doi: 10.1016/0038-1098(83)90834-7. URL http://www.sciencedirect.com/science/article/pii/0038109883908347. 72

[163] L Calcagno, P Musumeci, F Roccaforte, C Bongiorno, and G Foti. Crystallization process of amorphous silicon-carbon alloys. *Thin Solid Films*, 411(2):298 – 302, 2002. ISSN 0040-6090. doi: 10.1016/S0040-6090(02)00332-2. URL http://www.sciencedirect.com/science/article/pii/S0040609002003322. 72

[164] S. Latil and L. Henrard. Massless fermions in multilayer graphitic systems with misoriented layers: ab initio calculations and experimental fingerprints. *Phys. Rev. B*, 76:201402, 2007. 73

[165] Yongfeng Wang, Yingchun Ye, and Kai Wu. Simultaneous observation of the triangular and honeycomb structures on highly oriented pyrolytic graphite at room temperature: An stm study. *Surface Science*, 600(3):729 – 734, 2006. ISSN 0039-6028. doi: 10.1016/j.susc.2005.12.001. 73, 79, 90

[166] Nikhil Sharma, Doogie Oh, Harry Abernathy, Meilin Liu, Phillip N. First, and Thomas M. Orlando. Signatures of epitaxial graphene grown on si-terminated

6h-sic (0 0 0 1). *Surface Science*, 604(2):84 – 88, 2010. ISSN 0039-6028. doi: http://dx.doi.org/10.1016/j.susc.2009.10.014. URL http://www.sciencedirect.com/science/article/pii/S0039602809006645. 79

[167] Olga Kazakova, Vishal Panchal, and Tim L. Burnett. Epitaxial graphene and graphene–based devices studied by electrical scanning probe microscopy. *Crystals*, 3(1):191, 2013. ISSN 2073-4352. doi: 10.3390/cryst3010191. URL http://www.mdpi.com/2073-4352/3/1/191. 79

[168] Jonathan D. Emery, Blanka Detlefs, Hunter J. Karmel, Luke O. Nyakiti, D. Kurt Gaskill, Mark C. Hersam, Jörg Zegenhagen, and Michael J. Bedzyk. Chemically resolved interface structure of epitaxial graphene on sic(0001). *Phys. Rev. Lett.*, 111:215501, Nov 2013. doi: 10.1103/PhysRevLett.111.215501. URL http://link.aps.org/doi/10.1103/PhysRevLett.111.215501. 79

[169] K. V. Emtsev, F. Speck, Th. Seyller, L. Ley, and J. D. Riley. Interaction, growth, and ordering of epitaxial graphene on sic0001 surfaces: A comparative photoelectron spectroscopy study. *Phys. Rev. B*, 77:155303, Apr 2008. doi: 10.1103/PhysRevB.77.155303. URL http://link.aps.org/doi/10.1103/PhysRevB.77.155303. 79

[170] Takayuki Ide, Yusuke Kawai, Hiroyuki Handa, Hirokazu Fukidome, Masato Kotsugi, Takuo Ohkochi, Yoshiharu Enta, Toyohiko Kinoshita, Akitaka Yoshigoe, Yuden Teraoka, and Maki Suemitsu. Epitaxy of graphene on 3c-sic(111) thin films on microfabricated si(111) substrates. *Japanese Journal of Applied Physics*, 51(6S): 06FD02, 2012. URL http://stacks.iop.org/1347-4065/51/i=6S/a=06FD02. xvii, 81

[171] Pham Thanh Trung, Frederic Joucken, Jessica Campos-Delgado, Jean-Pierre Raskin, Benoit Hackens, and Robert Sporken. Direct growth of graphitic carbon on si(111). *Applied Physics Letters*, 102(1), 2013. 83, 92

[172] Long Zhang, Fan Zhang, Xi Yang, Guankui Long, Yingpeng Wu, Tengfei Zhang, Kai Leng, Yi Huang, Yanfeng Ma, Ao Yu, and Yongsheng Chen. Porous 3d graphene-based bulk materials with exceptional high surface area and excellent conductivity for supercapacitors. *Scientific Reports*, 3(1408), 2013. doi: doi:10.1038/srep01408. 88

[173] E. Moreau, S. Godey, F. J. Ferrer, D. Vignaud, X. Wallart, J. Avila, M. C. Asensio, F. Bournel, and J.-J. Gallet. Graphene growth by molecular beam epitaxy on the carbon-face of sic. *Applied Physics Letters*, 97(24):241907, 2010. 91

[174] R. Scholz, U. Gosele, F. Wischmeyer, and E. Niemann. Formation and prevention of micropipes and voids in cvd carbonization experiments on (111) silicon. *Materials Science Forum*, 264-268:219 – 222, 1998. 92

[175] Pham Thanh Trung, Jessica Campos-Delgado, Frederic Joucken, Jean-Francois Colomer, Benoit Hackens, Jean-Pierre Raskin, Cristiane N. Santos, and Sporken Robert. Direct growth of graphene on si(111). *Journal of Applied Physics*, 115 (22), 2014. 92

[176] C Riedl, C Coletti, and U Starke. Structural and electronic properties of epitaxial graphene on sic(000-1): a review of growth, characterization, transfer doping and hydrogen intercalation. *Journal of Physics D: Applied Physics*, 43(37):374009, 2010. 94

[177] Ok-Kyung Park, Yong-Mun Choi, Jun Yeon Hwang, Cheol-Min Yang, Tea-Wook Kim, Nam-Ho You, Hye Young Koo, Joong Hee Lee, Bon-Cheol Ku, and Munju Goh. Defect healing of reduced graphene oxide via intramolecular cross-dehydrogenative coupling. *Nanotechnology*, 24(18):185604, 2013. 94

[178] F. Varchon, R. Feng, J. Hass, X. Li, B.N. Nguyen, C. Naud, P. Mallet, J.-Y. Veuillen, C. Berger, E.H. Conrad, and L. Magaud. Electronic structure of epitaxial graphene layers on sic: Effect of the substrate. *Physical Review Letters*, 99(12): 126805, September 2007. 95

[179] Song Zhang, Rong Tu, and Takashi Goto. High-speed epitaxial growth of sic film on si(111) single crystal by laser chemical vapor deposition. *Journal of the American Ceramic Society*, 95(9):2782–2784, 2012. ISSN 1551-2916. 95

[180] TS Perova, J Wasyluk, SA Kukushkin, AV Osipov, NA Feoktistov, and SA Grudinkin. Micro-raman mapping of 3c-sic thin films grown by solid-gas phase epitaxy on si (111). *Nanoscale Research Letters*, 5(9):1507–1511, 2010. ISSN 1556-276X. doi: 10.1007/s11671-010-9670-6. 96, 107

[181] Toshiaki Enoki. Role of edges in the electronic and magnetic structures of nanographene. *Physica Scripta*, 2012(T146):014008, 2012. URL http://stacks.iop.org/1402-4896/2012/i=T146/a=014008. 98

[182] Ken-ichi Sakai, Kazuyuki Takai, Ken-ichi Fukui, Takeshi Nakanishi, and Toshiaki Enoki. Honeycomb superperiodic pattern and its fine structure near the armchair

edge of graphene observed by low-temperature scanning tunneling microscopy. *Phys. Rev. B*, 81:235417, Jun 2010. doi: 10.1103/PhysRevB.81.235417. 98

[183] Mehrer Helmut, editor. *Diffusion in solids: Fundamentals, Methods, Materials, Diffusion-Controlled processes*. Springer, 2007. 100, 102

[184] W. Jones Scotten. Diffusion in silicon, 2008. 102

[185] Dept. of Materials Sciences University of Tennessee and Engineering. Diffusion, 2015. 102

[186] L. Moro, A. Paul, D. C. Lorents, R. Malhotra, R. S. Ruoff, P. Lazzeri, L. Vanzetti, A. Lui, and S. Subramoney. Silicon carbide formation by annealing c60 films on silicon. *Journal of Applied Physics*, 81(9):6141–6146, 1997. doi: http://dx.doi.org/10.1063/1.364395. URL http://scitation.aip.org/content/aip/journal/jap/81/9/10.1063/1.364395. 103, 107

[187] V. Cimalla, Th. Stauden, G. Eichhorn, and J. Pezoldt. Influence of the heating ramp on the heteroepitaxial growth of sic on si. *Materials Science and Engineering*, B61-62:553–558, 1999. 103

[188] M. Ollivier, L. Latu-Romain, M. Martin, S. David, A. Mantoux, E. Bano, V. Soulière, G. Ferro, and T. Baron. Si-sic core-shell nanowires. *Journal of Crystal Growth*, 363(0):158 – 163, 2013. ISSN 0022-0248. doi: http://dx.doi.org/10.1016/j.jcrysgro.2012.10.039. URL http://www.sciencedirect.com/science/article/pii/S0022024812007440. 107

[189] K Volz, S Schreiber, J.W Gerlach, W Reiber, B Rauschenbach, B Stritzker, W Assmann, and W Ensinger. Heteroepitaxial growth of 3c-sic on (100) silicon by c60 and si molecular beam epitaxy. *Materials Science and Engineering: A*, 289:255 – 264, 2000. ISSN 0921-5093. doi: http://dx.doi.org/10.1016/S0921-5093(00)00825-X. URL http://www.sciencedirect.com/science/article/pii/S092150930000825X. 107